A comprehensive CFD methodology for the simulation of Spark Ignited Engines

A comprehensive CFD methodology for the simulation of Spark Ignited Engines

by

Enrico Delogu

Dissertation submitted to the Doctoral School of the Politecnico di Torino in partial fullfilment of the requirements for the Degree of

DOCTOR OF PHILOSOPHY IN ENERGETICS AT THE POLITECNICO DI TORINO

May 2013

Tutor:
Prof. Federico Millo

Scientific Committee:
Prof. Carlo Vincenzo Ferraro
Prof. Angelo Onorati
Prof. Lucio Postrioti

Summary

In this work, a Computational Fluid Dynamic methodology for the simulation of the charge formation process in Gasoline Direct Injection engines is presented. The aim of the work is to develop a methodology suitable in an industrial environment to drive and support the development process of modern GDI engines.

A big emphasis is placed on the comparison of the proposed CFD models with experimental data obtained using a single-cylinder optical engine.

Chapter 1 describes the working context and sets the aim of the work. After a brief recall of the theoretical background of CFD in chapter 2, an overview of the optical techniques interesting for Internal Combustion Engine applications is presented in chapter 3, and the basic principles of spray atomization theory are reviewed in chapter 4.

In chapter 5 the CFD simulations for the charge motion in-cylinder are described. Two different engines were investigated, and the effect of different turbulence models and numerical schemes are analyzed, comparing the results with optical experimental data. The standard k-ε model, together with the MARS numerical scheme, showed the better capability to reproduce the charge motion and turbulence pattern in-cylinder, and therefore they were used for the remaining part of the work.

In chapter 6 the injection model used is discussed. De-

spite a traditional Lagrangian-Eulerian approach, the model presents an innovative procedure capable to reproduce also the liquid core. After that the effects of the use of the liquid core and a bi-component fuel are analyzed, the in-cylinder injection results for the two investigated engines are presented. The injection model shows its capability to correctly reproduce the spray shape and penetration in different operating conditions and for different injector types, using a reduced amount of calibration parameters.

Finally, chapter 7 presents some "diagnostic indexes" capable to resume the results of the CFD simulations in a reduced number of parameters. In particular, some indexes to assess the quality of the mixture and the wall impingement tendency are proposed, allowing to use the CFD simulations to address these crucial aspects in the choice of injector targeting and actuation strategy.

The proposed methodology allows to use CFD simulations to support the engine development process, and was successfully applied to many different spark ignited engines.

Contents

List of Figures

List of Tables

Nomenclature

Symbols

η	Scale length
λ	Wavelength; air-fuel equivalence ratio
μ	Dynamic viscosity
ν	Kinematic viscosity
Ω	Volume (in integral equations)
ω	Turbulence dissipation frequency
ρ	Density
σ	Surface tension
$\overline{\overline{\sigma}}$	Stress tensor
ε	Turbulence kinetic energy dissipation rate
$\vec{F}$	Flux vector
$\vec{v}$	Velocity
C	Constant
d	Particle diameter; nozzle diameter

E	Total energy ($E \triangleq e + \vec{v}^2/2$)
e	Internal energy per unit mass
F_D	Diffusive flux
f_e	External forces
k	Thermal conductivity coefficient; turbulence kinetic energy
l	Nozzle orifice length
p	Pressure
Q	Source term
r	Nozzle hole rounding radius
T	Temperature
t	Time
U	Generic conservative variable
u	Generic speed
We	Weber number

Subscripts

a	air
d	droplet
f	fuel
g	gas
l	liquid

S	Surface
stoich	Stoichiometric
V	Volume; viscous

Abbreviation

AFR	Air/Fuel Ratio
AMR	Adaptive Mesh Refinement
BDC	Bottom Dead Center
CA	Crank Angle
CFD	Computational Fluid Dynamics
DI	Direct injection
DNS	Direct Numerical Solution
DOI	Duration Of Injection
FV	Finite Volume
GDI	Gasoline Direct Injection
GUI	Graphical User Interface
HCCI	Homogeneous Charge Compression Ignition
HWA	Hot Wire Anemometry
ICE	Internal Combustion Engine
imep	Indicated Mean Effective Pressure
LDA	Laser Doppler Anemometry
LES	Large Eddy Simulation

LIF Laser Induced Fluorescence

PDA Phase Doppler Anemometry

PDE Partial Differential Equations

PFI Port Fuel Injection

PIV Particle Image Velocimetry

RANS Reynolds Averaged Navier-Stokes

SI Spark Ignition

SMD Sauter Mean Diameter

SOI Start Of Injection

TDC, ATDC, FTDC Top Dead Center, After TDC, Firing TDC

Notation

$\bar{\cdot}$ Time averaging of $\cdot$; Mean part of a turbulent term $\cdot$

$\cdot''$ Fluctuating part of a turbulent term $\cdot$

$\otimes$ Tensorial product

Chapter 1

Introduction

Engine development has nowadays to deal with a stringent legislation on the pollutant emissions, and a constant attempt to reduce the fuel consumption, as required from the marketing, the governments and the customers. However, the research for constant increasingly performances and fun to drive cannot be neglected to create a winning product on the market. Cost reduction and short development time complete the framework in which every new engine for series production is generally developed.

In this chapter, the effects of the main existing laws on the pollutant emissions will be revised, since they currently drive and deeply affect the engine development. Afterward, the role of gasoline direct injection engines in the current scenario of engines will be discussed, and finally the general aim of the CFD simulations during the engine development, and in particular the motivation for the present work, will be presented.

1.1 Emission legislation

Since when at the beginning of 50's the problem of air pollutions became known in Los Angeles, various and constantly

more stringent legislations were set all over the world, beginning from California to Europe, Japan and nowadays even China and India. Legislations are considerably different, both in term of regulated pollutants and their limits, as well as the test driving cycles. At the moment however, the USA limits as well as the Japanese ones are the most severe, taking into account also the adopted test cycle, but with the introduction of the Euro 6 in 2014 also in Europe quite challenging limits will be required. A further requisite, particular stringent in Europe, is the request from European Community accepted by ACEA[1] to reduce the fleet-averaged CO_2 emissions until the level of 95 g/Km for 2020, corresponding to a fuel consumption of approx. 4.1 l/100 Km for gasoline engines.

A discussion on the homologation cycles in each country and the law limits is beyond the purpose of this chapter, but can be easily found in the specific literature [1, 2].

Thanks to the use of the three-way catalytic converter, the prescribed limits in term of CO and HC emissions can be reached without too many problems, if a proper combustion without misfiring and a correct air-fuel ratio is provided. For gasoline direct injection, the compliance with the maximum number of particulate particles is more difficult to be reached. This limit has been introduced with the Euro 6 and it is currently proposed to be for the first three years $6.0{\cdot}10^{12}$ #/km, that then will be reduced to $6.0{\cdot}10^{11}$ #/km [3]. In case of GDI engines working in lean stratified mode, also the NO_x limits have to be carefully considered, while these are generally easily achievable in case of homogeneous combustion.

1.2 Gasoline Direct Injection engines

Gasoline Direct Injection engines can be operated in homogeneous mode or in lean-stratified mode. In the former mode,

[1] European Automobile Manufacturers Association.

like in a conventional port fuel injection (PFI) engine, the fuel is introduced in the cylinder in approximately stoichiometric ratio with the air, in order to achieve an homogeneous air-fuel mixture. The latter one is more difficult to be realized, since a detailed control of the spray in-cylinder is required in order to achieve the desired stratification, nevertheless it has numerous advantages in terms of reduction of fuel consumption thanks to [4]:

- reduced pumping losses, since the load control is done through a different injected quantity and a different global air-fuel ratio as in the diesel engines;
- reduced temperature in-cylinder and consequently reduced heat losses;
- higher compression ratio achievable thanks to the fuel evaporation cooling effect;
- possibility of easier fuel cut-off during deceleration, and lower acceleration enrichment, since no fuel film is built on the intake port.

It is worth to point out that nowadays, due to difficulties in realizing the fuel stratification at different speeds and loads, many GDI engines on the market always operate in homogeneous mode. The first advantage on the list – which is also the most attractive one, both in the homologation cycle and the real working conditions, where the engine is very often used at partial load – is lost. However, all the other mentioned advantages remain valid also in case of homogeneous operation, and make the GDI engines very attractive in order to reduce the fuel consumption of modern cars.

Downsizing is another concept which is nowadays often mentioned. In the past, downsizing was used only in case of packaging constraints, in order to obtain the same performance of an higher displacement engine reducing the engine size and

equipping it with a boosting system (either a turbocharger or a supercharger) [5]. Nowadays downsizing is mainly used to reduce fuel consumption and consequently CO_2 emissions. A reduced displacement allows to decrease the mechanical losses due to auxiliaries and frictions. Furthermore, the engine will be generally operated at higher load, reducing the pumping losses and the impact of organic losses on the total generated power, ending up in an higher efficiency. Finally, the use of boosting systems enhances the low-end torque, nowadays synonymous of fun-to-drive for many OEMs and customers.

1.2.1 Problematics of GDI engines

As already mentioned in the section 1.1, pollutant emissions and fuel consumption nowadays drive the development process of each engine for the series production. The main issues of GDI engines are related to the maximum number of soot particles admitted by the legislation, since due to the direct injection some pool fires events could occur in-cylinder, causing a considerable production of soot.

Pool fires are nowadays considered related to the liquid fuel impingement on the piston and on the valves, as well as the presence of rich locations in the cylinder or not completely evaporated droplets [6, 7, 8]. For these reasons, during the GDI development an high attention to the definition of the injector positioning, targeting and actuation strategy is required.

Another issue that has to be specifically addressed in case of GDI engines is the catalytic converter heating phase. Since during the warm-up of the catalytic converter most of the whole pollutant emissions in the homologation cycle are produced, it is necessary to short up this phase. For this reason a very late spark timing is used in order to increase the exhaust temperature, and multiple injections strategy can be exploited to improve the ignitability of the mixture, creating a slightly rich mixture near the spark-plug at the crankangle of ignition.

Especially in extremely downsized engines, some problems can derive from an excessive oil dilution, and for this reason the spray targeting is once again of extreme importance, since it determines how much liquid fuel will impinge on the liner.

Finally, parallel to the increase of the downsizing grade and the correspondent increase of boosting level to obtain higher effective pressures, issues related to abnormal combustion phenomena such as pre-ignition and knocking are gaining again importance.

1.3 CFD simulations

CFD simulations play an important role in the engine development, and they are used at different stages of the design process with different purposes.

During the early phases of the engine development, simulations in general are at the forefront, since they allow to cost effectively explore different concepts and ideas, using some "virtual prototypes" in a phase in which many details of the project are still unknown. In this phase, it is also possible to early identify possible problems or criticalities, and solve them with almost no impact on the time scheduling or project budget.

Fig. 1.1, from Lindhal [9], expresses why it is important to invest in the simulations especially during the first phase of the project. Simulations allow to quickly and effectively gain a detailed knowledge of the project, and can be used to exploit different variants with reduced amount of investments. Problems can be early identified and solved preventing from modifications in the late phases of the development, that would be more expensive.

However, CFD simulations are used also in the late phase of the project, to deeply investigate some phenomena which cannot be analyzed in enough high detail from the experimen-

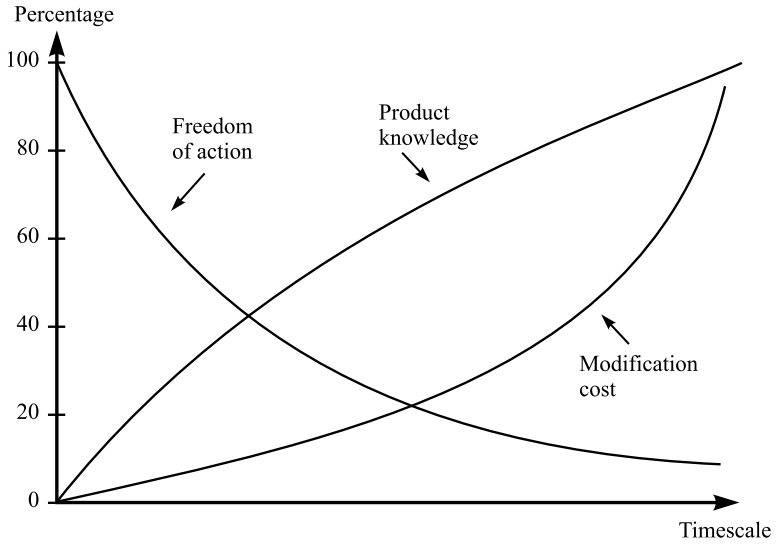

Figure 1.1: Freedom of action, product knowledge and modification costs during the project development [9].

tal point of view. CFD simulations are in these cases useful to properly address some issues that are encountered at the test-bench, but which cannot be enough well investigated and understood just looking at the collected experimental data.

Independently from the use, a prerogative of each simulation is its reliability. In opposition with experimental research, in the simulations the physical phenomena have to be modeled individually defining their governing equation, and only if a proper model is provided, the effects of a certain phenomenon will be visible in the results.

1.4 Motivation of the work

CFD simulations involve a huge amount of physical phenomena, and also the numerical aspects play a relevant role in de-

termining the quality of the results. As explained in the previous paragraph, a prerogative of each simulation is its reliability and possibility to correctly reproduce the physical phenomena of interests.

In this work, the phenomena of major interest in the development of a modern GDI engine were investigated, in order to be able to correctly reproduce them in the simulations, developing a reliable but at the same time easy and fast to use tool capable to support the development process.

In order to assess the results of the simulation, experimental data obtained from different optical engines were used, as well as experimental results from series production engines measured at the test-bench.

The goal of this work is to develop a procedure to simulate the mixture formation in GDI engines. In particular, the work is focused on the air motion in-cylinder and on the injection phase, until the mixture formation before the ignition. The simulation of combustion in gasoline engines is nowadays still in the research phase, and it is generally not used for the engine design. Although it constitutes an interesting research topic, it requires a computation and experimental effort far beyond the current state of the art in the daily engine development process, and it is not covered in this work.

Chapter 2

Computational Fluid Dynamics Fundamentals

In this chapter a short introduction about the basic equations behind a computational fluid dynamics code will be presented. The purpose of this chapter is not to give an exhaustive picture of this extremely wide subject, for which a wide literature exists (see for instance [10, 11, 12]), but to recall the theoretical background on which this work is based, focusing on some of the most important aspects.

2.1 Navier-Stokes equations

The so-called Navier-Stokes equations are a set of three partial differential equations that describes the motion of a fluid. They express the more general physical principle of conservation of mass, momentum, energy and species concentrations, and therefore all can be derived from a general conservation equation, changing the variable of which is intended to express the conservation.

The general form of a conservation equation can be written as:

$$\frac{\partial}{\partial t}\int_{\Omega} U \,\mathrm{d}\Omega + \oint_{S} \vec{F}\cdot \mathrm{d}\vec{S} = \int_{\Omega} Q_v \,\mathrm{d}\Omega + \oint_{S} \vec{Q}_S \cdot \mathrm{d}\vec{S} \qquad (2.1)$$

where U is the conserved scalar variable on the volume Ω, delimited by the surface S, and $\vec{F}$ indicates its flux through the surface. Q_v and Q_S are the source terms, respectively of volume and surface. In case of a vectorial quantity $\vec{U}$, the conservation equation becomes:

$$\frac{\partial}{\partial t}\int_{\Omega} \vec{U} \,\mathrm{d}\Omega + \oint_{S} \overline{\overline{F}}\cdot \mathrm{d}\vec{S} = \int_{\Omega} \vec{Q_v} \,\mathrm{d}\Omega + \oint_{S} \overline{\overline{Q}}_S \cdot \mathrm{d}\vec{S} \qquad (2.2)$$

where the previous vectorial flux term and the surface source term are now substituted by the corresponding tensors.

From this general equation, the conservation equations for mass, momentum, energy and species mass can be derived. The equations are derived per unit of volume, thus in case of the mass the conserved quantity U will be the density ρ, in case of the momentum it will be the term $\rho\vec{v}$, where $\vec{v}$ is the fluid velocity, and in case of the energy it will be the specific internal energy e.

In case of the mass conservation equation, no diffusive flux exists for the mass transport, thus only the convective flux is present in the equation.

For the momentum conservation equation, the external forces $\vec{f_e}$ acting on the system and the stress tensor $\overline{\overline{\sigma}}$ act respectively as the volume and the surface source terms.

To obtain the energy conservation equation, the total energy E can be defined as the sum of the fluid internal energy and its kinetic energy per unit mass, i.e. $E \triangleq e + \vec{v}^2/2$. The source terms, as known from the first law of thermodynamics, are the work of the forces acting on the system, plus the heat

transmitted to this system. The volume sources are the sum of the work of the volume forces $\vec{f_e}$ and of the heat sources other than conduction, such as radiation and heat released by chemical reactions, designated by q_H. The surface sources Q_S are the result of the work done on the fluid by the internal shear stresses acting on the surface of the volume, considering that there are no external surface heat sources, and so $Q_S = \overline{\overline{\sigma}} \cdot \vec{v}$. The convective flux of energy can be easily calculated, while the diffusive flux F_D can be written using the Fourier's law of heat conduction, so $\vec{F}_D = -k\vec{\nabla}T$, where T is the absolute temperature and k is the thermal conductivity coefficient.

Taking into account the previous considerations, the full set of Navier-Stokes equations, expressed in the so-called integral form, is:

$$\begin{aligned}
\frac{\partial}{\partial t}\int_\Omega \rho \,\mathrm{d}\Omega + \oint_S \rho\vec{v}\cdot\mathrm{d}\vec{S} &= 0 \\
\frac{\partial}{\partial t}\int_\Omega \rho\vec{v} \,\mathrm{d}\Omega + \oint_S \rho\vec{v}(\vec{v}\cdot\vec{S}) &= \int_\Omega \rho\vec{f_e} \,\mathrm{d}\Omega + \oint_S \overline{\overline{\sigma}}\cdot\mathrm{d}\vec{S} \\
\frac{\partial}{\partial t}\int_\Omega \rho E \,\mathrm{d}\Omega + \oint_S \rho E\vec{v}\cdot\mathrm{d}\vec{S} & \\
- \oint_S k\vec{\nabla}T\cdot\mathrm{d}\vec{S} &= \int_\Omega (\rho\vec{f_e}\cdot\vec{v} + q_H)\,\mathrm{d}\Omega \\
&\quad + \oint_S (\overline{\overline{\sigma}}\cdot\vec{v})\cdot\mathrm{d}\vec{S}
\end{aligned} \tag{2.3}$$

It is important to notice that the equations (2.3) constitute a set of fully coupled non-linear equations. The non-linearity is mainly due to the convective term in the momentum equation, which is responsible for the appearance of turbulence, a spontaneous instability of the flow, whereby all quantities take up a statistical (chaotic) behavior [11]. Other non-linearities are due to the product of the density with the velocity, and could be also derived from non-uniform temperature field, or free surfaces flow.

The fully coupled and non-linear nature of these equations, makes them difficult to be numerically solved. The necessity to resolve the smallest turbulent scale (the so-called Kolmogorov Scale) requires an extremely fine grid[1] and a corresponding small time step. For the case of practical interest, where the Reynolds number is of the order of $10^5 - 10^7$, the Direct Numerical Simulation are out of reach for a long time, based on the current and projected computer capacities [11].

2.2 LES and RANS approach

Due to the prohibitive amount of computational time required for the complete solution of the Navier-Stokes equations with the so called Direct Numerical Simulation (DNS), a large variety of different methods have been developed, to avoid to calculate completely the turbulent field motion.

Similarly to the approach in the DNS, there are the Large Eddy Simulation (LES) methods. With these methods, the turbulent fluctuations are resolved directly in space and time, but only until a certain scale. This allows to relax the requirements on spatial and temporal discretization of the DNS, still maintaining the stochastic nature of the solution. LES methods are currently under investigation for applications in the ICE field, and they result particularly appealing since they allow to simulate the cyclic variations typical of the ICE operations [13, 14]. However, the necessity to simulate a relevant number of engine cycles, together with the need of a well validate combustion model in order to be able to calculate also the expansion stroke, prevents their use in the industrial applications, limiting their exploitation in the research.

Instead of solving the turbulence, equations (2.3) can be

[1]Smaller than the Kolmogorov scale length $\eta = \left(\frac{\nu^3}{\varepsilon}\right)^{\frac{1}{4}}$, where ν is the kinematic viscosity and ε is the turbulent dissipation.

"filtered" to remove the stochastic fluctuations and solve only the average part, and turbulence is introduced through an ad hoc model. A method to "filter" the equations is provided by the Favre Average, by which all the equations are treated by a density weighted average and a fluctuating variable Φ is decomposed into a mean part $\overline{\Phi}$ and a fluctuating part Φ', leading to the Reynolds Averaged Navier-Stokes (RANS) equations. RANS approach is currently used in almost all the industrial applications of CFD in the ICE field, although the LES approach is steadily gaining interest for the reasons mentioned above.

2.3 Turbulence model

As explained in the section above, in case of the RANS approach the turbulence is not directly solved, but "superimposed" to the mean flow through the use of a turbulence model. Turbulence modeling is still nowadays a challenging and growing research field, since the LES and DNS approach do not seem practicable in the next future for the industrial applications. Nevertheless, LES and DNS can provide useful information to further develop the turbulence models. An extensive review of the turbulence models can be found in the book of Wilcox [15] or Pope [16] and in scientific literature. Here a short description of those models of major interest for this work will be presented.

2.3.1 The k-ε model

The k-ε model is based on partial differential equations for turbulent kinetic energy $k \triangleq \frac{1}{2}(\overline{u_i' u_i'})$ and its dissipation rate. u_i' is the generic i component of the velocity obtained after the Favre-averaging, the overbar is used to indicate the averaging and the Einstein summation convention for the repeated indexes has been adopted.

In this model, a conservation equation for the turbulent kinetic energy is written, following the general form of the conservation law expressed in eq. (2.1):

$$\frac{\partial \overline{\rho} k}{\partial t} + \nabla \cdot \overline{\rho} k \overline{\vec{v}} = \nabla \cdot \left(\frac{\mu_t}{\sigma_k} \nabla k \right) - \rho \overline{u_i' u_j'} \frac{\partial \overline{u_j}}{\partial x_i} - \overline{\rho} \varepsilon \qquad (2.4)$$

where σ_k is the Prandtl number connecting the diffusivity of k to the turbulent viscosity[2] μ_t.

In case of high Reynolds number, the turbulent viscosity is correlated to the turbulent kinetic energy and its dissipation by:

$$\mu_t = C_\mu \overline{\rho} \frac{k^2}{\varepsilon} \qquad (2.5)$$

where C_μ is a dimensionless constant.

Closure of the transport equation for the turbulent dissipation ε is difficult due to the presence of many unknown high order terms, but a simplified equation obtained in analogy to that for k was proposed by Launder and Spalding [17]. The equation for ε can be obtained multiplying eq. (2.4) by $\frac{\varepsilon}{k}$, and introducing some model constants. Thus, the equation reads:

$$\frac{\partial \overline{\rho} \varepsilon}{\partial t} + \nabla \cdot \overline{\rho} \varepsilon \overline{\vec{v}} = \nabla \cdot \left[\frac{\mu_t}{\sigma_\varepsilon} \nabla \varepsilon \right] - C_{\varepsilon,1} \frac{\varepsilon}{k} \rho \overline{u_i' u_j'} \frac{\partial \overline{u_j}}{\partial x_i} - C_{\varepsilon,2} \overline{\rho} \frac{\varepsilon^2}{k} \qquad (2.6)$$

where σ_ε is the turbulent Prandtl number[3] connecting the diffusivity of ε to μ_t, and $C_{\varepsilon,1}$ and $C_{\varepsilon,2}$ are model constants.

The "standard values" of the constants, as used in most of the pratical cases, can be found for the first time in the work of Launder and Sharma [18], based on the formulation of the model provided by Jones and Launder [19], which is the one nowadays considered as the "standard" k-ε model.

This model is valid only for fully turbulent flows. Many variants for low Reynolds flow have been proposed [20]. In

[2] Generally a value of 1 is used.

[3] Generally a value of 1.3 is used.

the CFD codes, in case of an application with high Reynolds number for the bulk flow, as in most of the practical cases, one of these models or a wall function is used to solve the boundary layer near the walls. Using the wall function, which is the easiest and most diffuse option in the field of ICE simulations, algebraic functions are then used to represent the distributions of velocity, temperature, turbulence, energy, etc. within the boundary layers [21].

Many variants of the k-ε model have been proposed over the time. An interesting variant for the ICE application is the RNG-k-ε model.

The RNG-k-ε variant

The RNG variant of the k-ε model is based on the renormalization group analysis [22], and allows to overtake the equilibrium assumption of turbulence of the standard k-ε model, which has been developed for stationary flows but shows its limitations in ICE applications, where the flow is transient in nature [23].

An additional term in the transport equation for the turbulent dissipation is included, which is used to take into account the effect of mean flow distortion on the turbulence. Also the standard values for the model constants are slightly different [24]. It has to be noticed that, although the structure of the equations looks similar to the one of the standard model, these are obtained directly from the instantaneous Navier-Stokes equations after applying the renormalization group method, instead of the Favre-averaging.

2.3.2 The k-ω model

This model is a two-equations model as the the k-ε model. In this case, instead of the turbulent dissipation ε, a transport equation for the turbulence dissipation rate ω, inversely proportional to the turbulence time scale, is adopted.

The turbulent viscosity is then related to the turbulence dissipation rate by:

$$\mu_t = \overline{\rho}\frac{k}{\omega} \tag{2.7}$$

The first formulation of this model was presented by Kolmogorov [25], and in its actual formulation is due to Wilcox [15].

The numerical behaviour of this model is similar to that of the standard k-ϵ model, and of course it assumes, like the k-ε model, that μ_t is isotropic.

According to Wilcox, who developed the model, his model is superior to the k-ε model both in its treatment of the viscous near-wall region, and in its accounting for the effects of streamwise pressure gradients [16]. It performs better than the standard k-ε model for low Reynolds flows.

2.4 Spatial discretization

In the finite volume (FV) method, the computational domain is subdivided into sub-domains or "cells", and the Navier-Stokes equations or an approximate form of them, as discussed in the paragraphs before, are solved for each cell.

The collection of vertexes, edges and faces that define each cell is called *mesh*. The degree of difficulty required to generate a mesh for a numerical simulation varies depending on the geometry shape, but usually a considerable effort by the user is required at the mesh generation stage. Mesh definition in the field of ICE simulations is highly time-demanding for the user, considering the further difficulties due to the mesh movement during the simulation. Different approaches for the mesh generation are possible.

Meshes can be classified as structured and unstructured grids. Structured grids are constituted by a regular collection of congruent parallelepipeds. Every cell can be addressed uni-

vocally by using an index for each spatial coordinate (therefore three indexes in case of 3D-domains as in the present work). This regularity allows considerable simplifications in the solver that will work on this kind of grid, at price of less flexibility in meshing complex domains with an irregular shape. On the contrary, in unstructured grids it is not possible to identify each element by mean of a coordinate index, but a connectivity list is used to specify which vertexes define a cell, which can be of irregular shape. In the past, the most common used cells were hexahedral and tetrahedral cells, cut if needed to follow the boundaries shape. In most recent codes, also polyhedral cells are used.

An important limitation, also for regular geometries suitable for structured grid meshing, is that the spatial resolution in case of a structured grid must be constant, preventing the use of a finer grid in the area of higher gradients. To overtake this limitation, a block-structured grid can be used. In a block-structured mesh, the computational domain is subdivided in different regular-shape subdomains, and a structured grid with different resolutions can be used in each domain. A connectivity list is then necessary only at the interfaces, while each sub-domain can be handled as a normal structured grid.

2.5 Solution alghoritms

In the FV method the flow parameters are approximated in terms of cell-centered nodal values. The conservation equations are first integrated over the individual computational cells, using their varying volume as the control volume and transforming the divergence terms into surface integrals using the Gauss divergence theorem. Details on the mathematical procedure and the different discretization techniques can be found for example in [11, 26, 10], and will not be discussed here.

After the spatial and temporal discretization, a non-linear system of algebraic equations is obtained, which can not be solved analytically. Different iterative methods are available, such as the SIMPLE[4] and PISO[5], which are the most used. Since the SIMPLE algorithm is like the PISO algorithm, except the use of a single corrector step and some relaxation factors, only the PISO algorithm will be explained here.

The sequence of stages followed by PISO algorithm at every time step, starting from initial values of the variables field is the following:

1. using the initial pressure, the momentum equations are solved (iteratively) in each direction to obtain a velocity field. This velocity field does not satisfy the continuity equation. The iterations required to solve the non-linear algebraic equations are called "inner iterations", to distinguish them from the "outer iterations", which consist of a repetition of all the steps described, as explained hereafter;

2. other state variables are obtained by replacing the velocity and the pressure in the energy conservation and turbulence energy equations.

These first two steps constitute the so-called "predictor stage". Then, in the "corrector stages", equations are solved as follows:

3. use the continuity equation, with the already obtained velocities, to calculate a new pressure;

4. substitute the new pressure in the momentum equation to obtain a corrected velocity field;

5. other state variables are obtained by replacing the velocity and the pressure in the energy conservation and turbulence energy equations.

[4]Semi-Implicit Method for Pressure Linked Equations, [27].
[5]Pressure Implicit with Splitting Operators, [28].

The number of the corrector steps executed is not predetermined, therefore it is judged from an internal measure of the splitting error. If the calculation of scalar fields such as the turbulence parameters and temperature is required, and they are not strongly coupled to the flow field (velocity and pressure), it is performed in further steps executed after the final flow corrector, otherwise the evaluation of these variables is incorporated in the main predictor/correct sequence.

In order to improve the convergence, a relaxation factor for the pressure is used. It expresses how much the new pressure value calculated at the step 3) of the algorithm will be "blended" with the value of the pressure calculated in the previous outer loop to perform the steps 4) and 5). Relaxation factor r ranges between 0 and 1. A value lower than 1 is generally used, meaning that the new calculated pressure is not directly substituted in steps 2), 3) and 4), but is it blended with the pressure deriving from the previous iteration in a fraction corresponding to $(1-r)$. Obviously more PISO iterations will be required when the relaxation factor is decreased, but the scheme should have an higher stability. In analogy, under-relaxation factors can be defined also for the other variables.

In all the simulations that will be presented, a PISO algorithm was used.

2.6 Peculiarities of CFD codes for ICE applications

Numerical simulations are used to optimize the ICE since more than 20 years. The main peculiarity of ICE simulations is that, for in-cylinder computations, the mesh has to change over the time, to reproduce the piston and valve movements.

The change of the mesh over the time constitute a big effort for the computational code, which has to incorporate

or to be able to communicate with an appropriate algorithm capable to manage automatically the mesh changes, since it is obviously not feasible to modify the grid and remap the solution manually at each time step.

Different codes, which handle the mesh changes with different approaches, have been developed over the times.

Historically, one of the first codes developed specifically for the ICE simulations is KIVA, written at Los Alamos Laboratories [29]. Until version 2, the code was able to deal only with structured grids, making it suitable only for simple geometries such as the combustion chamber of Diesel engines. From version 3 it is able to manage also block structured grids [30], and from version 4 also unstructured grids [31], but due to historical reasons it is still nowadays mainly used in the field of Diesel engines. However, due to the availability of its source code, many different subversions and new models, especially for spray and combustion simulations, were implemented on KIVA also from academic institutions, and the code is nowadays quite spread amongst the industry [32].

A block structured mesh, and in the last version also a polyhedral unstructured mesh, is used by Es-ICE, a mesh-generator code written to work in conjunction with the general purpose CFD code Star-CD. Star-CD was historically one of the first commercial software dealing with the generation of a self-moving mesh suited also for complex geometries. In combination with its package for the engine grid generation Es-ICE, Star-CD has gained a considerable market share in the automotive industry. Mesh generation in Es-ICE is based on the creation of a 2D-template reproducing the main peculiarities of the three-dimensional geometry such as valves, squish area and so on. The 2D-template is then extruded in a 3D-template, which can be projected on the actual three-dimensional geometry or cut with it [33]. The grid so obtained is then modified automatically from the code, first stretching

or compressing the cells to take into account the movement of the piston or the valves, and eventually adding or deleting cell layers when the mesh skewness due to the grid deformation is above an acceptable value.

The code, born as mentioned as a general purpose CFD code, had at the beginning very few ad hoc models for ICE simulation requirements, such as the spray injection or the combustion. For this reason, many models have been implemented directly from the users, leading to a wide variety of different models and implementations used in the industry for these purposes.

A more recent software, specifically developed for ICE simulations, is Fire by AVL. Its peculiarities are the implementation of numerous models dedicated to ICE applications, as well as a mesh generator capable to deal with complex geometries typical of ICE. The meshing process is based on the generation of four different grids for each different configuration of the combustion chamber, i.e. one grid with both the intake and exhaust valves open, one grid with the intake open and the exhaust closed, one grid with exhaust open and intake closed and one grid with both the intake and exhaust valves closed. The code can then switch autonomously between the different grids, and modify them to take into account the movement of the piston and the valves. Despite the easier Graphical User Interface, maybe due to its later introduction on the market, AVL Fire seems to be less spread than Star-CD/Es-ICE in the automotive industry.

Finally, a software that is rapidly gaining market share in the automotive industry is Converge-CFD, by Convergent Science. Converge adopts an innovative meshing approach, by which a cartesian structured mesh is created completely automatically starting from the surface geometry file [34]. An adaptive mesh refinement (AMR) or a static refinement in the area of major interest is allowed and automatically man-

aged from the code. The innovative approach in the meshing could seem critical due to the absence of prismatic cells in the boundary layer region, and do not allow a "feature oriented" meshing, except for the embedding or AMR mesh improvements in the critical areas. However, it grants a considerable reduction in user efforts for the intensive time consuming mesh preparation.

In the scientific literature, some attempts can be found, which present a code that allows the grid movement in a open-source environment, like for example Open-Foam. An example with quite promising results can be found in the works by the ICE research group of "Politecnico di Milano" [35].

Although parts of the present research was developed with AVL Fire and Converge-CFD, the main code used for this work is Star-CD, for which a larger database of previous simulations and an higher know-how was already present in the institutions where this work was developed.

Chapter 3

Optical techniques

The aim of this chapter is to present the main techniques used in the present work to extract experimental data necessary to validate the proposed CFD models. Optical diagnostic has an extremely wide application area and important applications also outside the field of ICE. This chapter will focus only on the techniques that are relevant for the present work. A more exhaustive discussion can be found in specific books [36] or scientific literature.

3.1 Optical engines

Before reviewing some optical techniques, a short discussion about the engines used for optical applications is necessary. It is important to bear in mind that the structure of these engines differs from the standard "all-metal" engines[1]. Sometimes a simplified piston bowl geometry and other differences in the combustion chamber geometry, especially in the combustion chamber roof, are used to allow or maximize the op-

[1] In the following, standard engines will be referred to also as "thermodynamical" engines, to underline the fact that the combustion takes place inside them.

tical access. Even when the combustion chamber geometry is perfectly reproduced, non-standard piston rings manufactured from special materials are used, due to the need for "dry-run" the engine to avoid fouling on the optical devices. This generally leads to engine blow-by considerably higher than in standard engines.

Furthermore, optical-access engines rely on the replacement of a number of metal engine parts by "transparent" windows, which allow visual access to the combustion chamber. The windows are typically made from quartz and/or sapphire. The choice of an appropriate material depends not only on mechanical properties but also on optical properties. The use of materials such as quartz, sapphire and titanium in optical engines has a significant impact on engine combustion characteristics, due to the lower thermal conductivity of these materials in comparison with aluminum, steel or cast iron used in the standard engines.

Generally, the operating range of the engine is reduced to lower loads and lower speeds, due to structural limits and also technological limitations of the optical devices (e.g. the sampling frequency of the camera).

Very often a single-cylinder engine is used, having the cylinder head derived from the standard engine, in order to keep the geometry as much realistic as possible. Otherwise, a full engine could be used, providing endoscopic access to one (or more) of its cylinders.

In the present work a single-cylinder engine was used, equipped with a glass liner and 4 valves per cylinder with adjustable timing, fed through an external boosting system. Intake and exhaust ports are realized in rapid prototyping, in order to allow their fast modification during the design evolution. Due to its characteristics, the engine can be operated only in motored mode, hence without combustion. The electrical compressor in the feeding system allows to reproduce

the same in-cylinder pressure as in the thermodynamic engines, which are turbocharged. Two different engine geometries, one corresponding to a single-cylinder research engine, and the other to a 4-cylinder passenger car engine, were investigated in this work. Geometrical details are reported in chapter 5.

3.2 Overview of the optical techniques of interest for ICE

As explained before, we will focus only on the techniques of interest for this work. However, an overview of the main laser techniques available and their application is presented in table 3.1 [37]. In particular, only techniques for flow and spray analysis will be reviewed here, omitting all the techniques related to combustion diagnostic, since these are not of interest for this work.

In addiction to the laser techniques, a large number of endoscopic methods are available. They use an optical access to monitor the charge formation and combustion process by using an endoscopic camera or fiber optical sensors [38].

3.3 Flow visualization

Flow motion in the cylinder, and consequent turbulence level, are of extreme importance in determining the mixture formation and combustion process in the engine. Thanks to the diffusion of CFD, it can be nowadays simulated. However, measurements of the turbulence level and air velocity in the cylinder were common considerably before the large diffusion of CFD, and still nowadays they play an important role for models development and validation.

Table 3.1: Overview of the laser-based in-cylinder analysis techniques [37].

Method	**Object**	**Information**	**Sensors**
PIV, Particle Image Velocimetry	Seeding particles, fuel droplets	Flow field	Camera
LDA, Laser Doppler Anemometry	Particles, droplets	Local flow velocity	Photodiode, multiplier
PDA, Phase Doppler Anemometry	Droplets	Droplet size	Photodiode, multiplier
LIF, Laser Induced Fluorescence	Fluorescent molecules	Species concentration	Camera
LII, Laser Induced Incandescence	Soot particles	Soot distribution	Camera
Raman scattering	Molecules	Concentration, temperature	Multiplier
Light absorption	Molecules, particles	Concentration	Photodiode, multiplier

3.3.1 Hot Wire Anemometry (HWA)

Hot wire anemometry (HWA) is one of the first experimental techniques used to measure the velocity in the combustion chamber. Hot wire anemometers consist of a very thin wire (of the order of several micrometers) electrically heated. Air flowing past the wire has a cooling effect on the wire, and measuring the current necessary to keep the wire at constant temperature (constant temperature anemometer), or measuring the difference in resistance of the wire due to the change of

temperature (constant voltage or constant current anemometer), it is possible to determine the flow velocity. Thanks to the good dynamical response of the anemometer, it is possible to measure also the turbulent fluctuations of the velocity, obtaining thus also information on the turbulence.

This technique has obviously limitations in determining the flow direction, but combining different wires and appropriate masking, it is possible to partially overtake this weakness. Nevertheless, this technique has been nowadays surpassed by optical approaches.

3.3.2 Laser Doppler Anemometry (LDA)

The modern equivalent of HWA is the Laser Doppler Anemometry, since as the HWA it provides local information on the fluid velocity. It is based on the Doppler shift occurring to laser light, when it is scattered from a particle. Two different laser beams crossover in the measure volume, generating a fringe pattern. When a particle passes through the measure volume, it generates a modulation of the fringe pattern depending on its velocity, which can be measured directly from the frequency of the modulation of the light signal. Since both the beams are generated from a single laser with a splitting optic, a Brag-cell is generally used to increase the frequency of one of the signals, in order to obtain a frequency-particle velocity response which is monotone (otherwise it would be an even function, not allowing to discriminate the direction of the velocity).

In case a further receiver is added, capable to detect the light of a third beam reaching the particle from a different angle, the technique is extended to Phase Doppler Anemometry, allowing to measure also the particle size. In fact, measuring the phase shift of the two signals, it is possible to determine the different optical paths of the two beams, which depends on the particle size.

Both the techniques can be used to measure the flow velocities, inserting tracer particles in the flow, or to characterize the spray droplets, in addiction to the techniques described in paragraph 3.4.

3.3.3 Particle Image Velocimetry (PIV)

PIV is a technique that allows to visualize the motion field on a plane. Unlike conventional measurement techniques for turbulence, such as HWA and LDA which are single-point methods, the PIV technique allows the analysis of the whole field, and more importantly the instantaneous flow field.

Essentially, PIV measures the average velocity of flow over a finite period between two particle images, and the results are then used for spatial correlation analysis [36].

The typical optical configuration of a PIV set-up includes:

- a light source that usually is a double-pulse laser;
- light-sheet optics including beam combining optics, a beam delivery, and light-sheet formation optics;
- tracer particles;
- high speed camera and recording media.

In its simplest form, the flow is illuminated with a double-pulsed light-sheet. The first pulse of the laser records the initial positions of the particles onto the first frame of the camera. The light scattered by the particles, and therefore the final positions due to the movement of the flow field, is recorded onto the second frame of the camera. The mean particle displacement vector in each small region of the flow is finally determined by performing a spatial correlation of the particle image field in that region [39]. More in detail, PIV images are analyzed by subdividing the image into small interrogation

regions. Each interrogation region contains many particle image pairs. It is not possible to find individual matching pairs, because the displacement is greater than the mean spacing between particle images. Therefore a statistical method is used to find the particle image displacement [40].

It is important to notice that the presence of tracking-particles is necessary, due to the optical homogeneity of the air. Ideal tracers do not alter the flow or the fluid properties, and follow the motion of the fluid precisely. The accuracy of the velocity field determination is ultimately limited by the ability of the scattering particles to follow the instantaneous motion of the continuous phase. A compromise between reducing the particle size to improve flow tracking, and increasing the particle size to improve light scattering is therefore necessary. The choice of an optimal diameter for seeding particles is a compromise between a low inertia of the tracer, requiring small diameters, and a high signal-to-noise ratio (SNR) of the particle images, which takes advantage of large diameters. Also the density of the tracers is a parameter that needs to be tuned appropriately [36].

3.4 Spray visualization

In modern DI engines, fuel spray plays a crucial role in determining the engine performances, intending with performances also the pollutant emissions that are nowadays of crucial importance due to severe legislation. Injection events last only few milliseconds, but spray penetration and shape obviously have an important role in determining the fuel mixture formation. Optical techniques for the spray visualization help in gaining a better understanding of the complex phenomena involved in the spray atomization and evaporation, and give important information on the crucial injection phase.

3.4.1 Direct imaging

Direct imaging is the simplest technique to visualize the spray, consisting, roughly, in taking pictures of the spray. Despite this apparently simple explanation, there are different technological challenges that make the direct imaging a complex technique. Firstly, the injection event in ICE lasts only few milliseconds[2]. For this reason, high speed cameras are required. Otherwise, a single-shot camera can be used, equipped with a synchronizing device, to reconstruct the injection event taking images at different times of different injection events.

Secondly, due to the short exposition time of the camera, an intense light source is required. Light sources can be either continuous or pulsed. Continuous and pulsed light sources are available both as lamps and as lasers, but lasers provide an higher brightness generally at price of an higher cost.

Finally, an automatized method for the imaging post-processing has to be defined. Using specific image post-processing algorithms, it is possible to detect the spray contour over the time, to calculate the penetration, and even determine the droplet size distribution in the well-dispersed region of the spray, where it is possible to recognize the single droplets. Of course the visualization window and camera resolution have to be set properly, according to the droplets size. In case a parallel beam of light is produced, using an appropriate optic, the direct imaging is also known as shadowgraphy or Schlieren imaging.

[2]To have a rough estimation, it can be considered that at 6000 rpm a whole engine cycle lasts 20 ms, thus the intake stroke and the compression stroke, during which the injection has to take place, last approximately 10 ms.

3.4.2 Mie-scattering

The direct imaging method presented before provides information that are integrated along the line of sight in the measurement region. However, using a laser-sheet it is possible to "isolate" a plane of the spray and obtain information only for that plane. The scattered light[3] is proportional to the square of the diameter, but since it depends also on the drop concentration and size distribution, Mie-scattering can be used only to extract qualitative information on the spray liquid mass distribution on the plane, that results to be proportional to the intensity of the scattered light.

3.4.3 Laser Induced Fluorescence (LIF) and Laser-Sheet Droplet sizing (LSD)

If fluorescence is induced by laser, and detected with an appropriate optic instead of the scattering, the technique is called Laser Induced Fluorescence, or LIF. Unlike the Mie-scattering, this technique can be used also to detect the vapor phase, although due to the different range of LIF intensity, it is difficult to detect both the liquid and the vapor phases simultaneously. Thanks to the similar setup required, both the Mie-scattering and LIF can be used together, with two separate optical setups or an image doubling optical setup.

Since the signal deriving from LIF is proportional to d^3, while the intensity of the Mie-scattering is proportional to d^2, from the ratio of the two signals is possible to derive the droplets Sauter Mean Diameter SMD, with the so-called Laser-Sheet Droplet sizing (LSD) approach. The SMD is in fact

[3]It is called Mie-scattering when the diameter d of the particle which scatter the light is much bigger than the wavelength λ of the scattered light. For visible light, Mie-scattering occurs with droplets bigger than 0.5 μm.

defined as:

$$\text{SMD} \triangleq \frac{\sum_{i=1}^{N} d_i^3}{\sum_{i=1}^{N} d_i^2} \tag{3.1}$$

where N is the number of the droplets and d_i their diameters. SMD is an important characteristic dimension of the droplets, since it is given by the ratio of volume and surface. Therefore, it is important to characterize the evaporation behavior of the droplets and their penetration, both depending on the mass (thus their volume) and the surface area [41].

LSD requires a calibration with another technique such as the Phase Doppler Anemometry (PDA), capable to give the absolute size of a droplet without any calibration. LSD measurements are more efficient for narrow droplet size distributions, since both the Mie-scattering and the LIF signals are biased towards droplets of bigger dimensions.

3.4.4 Laser diffraction

Laser diffraction is a widely used technique for particle sizing. It is based on the Fraunhofer diffraction as the Mie technique. When a laser beam encounters a particle, it is diffracted at an angle inversely proportional to the particle size. Measuring the diffraction angle, it is therefore possible to determine the particle size. This technique operates on an ensemble of particles which passes through a broadened beam of laser light. Analyzing the peak and the minimum of intensity of the diffraction pattern, it is also possible to extract information on the particle size distribution.

Chapter 4

Spray characteristics for gasoline engines

The atomization process plays a fundamental role in determining the engine performances and pollutants emissions. A big effort to understand in details the phenomena involved was made over the decades, allowing to gain a deep knowledge of the complex mechanisms involved in the spray atomization, which constitute however still nowadays a challenging research field.

This chapter will focus on gasoline direct injection engines, referring to the specific literature [42, 43] for a more extensive discussion.

4.1 Combustion system concepts

Many different combustion system concepts have been experimented over the time, and several of them still compete on the market. In a schematic classification, a first distinction can be made between engines working with an homogeneous charge, and those adopting a stratified charge. Engines operating with an homogeneous charge, despite the direct injection,

try to obtain a completely homogeneous charge in all the working conditions, which should ideally not differ from that of a PFI engine. The air-fuel equivalence ratio (often called λ in the european literature) is almost always near to 1, except in case of enrichment at full load or for the cold start. On the contrary, engines operating with a stratified charge work with an overall lean mixture (i.e. λ higher than 1), with a fuel stratification by which a rich, and thus easily ignitable and stable burning mixture, is created near the spark plug. Currently, even the engines working with a stratified concept switch to the homogeneous mode at high load [44]. Other combustion concepts, like for example the Homogeneous Charge Compression Ignition (HCCI), are under investigation since long time, but at the moment no production engines are available on the market adopting this concept. Because this topic is beyond the aim of this chapter and of the present work, it will be not discussed further.

A second classification can be made according to the injector position in the combustion chamber. Assuming that the spark plug is always positioned near the center of the combustion chamber to enhance a symmetrical flame propagation, the injector can be positioned near the spark plug, thus in central position, realizing the so-called "narrow spacing". Otherwise, the so-called "wide spacing" or side injector configuration can be adopted, positioning the injector on a lateral side of the combustion chamber. Generally the intake side is chosen, to protect the injector from too high temperatures which lead to faster injector coking. Both the configurations show pros and cons in terms of packaging, combustion performances and costs; for a detailed discussion see [4]. At the moment both the concepts are successfully present on the market.

Finally, a further classification can be made considering the way in which the homogeneous or stratified charge is obtained. According to the relative position between the injector,

the spark plug and the cylinder and piston wall, the required stratification can be obtained by mean of: the spray shape, the liquid-driving surfaces on the piston crown, or the air motion in the cylinder that transports the fuel in the combustion chamber. These are called respectively "spray guided", "wall guided" and "air guided" combustion systems. This is however a simplification needed to schematize the process, because there is obviously always a strong interaction between the air motion in the cylinder, the spray shape and the liner and piston walls.

4.2 Injector types

In modern direct injection engines fuel pressures up to 200 bar are used. Together with the traditional solenoidal-controlled injectors, since 2006 also piezo-electric injectors are available on the market [45]. Despite the actuation system, injectors can be differentiated by their nozzle type and the corresponding spray pattern they produce. The spray pattern determines the characteristics of the spray emerging from the nozzle, namely the cone angle, the spray penetration and the droplets size distribution. These parameters should be carefully matched with the injector positioning, the combustion chamber design and the combustion principle in order to optimize the mixture formation process.

Multi-hole injectors are characterized by spray jets that come from different holes (generally from five to seven), and emerge separate from the injector tip. Due to the chamber pressure and air motion conditions, the jets can collapse at a certain distance from the nozzle. However, except in flash-boiling conditions [46], it is possible to design the hole positions in order to obtain the desired pattern to minimize the wall and valve impingement and optimize the mixture formation. Injector holes are more sensitive to coking phenomena

than in the other injector types.

Swirl injectors are characterized by a narrow jet with a strong tangential component velocity, which creates a compact fuel cloud. The penetration is generally lower than the one of a multi-hole injector, but the spray shape is more dependent on the chamber conditions [4]. They were largely used in the first GDI engines, while nowadays multi-hole injectors are generally preferred, due to the higher actuation pressure, which allows to perform multiple injections.

The outward opening injectors, or "pintle" injectors, are characterized by a reduced spray penetration and very small droplets size. Together with the good reproducibility of the spray, and the very small actuation time – obtained through the piezo-electric actuation which is generally adopted in this injectors – they are well suited for stratified combustion process in spray guided injection concept. Furthermore, they are less sensible to coking than multi-hole injectors.

In figure 4.1 a comparison of the spray emerging from the different injector types, with injection pressure of 200 bar and back pressure of 1 and 6 bar, is presented.

4.3 Spray atomization process

The function of any injector is to atomize the fuel in small droplets, in order to increase the surface/volume ratio and thus to enhance the evaporation. As soon as the fuel interacts with the air in the combustion chamber, the initially continuous liquid emerging from the injector is shattered into liquid droplets and ligaments, in the so-called primary breakup. The liquid particles formed, are then deformed by the action of aerodynamic forces and break up into smaller and smaller droplets, during the so-called secondary breakup. This phenomenon continues until the effect of cohesion due to the surface tension prevails over the aerodynamic forces.

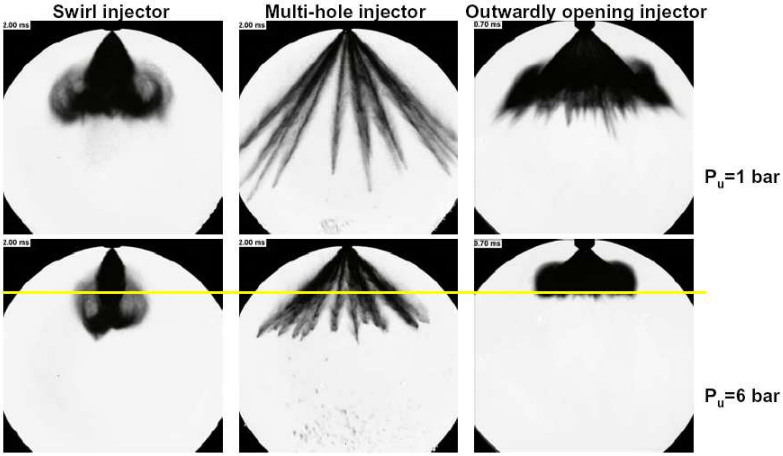

Figure 4.1: Spray patterns of different injector types [47].

4.3.1 Primary breakup

The jet primary breakup is the physical process that leads to the detachment of drops and ligaments from the liquid jet surface. It depends on the interaction of many complex phenomena such as the aerodynamic interaction with the air, the turbulence and the cavitation inside the nozzle.

The primary breakup has been studied for more than a century, and many theories are nowadays available. The first experimental investigations on jet flow phenomena were carried out by Bidone [48] and Savart. A first theoretical approach can be found in Plateau [49], cited by Rayleigh in his first mathematical description of the jets [50]. Weber [51] extended the study of Rayleigh to the viscous liquids, and his studies were experimentally confirmed by Haenlein [52].

Some adimensional numbers help in describing the phenomena involved, which depend on inertial forces, aerodynamic forces and surface tension acting on the jet. The Weber number We can be expressed as the ratio between the inertial

force and the surface tension force:

$$We = \frac{\rho v^2 d}{\sigma} \tag{4.1}$$

where ρ is the liquid density, v is the droplet velocity, d is a characteristic length such as the droplet diameter, and σ is the surface tension. The Ohnesorge number Oh relates the viscous forces to inertial and surface tension forces, by:

$$Oh = \frac{\mu}{\sqrt{\rho \sigma d}} \tag{4.2}$$

where, apart the symbols already defined, μ is the liquid dynamic viscosity.

Extending the Ohnesorge's work, Reitz [53] showed that the breakup regimes can be classified into four different types, according to the ratio between the droplet Ohnesorge number and the Reynolds number, as shown in the graph of fig. 4.2.

In the Rayleigh regime, the breakup is caused by asymmetric instabilities amplified by the surface tension forces. Droplets sizes exceed the jet diameter.

The first wind-induced breakup is due to the surface tension effects amplified by aerodynamic forces, which induce a static pressure distribution across the jet enhancing the breakup. Drops diameters are about the same as the jet diameter.

The second wind-induced breakup regime is typical of low-medium pressure injection systems of GDI engines. Shear stresses due to the liquid to air relative velocity enhance the production of short-wavelength surface waves. Gas inertia is then the driving agent of their unstable growth, being limited by surface tension and liquid viscous forces. Breakup occurs several diameters downstream of the nozzle exit, and average drops diameters are much smaller than the jet diameter.

The atomization regime is typical of direct injection Diesel engines with high pressure injection systems. A high speed jet emerges from the orifice in a compact continuous form, but

it is disintegrated in the immediate vicinity of the atomizer into droplets varying greatly in size. Average drops diameters are much smaller than the jet diameter. The relevant forces in this regime are the internal stresses due to turbulence or cavitation, and liquid inertia.

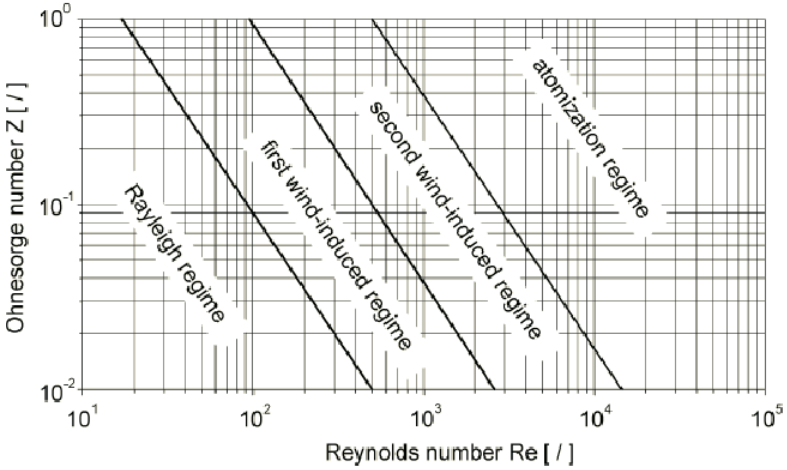

Figure 4.2: Classification of the modes of disintegration [54].

4.3.2 Secondary breakup

After the primary breakup, droplets moving in the surrounding gas are subjected to the inertial and aerodynamic forces and a non-uniform pressure distribution can arise on their surfaces. The droplets are deformed and can incur in the secondary breakup. The relevant forces in this physical phenomenon are those related to surface tension, viscosity, inertia and surface instabilities responsible for waves growth.

A possible classification can be made considering different ranges of droplets Weber number. The transition Weber number between a regime and another is not univocally reported

in literature [55, 56], nevertheless it is well established that four different regimes can be identified, at increasing Weber numbers.

At low Weber numbers (less than 20-40), the bag breakup takes place. Drop breakup is due to the deformation of the droplet in a bag-like structure that disintegrates after that a critical value of deformation is reached.

At intermediate Weber numbers (20-100), there is a transitional regime in which droplet breakup is due to both droplet deformation typical of the bag breakup, and filament stripping typical of the stripping regime.

At high Weber numbers (between 100 and 800-1000), the breakup occurs in the stripping regime. After an initial deformation, a sheet is formed at the periphery of the droplet and it evolves into ligaments that are stripped from the droplet, which gradually reduces until it is completely fragmented, or until a diameter at which aerodynamic forces are negligible is reached. Different physical explanations of the phenomenon are available in literature [43], but it seems that the gas phase inertia causes the periphery of the deformed drop to be deflected in the direction of the flow, thereby forming a sheet. After that, the sheet breaks into ligaments and then individual fragments. This mechanism seems to be confirmed by recent numerical simulations [57], as reported by Guildenbecher in [43].

At very high Weber numbers (larger than 800-1000) finally, the catastrophic regime appears. It is characterized by the presence of both Kelvin-Helmholtz (i.e. parallel to the droplet-air interface) and Rayleigh-Taylor (i.e. perpendicular to the interface) instabilities, respectively with lower and higher wavelengths and amplitudes. This regime is unlike to occur with the injection velocities typical of GDI engines (of the order of magnitude of 10^2 m/s).

A schematic illustration of the different secondary breakup

regimes is presented in fig. 4.3.

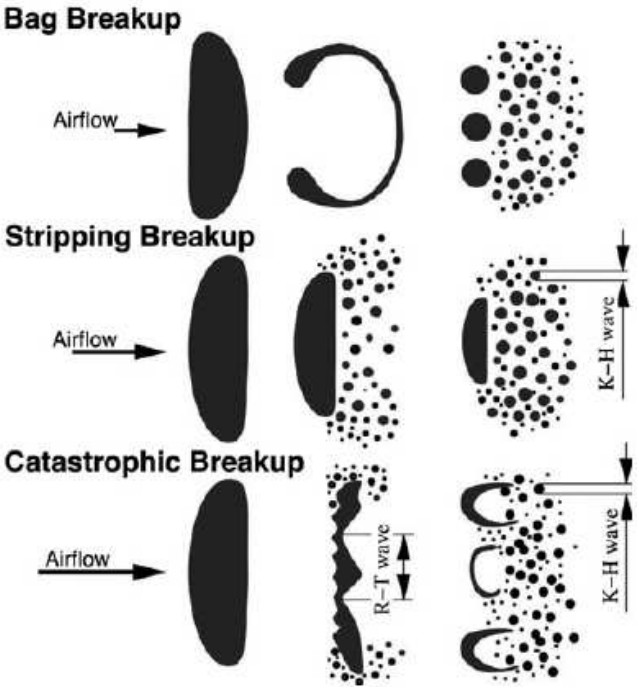

Figure 4.3: Scheme of the secondary breakup regimes [43].

Chapter 5

Cold-flow simulations

In this chapter the cold-flow[1] simulations performed in this work will be explained in detail. In particular, after the explanation of the main simulation settings and the reasons for their choice, the results obtained using different turbulence models and different solver settings will be presented.

This part of the work consists mainly in the comparison of the results obtained through CFD simulations with PIV measurements. A great effort was made on the the comparison of the mean flow and turbulence level with experimental data, because the reliability of the cold-flow simulations is crucial for all the CFD activities related with the engine development process. In fact, the CFD cold-flow simulations serve as basis for the injection simulations performed later on, and they are used to assess the optimal port and combustion chamber shape. Furthermore, the turbulence level can be of interest since it can be used as input for 0D predictive combustion models [58, 59, 60].

As it will be presented in this chapter, the accuracy of the cold-flow simulations can be deeply affected by the choice of

[1] With the term cold-flow simulation we refer here to simulations without injection and without combustion.

the model settings, and in particular the turbulence model and the solver schema. The cold-flow simulations are nowadays routinely used in the engine development process, especially with the RANS approach, but it is hard to find in literature comparisons of CFD results with flow optical measurements.

5.1 Experimental setup

Optical measurements with PIV technique were performed in a single cylinder optical engine with glass liner and piston and intake and exhaust pipe in rapid prototyping, whose geometry corresponds identically to the one of the investigated engine. Due to the fragility of the glass liner, the optical engine can be operated only in motored mode.

The PIV system consists of a double cavity diode pumped solid state Nd:YLF Laser (Quantronix Darwin Duo) operated at 527 nm wavelength and a high speed CMOS camera (Photron Fastcam SA-1). In order to fit the laser pulses into the camera frames a high speed synchronizer (ILA GmbH) was used. Image processing is performed with DaVis software (La Vision), investigating two vertical planes, one being the tumble plane in the cylinder mid-section, and the other the cross tumble plane.

The flow seeding is performed introducing Di-Ethyl-Hexyl-Sebacat (DEHS, $C_{26}H_{50}O_4$) through an aerosol generator Topas ATM 210 in particles of around 1 μm, resulting in a Stoke number lower than 0.005. The homogenization of the particles is performed in a box of approximately 8 l volume located before the intake system of the engine.

5.2 Simulation settings

During the simulation setup with a commercial CFD software, many options are available in terms of differencing scheme,

numerical setup, boundary definition, domain initialization, specific submodels activation and constants definition.

It is important to notice that each setting affects the final result, although not all the settings have the same relevance to obtain a correct result, and sometimes more than one option would be correct. For this reason, it is fundamental to be able to keep trace of all the settings used in the simulation, otherwise it would be never possible to reproduce again the same result.

Furthermore, also the comparison between simulations adopting different geometries, valve timings, start of injection (SOI) or other engine related parameters, is really meaningful only when all the simulations are obtained with the same settings. Although some ad hoc settings can be used in particular situations, a meticulous attention should be paid when comparing results obtained with different simulation setups.

With text-based software, like for example Kiva or Converge[2], it is easy to keep trace of all the settings used in the model, since they are saved in a text file which can be easily copied and used as template to set up another simulation. However, in a Graphical User Interface (GUI) based software, like for example Star-CD, the model settings are saved directly in the GUI, and they cannot be directly transferred to another simulation[3].

However, Star-CD gives the possibility to provide the settings for the model in a textual mode, and this possibility has been exploited to create a shell-script based program in order to completely setup the calculation. The script accesses to some libraries where the different settings are saved, like for

[2]Although starting from version 1.4 Converge have a graphical interface to support the model settings, its core is still based on text input files.

[3]Until the current version (4.18), it is possible to export all the used settings in a text file, but it was observed that sometimes the transcription is not complete and the use of this feature is error-prone.

example the fluid properties, the model constants, the scalar variable definition and so on, and creates the complete model with a reduced number of inputs required from the user in text form. This guarantees that each simulation is always set in the same way.

5.2.1 Fluid definition

As well known, PFI engines intake a mixture of fuel and air, since the injection occurs in the intake port, while the DI-engines are fed only with fresh air and in case residual gases present in the intake. The fluid properties required to simulate a PFI engine are thus depending from the air-fuel ratio, while in DI they can be considered constant[4].

At the end of combustion, the combustion chamber is full of residuals, and if we assume in first approximation a complete combustion, it means the properties of the fluid in the combustion chamber or in the exhaust ports have to be calculated once again considering the air-fuel stoichiometric ratio. In case the air-fuel equivalence ratio[5] is larger than 1, the presence of unburned air in the exhaust must be taken into account when giving the fluid properties, while on the contrary in case λ is lower than 1 the presence of unburned fuel has to be considered.

The CFD code used in this work requires to specify the molecular weight, the coefficients of polynomials for molecular viscosity, specific heat and conductivity dependence from temperature, from which all the other properties (e.g. density, enthalpy or entropy) can be derived. FEV uses a database

[4]The fluid properties depend of course on pressure and temperature, but this dependence is directly considered in the CFD code. Constant here means not dependent from the specific case setup.

[5]We use in the present work the "european" convention of air-fuel equivalence ratio, i.e. the "lambda" $\lambda = AFR/AFR_{stoich}$ where AFR is the air-fuel ratio, $AFR = m_a/m_f$ with m_a and m_f respectively the air mass and the fuel mass in the mixture.

of these properties to define the exhaust gas settings obtained considering a combustion with different air-fuel equivalence ratio (ranging from 0.5 to 2.0). However, since this work deals with the comparison of CFD simulation with a motored glass-engine, no residuals or fuel mixture were required for the operating fluid definition, which was only standard air.

5.2.2 Simulation boundary conditions

Different choices for the boundary conditions are possible when dealing with compressible fluids at low Mach number and a computational domain with one inlet (intake port at the flange connection with the runner, the intake runner or the intake manifold) and one outlet (the exhaust port).

The inlet can be defined fixing the mass flow by providing the fluid density and the velocity perpendicular to the inlet, assuming a uniform distribution, or fixing the total pressure and temperature on the boundary surface. Outlet conditions are generally defined in terms of static pressure and temperature at the boundary surface.

In this work, the choice of defining the pressure at the inlet instead of the mass flow was preferred. Dealing with comparison with experimental data obtained from a single-cylinder engine, it is straightforward to use the pressure obtained from the pressure sensor at intake and exhaust location, in case available. Although this is actually a static pressure and not a total pressure, the error committed is negligible, especially for the purpose of the present work where the aim is to compare the motion field with the experimental data.

When experimental data are not available, and in case a 1D model of the engine is accessible, boundary conditions can be determined through the 1D model. In this case, also the mass flow at the boundary could be easily obtained. However, the choice of the pressure allows to calculate the mass flow directly in the 3D code, with the advantages derived from a

more detailed geometry description.

It is important to properly choose the CFD domain to be simulated. When data from experimental sensors are used, the boundary location should correspond to the effective position of the pressure sensor, because otherwise a spatial shifting of the pressure waves is introduced. However, it should be kept in mind that at the pressure boundary an "artificial" complete reflection of the pressure waves is introduced, and if the boundary is too near to the intake valves, this could affect the results. Furthermore, the part of the intake system modeled should be large enough that, in case of backflow, no residuals are lost through the boundary.

When no experimental data and no 1D model of the engine are available, the CFD model should consider, especially for the intake side, the geometry until a position where the pressure can be assumed reasonably constant. In fact, it is well known that the pressure waves at the intake deeply influence the operation of an ICE, especially if naturally aspirated [61]. On the contrary, except for valve timings with high valves overlap, the exhaust pressure can be assumed constant at its mean value, even when the boundary location would not allow this hypothesis, because it has a minor impact on the results.

Also the turbulence must be defined at the boundaries. In this work, the turbulence was defined in terms of turbulence intensity, assumed to be equal to 10% of the mean velocity at the boundary, and the turbulence length scale was assumed to be 0.1 times a characteristic length, defined as the equivalent diameter at the inlet or the outlet. The same assumption was also used for the turbulence initialization.

Furthermore, the temperature of all the wall boundaries has to be specified. Once again, if a 1D model of the engine is present, an approximate indication of these temperatures can be derived directly, otherwise some values derived from the experience are required. Although this can slightly affect the

volumetric efficiency, the impact on the flow field is negligible, and thus is not relevant for the present study.

5.2.3 Solver settings and turbulence models

As every commercial CFD solver, Star-CD offers a large choice of differencing schemes to be adopted for the governing PDE system solution. Among others, the MARS scheme (Monotone Advection and Reconstruction) is based on the REA (Reconstruct-Evolve-Average) algorithm [26]. MARS is a multidimensional second-order accurate differencing scheme [21]. According to the Software provider (CD-Adapco), amongst all the schemes available, MARS possesses the least sensitivity of solution accuracy to the mesh structure and skewness, and for this reason its use is suggested. MARS has been proved to be generally the most stable method.

A comparison of MARS with the well known Central Difference method (CD) will be presented in this work. It should however pointed out that, although the use of CD was unproblematic with the old version of the code, with the latest version a small blending factor is required, leading to a larger diffusion [11].

As explained in section 2.2, a RANS approach was used in this work. Different turbulence models available in the commercial software were tested, and the results will be discussed in this chapter. In particular, the standard k-ε and k-ω were investigated, as well as the RNG variant of the k-ε. The use of the k-ε model is well established for ICE engine simulations [62], in particular in its RNG variant, while the k-ω was investigated since it is another common 2-equations turbulence models. In all cases the standard values for the model constants were used [63].

Generally in the in-cylinder cold-flow simulations the attention is focused on the intake stroke and the compression stroke.

5.3 Results

Two different engines were investigated. Engine 1 is a four-cylinder engine designed for the series production, while Engine 2 is a single-cylinder research engine. For both the engines a glass liner and piston were built, as well as rapid prototyping intake and exhaust runners, in order to be investigated through the optical measurements. The motored optical engine is in fact designed to completely reproduce the combustion chamber and the intake and exhaust ports and runners of each engine, as shown in fig. 5.1 [64].

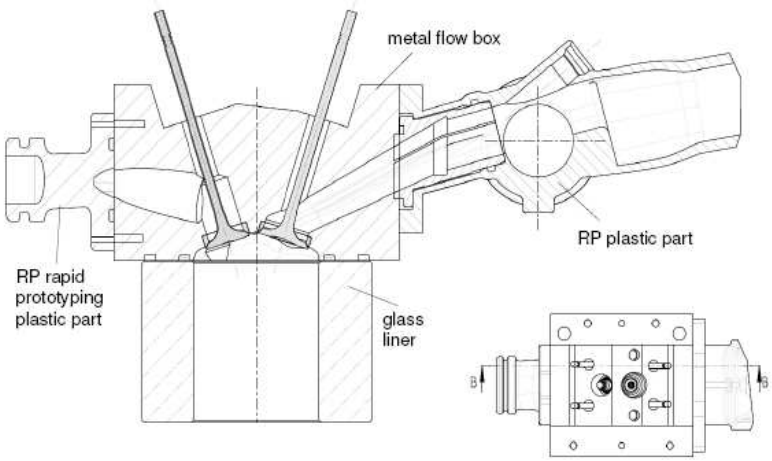

Figure 5.1: Design of the motored optical engine.

The test-bench has an electrically driven compressor which permits to pressurize the intake system, allowing to reproduce different operating conditions. Also the engine speed can be changed, but since 1500 rpm is the maximum operating speed, all the tests here presented were performed at that speed.

A short summary of the main geometrical characteristics of the two investigated engines is presented in tab. 5.1. For both

Table 5.1: Main geometrical data of the two investigated engines.

	Engine 1	**Engine 2**
Bore	73 mm	75 mm
Stroke	90 mm	82.5 mm
Compression ratio	10	10
Intake valve diameter	28 mm	27.1 mm
Exhaust valve diameter	23 mm	23 mm
Intake maximum lift	8 mm	9 mm
Exhaust maximum lift	8 mm	9 mm
Intake valve angle	15°	17.5°
Exhaust valve angle	15°	17.5°
Injector position	Side	Central
Injector angle	27°	6°

the engines the connecting-rod length adopted is the same, since this cannot be changed in the optical test-bench. The piston-pin offset, as well as the cranktrain offset, is zero for constructive reasons of the test-bench, although in the real engine this is not the case. However, both the offset and the connecting rod length have a minor effect on the engine kinematic, and their impact is more relevant from a structural point of view, and can therefore be neglected for the purposes of our work.

Engine 1 was investigated in different working points with different turbulence models and numerical schemes, while Engine 2 was simulated with only one turbulence model, to confirm that the trends observed can be reproduced also for a different geometry. The results obtained will be discussed in the following section.

5.3.1 Results for Engine 1

Engine 1 was investigated at 1500 rpm with 1.6 bar and 1.1 bar average intake pressure, corresponding respectively to 18 bar and 12 bar imep with fired operation. The engine walls were conditioned at ambient temperature (25 °C) and the exhaust system was connected to an extractor fan, thus the back pressure at the exhaust port was assumed to be 50 mbar. The mesh of the engine is presented in fig. 5.2. It is important to notice that the intake boundary is located at the pressure sensor position.

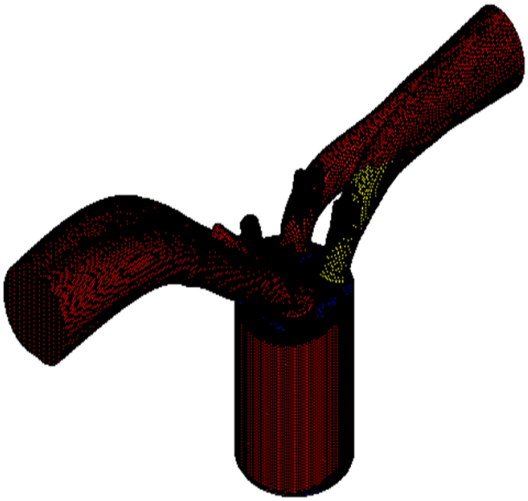

Figure 5.2: Mesh of Engine 1.

In tab. 5.2 the boundaries used for the two operating points are reported.

In fig. 5.3 the experimental and CFD cylinder pressures for both the operating points are reported. Although the simulations were performed with different turbulence and numerical schemes, no differences are visible in the averaged cylinder pressure, thus just a single line for the CFD results is shown

Table 5.2: Boundaries for the two operating points, Engine 1.

	18 bar imep	**12 bar imep**
Engine speed	1500 rpm	1500 rpm
Mean intake pressure	1.6 bar	1.1 bar
Exhaust pressure	1.05 bar	1.05 bar
Int. valve opening (1 mm)	345 °CA	345 °CA
Int. valve closing (1 mm)	543 °CA	543 °CA
Exh. valve opening (1 mm)	168 °CA	168 °CA
Exh. valve closing (1 mm)	365 °CA	365 °CA
Ports temperature	25 °C	25 °C
Cylinder and piston temp.	30 °C	30 °C

on the graphs. It is possible to notice the good agreement between the experimental and the calculated pressure during the intake phase and the first compression phase. The calculated pressure then mismatches the experimental one during the late compression stroke and the expansion stroke, due to the high leakages typical of the optical engine. This is more evident in the p-V logarithmic diagram, presented in fig. 5.4. Since the engine is motored, assuming a perfect adiabatic engine and no leakages, the compression and expansion line would appear overlapping. Since in the CFD model the thermal exchanges are taken into account, the expansion line has a slightly lower slope than the compression one. In the experimental curve the leakages reduce the slope, already during the compression stroke, and the expansion line appears much below the compression one. It is however important to notice that, at least during the initial phase of the compression stroke, when the cylinder pressure is low and the leakages are limited, the CFD pressure has the same slope of the experimental one, allowing to asses the overall quality of the modeling in terms of boundary conditions, fluid properties and engine geometry discretization, which affect the calculated pressure.

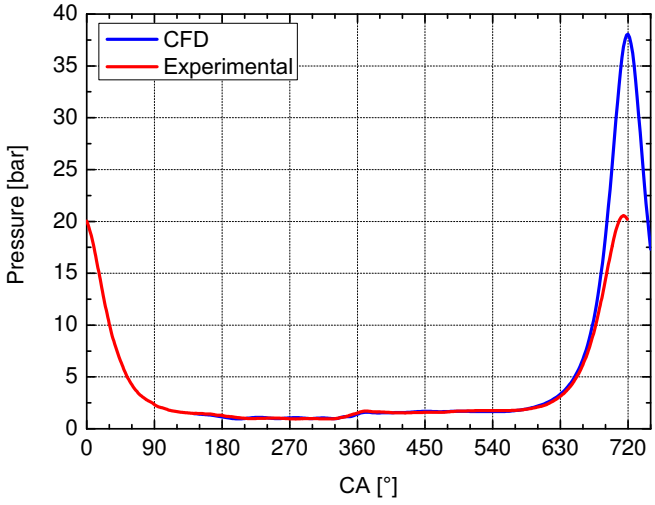

(a)

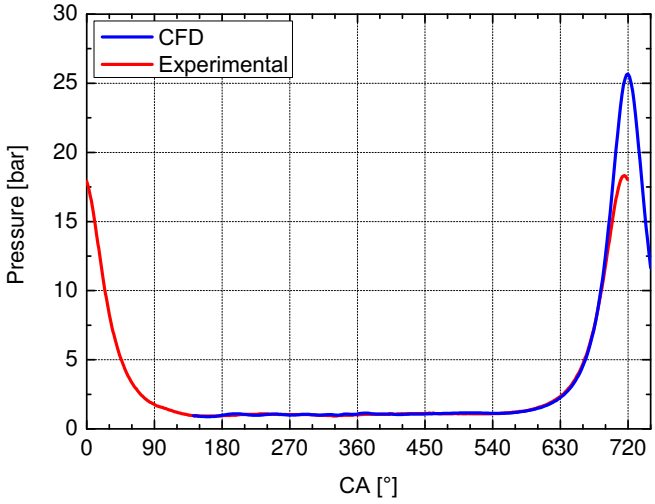

(b)

Figure 5.3: Indicated pressure for 18 bar imep (a) and 12 bar imep (b) operating points.

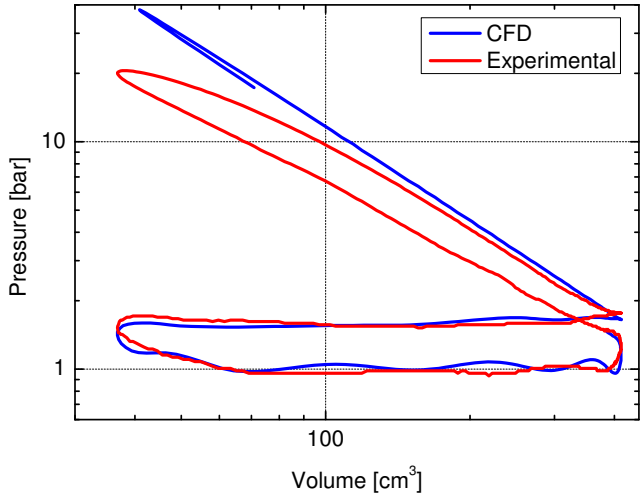

(a)

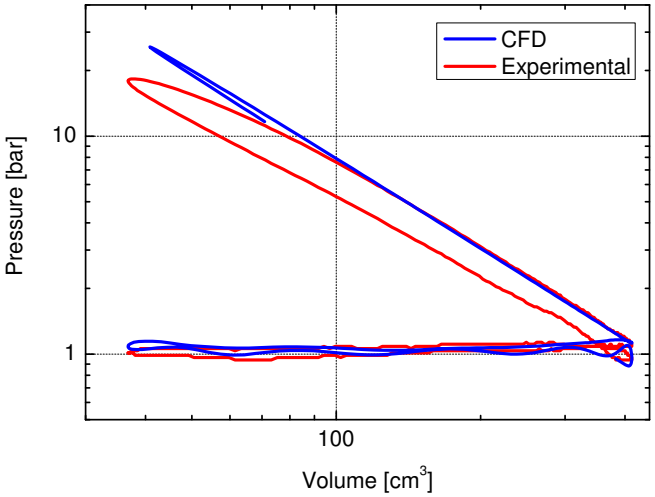

(b)

Figure 5.4: Pressure-Volume bi-logarithm diagram for 18 bar imep (a) and 12 bar imep (b) operating points of Engine 1.

Investigation on turbulence model

Three different turbulence models were investigated, and the results obtained in terms of mean flow and turbulence were compared with PIV measurements. The k-ε RNG variant of the standard k-ε model is nowadays the most used turbulence model for the ICE applications, as it is confirmed from the fact that it is suggested as default model for both Star-CD and Converge software. However, also the standard k-ε model is relatively widespread, thanks to its relatively long existence and its versatility in many different fields and applications. Finally, the k-ω model was investigated, since it is another two-equations model similar to the k-ε, which should be more accurate in the near-wall treatment [16]. All the models were used with their default constants [63].

PIV measurements were performed at the single-cylinder optical test-bench of FEV GmbH, and the results presented consist of images post-processed from an averaging of 30 working cycles.

In fig. 5.5 the motion field in the tumble plane[6] in the cylinder center is presented, at 390 °CA, i.e. at approximately half the maximum lift of the intake valves. At this time, no evident differences between the turbulence models can be observed, although there is overall a slight underestimation of the jet emerging from the intake valves, as far as the PIV measurements are considered.

Observing the results at 454 °CA reported in fig. 5.6 however, the CFD simulations slightly overestimate the velocities near the valves. This is particular evident with the k-ε RNG model and the k-ω, while the standard k-ε model provides the best results.

At BDC, shown in fig. 5.7, all the turbulence models provide almost the same results in terms of average velocity, in good agreement with the PIV measurements. The same trend

[6]The tumble plane is the plane perpendicular to the crankshaft.

is visible also during the compression stroke, as presented in fig. 5.8 at 630 °CA and in the late phase of the compression stroke, reported in fig. 5.9.

From this analysis it appears that the CFD model has some limitations during the intake phase, maybe due to the intrinsic limitations in the RANS approach to solve the boundary layer around the valves. It should be otherwise pointed out that in case of high gradients and high velocities, also the algorithm used in the PIV measurements to determine the velocity components from the raw images can be affected by some errors, since it is not always possible to univocally identify the particles and their movement between two consecutive images. However, when the valves are closed, the in-cylinder motion is correctly reproduced, independently from the turbulence model adopted. In particular, it is possible to correctly reproduce the velocity field and the tumble center movement, which is particular important since the tumble generation is often an aim of the port and combustion chamber design. The tumble motion is in fact converted into turbulence at the end of the compression stroke, enhancing the combustion.

As far as the turbulence is concerned, results are reported from fig. 5.10 to fig. 5.14. It is important to notice that the PIV measurements operate on a plane. For this reason, the velocity component normal to the plane is not taken into account. Although this component is generally small, in order to have perfectly comparable pictures, it was completely canceled in the velocity figures discussed previously. Similarly, also the turbulent fluctuations are calculated using only two velocity components. Assuming an isotropic turbulence, the CFD results were thus scaled with a factor 2/3 to compare them properly with the PIV measurement. Furthermore, the average value of turbulence presented in the graphs, was obtained performing a mass average only on the plane corresponding to the experimental measures, and limiting the average area to that

visible in the experiments, highlighted with the red box in the figures.

As already observed for the velocities, at 390 °CA, reported in fig. 5.10), there is a slightly underestimation of the turbulence level, while at 454 °CA (fig. 5.11) there is a slight overestimation. This is particularly evident with the standard k-ε and k-ε RNG models, while the k-ω provides a lower level of turbulence. However, observing the results at BDC (fig. 5.12), it can be evinced that the k-ω model underestimates the turbulence level, while the standard k-ε and k-ε RNG provide the correct trend and turbulence pattern in the cylinder. This is more evident observing the results obtained during the compression stroke.

It is important to notice that, as for the velocity calculation, the turbulence measurement obtained with the PIV technique can be affected by the same errors in case of high velocities and velocities gradients, because the determination of the turbulence implies first the calculation of the mean flow. This can lead to the filtering of the high frequency components of the turbulence, causing an underestimation of the turbulence level. This can explain the results reported in fig. 5.15, where the resolved kinetic energy and turbulent kinetic energy on the analyzed planes are reported. In fact, it seems that the CFD models overestimate both the quantities, especially in case of the k-ε and k-ε RNG models, which however have demonstrated to provide a better flow and turbulence pattern resolution.

In order to have a confirmation of the observed trends, the other working point presented in tab. 5.2 was simulated. The simulation setup, the post-processing and the analysis of the results were performed in analogy with the operating point already described. Also in this case, observing the velocity field at maximum valve lift reported in fig. 5.16, the standard k-ε model shows the better agreement, while the other

models lead to a slight overestimation. As in the previous operating point, both the standard k-ε and the k-ε RNG give a good result during the compression stroke, shown at 630 °CA in fig. 5.17. Similar results are obtained for the turbulence field, shown for the same crankangles respectively in fig. 5.18 and 5.19. The trends in the global resolved kinetic energy and turbulent kinetic energy, observed in fig. 5.15 for the 18 bar imep case, are completely reproduced also in the 12 bar imep operating point, as shown in fig. 5.20.

The analogy of the results between the two different simulations allows to better assess the evaluation of the different turbulence models, and confirms that the standard k-ε model is the most suitable option amongst those investigated.

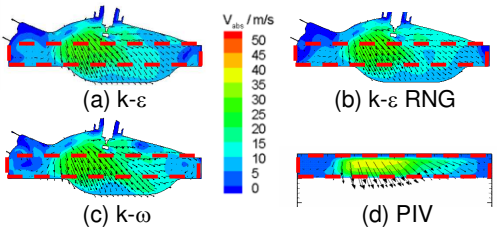

Figure 5.5: Velocity field at 390 °CA, 18 bar imep.

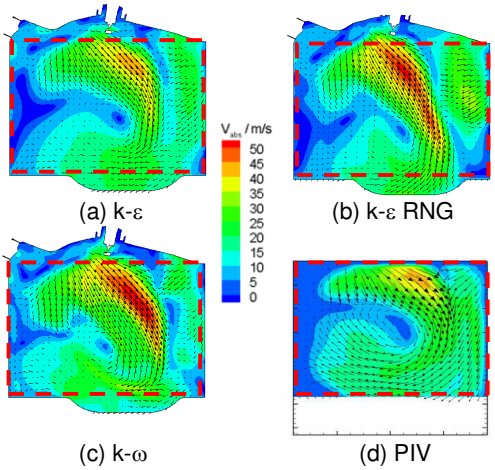

Figure 5.6: Velocity field at 454 °CA, 18 bar imep.

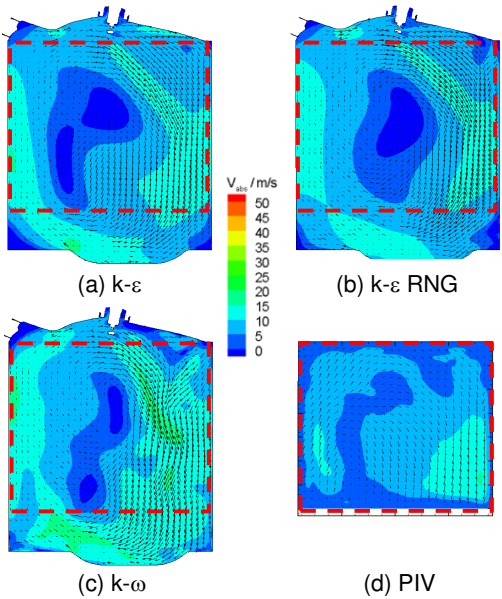

Figure 5.7: Velocity field at 542 °CA, 18 bar imep.

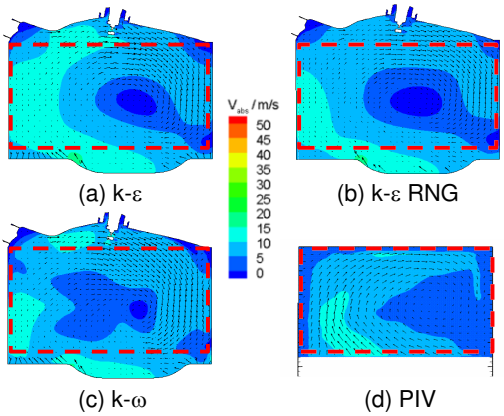

Figure 5.8: Velocity field at 630 °CA, 18 bar imep.

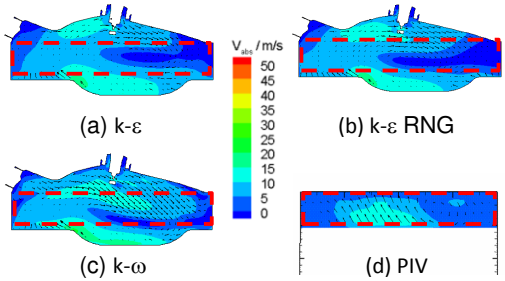

Figure 5.9: Velocity field at 678 °CA, 18 bar imep.

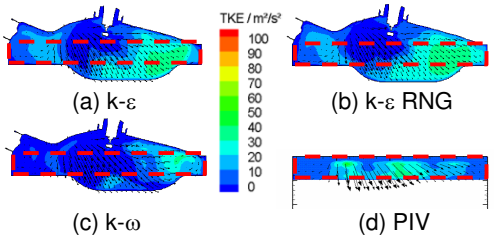

Figure 5.10: Turbulence field at 390 °CA, 18 bar imep.

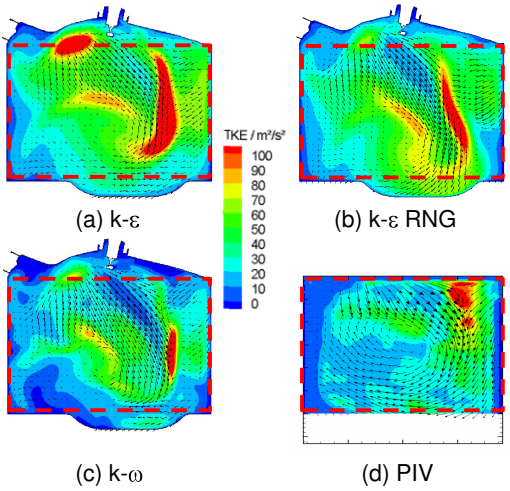

Figure 5.11: Turbulence field at 454 °CA, 18 bar imep.

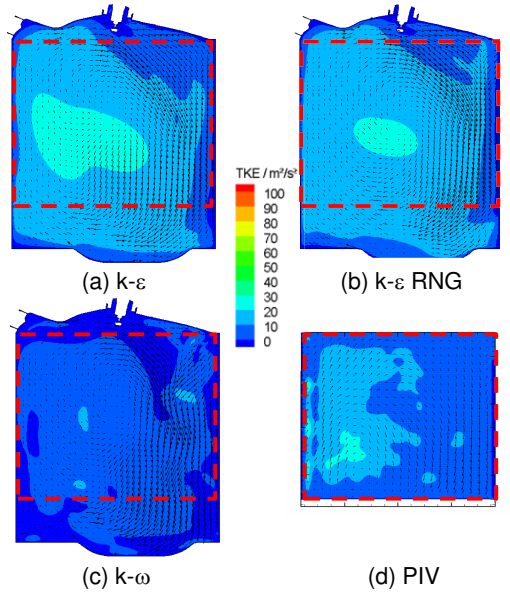

Figure 5.12: Turbulence field at 542 °CA, 18 bar imep.

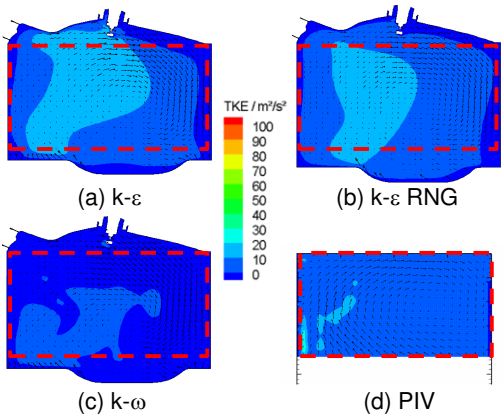

Figure 5.13: Turbulence field at 630 °CA, 18 bar imep.

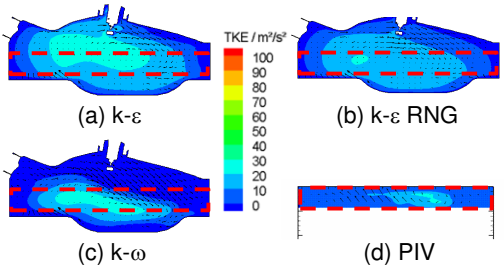

Figure 5.14: Turbulence field at 678 °CA, 18 bar imep.

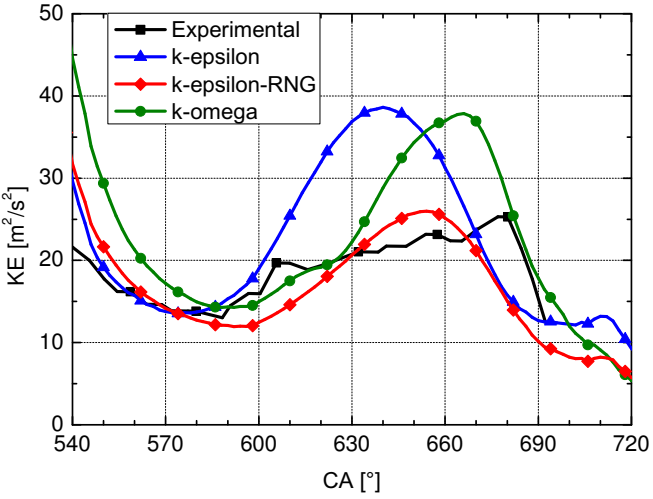

(a)

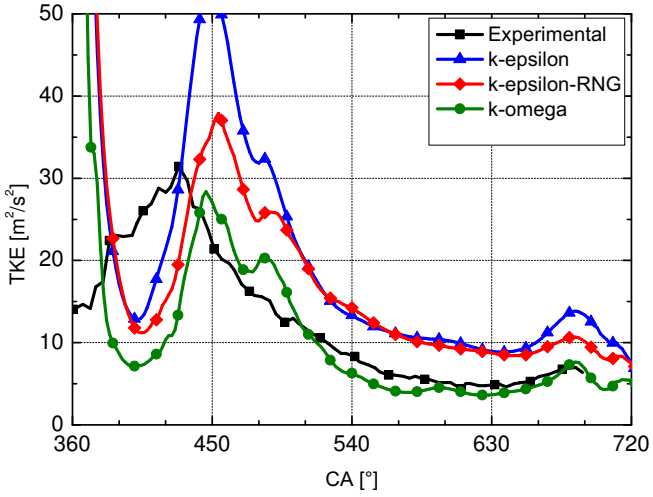

(b)

Figure 5.15: Resolved kinetic energy (a) and turbulence kinetic energy (b) for the operating point with 18 bar imep.

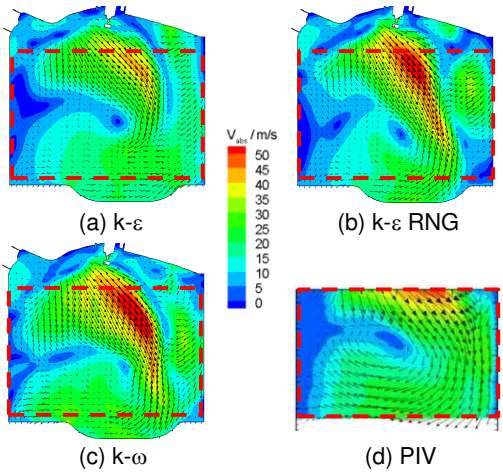

Figure 5.16: Velocity field at 454 °CA, 12 bar imep.

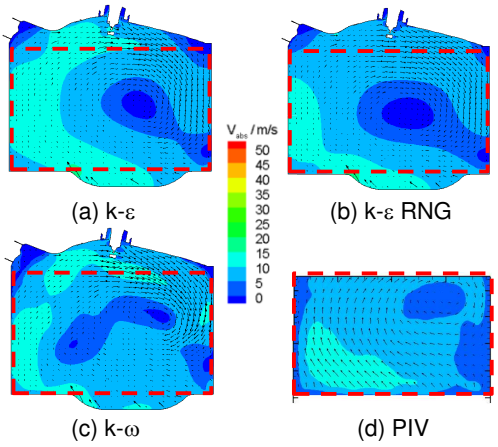

Figure 5.17: Velocity field at 630 °CA, 12 bar imep.

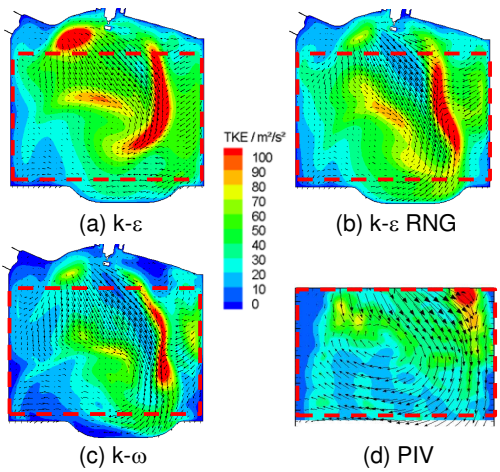

Figure 5.18: Turbulence field at 454 °CA, 12 bar imep.

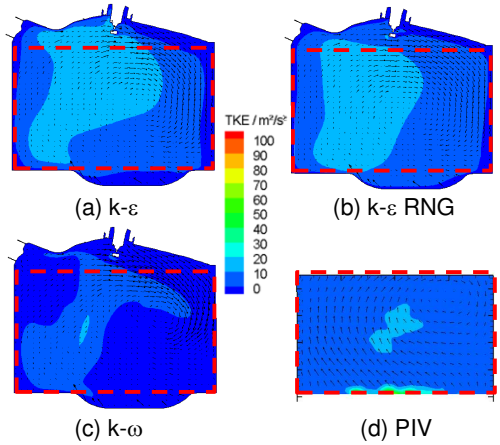

Figure 5.19: Turbulence field at 630 °CA, 12 bar imep.

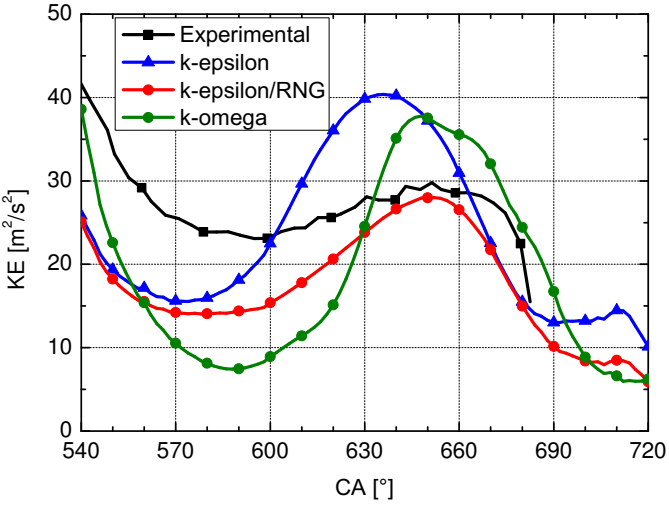

(a)

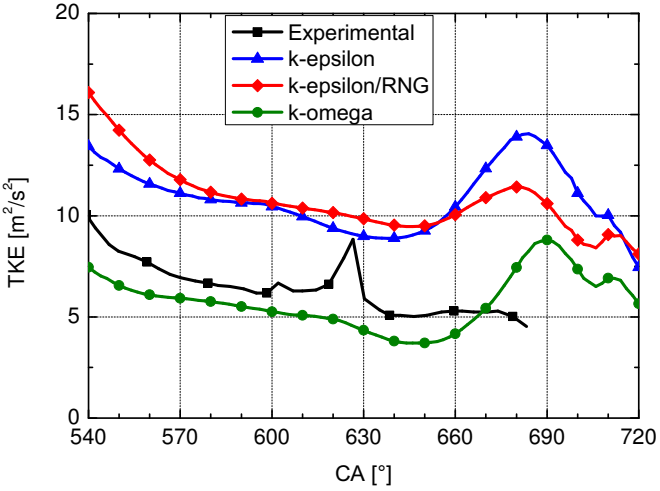

(b)

Figure 5.20: Resolved kinetic energy (a) and turbulence kinetic energy (b) for the operating point with 12 bar imep.

Investigation on the solution method

The results presented in the previous section were obtained using the MARS algorithm for the PDE solution, as explained in section 5.2.3. Also the well known CD algorithm was tested. However it should be pointed out that, for stability reasons, a blending factor of 0.5 was necessary, causing an high numerical dissipation. The results, obtained with the methodology described before, are presented from fig. 5.21 to fig. 5.27. The simulated working point is the one with 18 bar imep reported in tab. 5.2, and the turbulence model adopted is the standard k-ε, which gave the best results in the previous investigation. Thus, results with the MARS solution method correspond to those already presented in the discussion of the different turbulence methods.

The use of the CD scheme instead of MARS has a minor impact on the results, in comparison to the effect caused by the choice of the turbulence model. It can be in fact noticed that the velocity field is almost independent from the choice of the solution schema. The major differences are visible in the turbulence field. Observing the results at 454 °CA in fig. 5.24, which is for the explained reasons the most difficult point to simulate, it can be evinced that the CD scheme introduces a too high dissipation. These effects are visible also during the compression stroke, as can be seen observing fig. 5.25 and 5.26.

Looking at the global values for the resolved kinetic energy and the turbulence kinetic energy, shown in fig. 5.27, it can be observed that, with respect to the experimental data, both the numerical schemes overestimate the fluid velocities and turbulence. Although the CD scheme, thanks to its higher dissipation, is closer to the experimental results, the use of the MARS scheme appears more satisfactory as far as the spatial distribution is concerned. Furthermore, this scheme has proven to be more stable in the current version of the computational code (version 4).

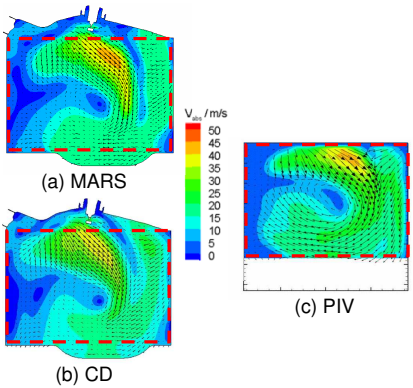

Figure 5.21: Velocity field at 454 °CA, 18 bar imep.

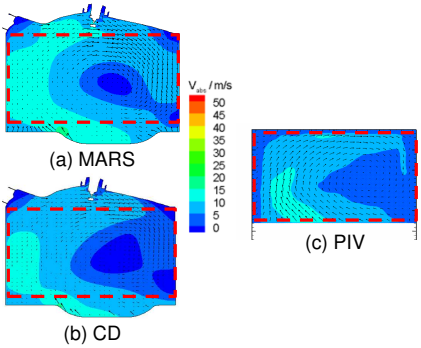

Figure 5.22: Velocity field at 630 °CA, 18 bar imep.

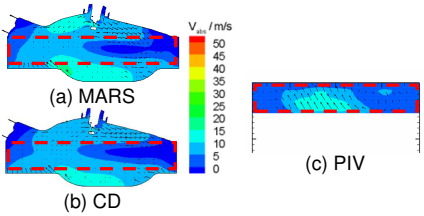

Figure 5.23: Velocity field at 678 °CA, 18 bar imep.

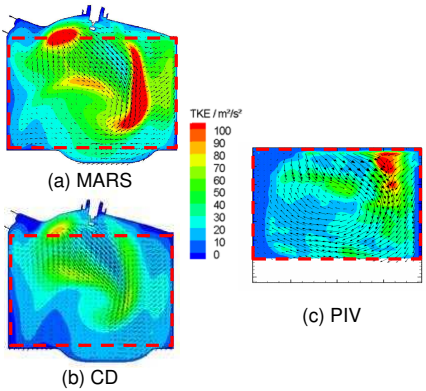

Figure 5.24: Turbulence field at 454 °CA, 18 bar imep.

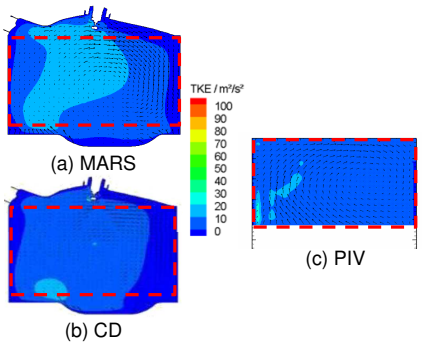

Figure 5.25: Turbulence field at 630 °CA, 18 bar imep.

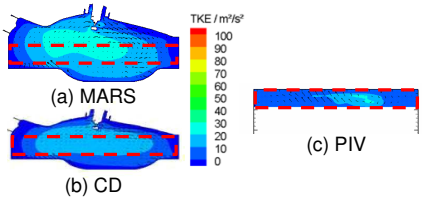

Figure 5.26: Turbulence field at 678 °CA, 18 bar imep.

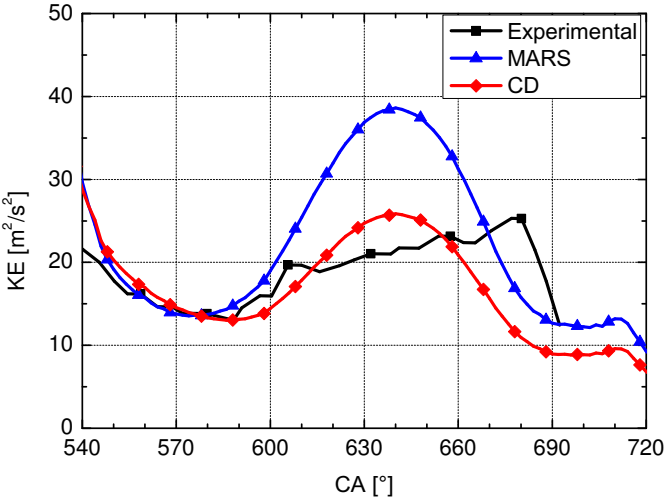

(a)

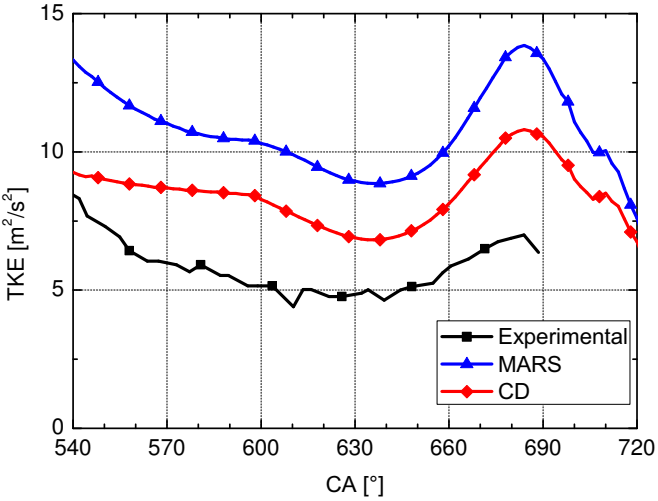

(b)

Figure 5.27: Resolved kinetic energy (a) and turbulence kinetic energy (b) for the operating point with 18 bar imep.

5.3.2 Results for Engine 2

As emerged from the data presented for Engine 1, the most satisfactory results were obtained with the MARS numerical scheme and the standard k-ε model.

In order to confirm the observed trend, a different engine in another operating point was simulated. Engine 2 data are reported in tab. 5.1. As in the previous case the engine speed is 1500 rpm due to the limitation of the optical engine, and the boundary conditions for the investigated point are reported in tab. 5.3.

Table 5.3: Boundaries for the operating point, Engine 2.

	16 bar imep
Engine speed	1500 rpm
Mean intake pressure	1.0 bar
Exhaust pressure	1.2 bar
Int. valve opening (1 mm lift)	350 °CA
Int. valve closing (1 mm lift)	535 °CA
Exh. valve opening (1 mm lift)	184 °CA
Exh. valve closing (1 mm lift)	369 °CA
Ports temperature	25 °C
Cylinder and piston temperature	30 °C

In this case the exhaust system had a different layout, and a back pressure of 200 mbar was assumed at the exhaust port. The mesh of the engine is shown in fig. 5.28.

For this simulation, only the velocity field was compared with the PIV measurements, and the CFD results were post-processed with the same Matlab script used for the PIV results. Analyzing the flow field at 450 °CA, reported in fig. 5.29, a similar behavior to the one obtained for Engine 1 is observed, with a slight overestimation of the jet emerging from the intake valves. However the flow field at BDC can be correctly

reproduced, as well as the flow field and the tumble center motion during the compression stroke.

As already discussed, the flow field at open valves is interesting especially for the injection simulation, which generally takes place during the intake stroke. However the correct flow field resolution during the compression stroke is more important, since the conversion of the tumble motion into turbulence is used to enhance the combustion, and the tumble level is one of the criteria for the evaluation of the intake port and combustion chamber design.

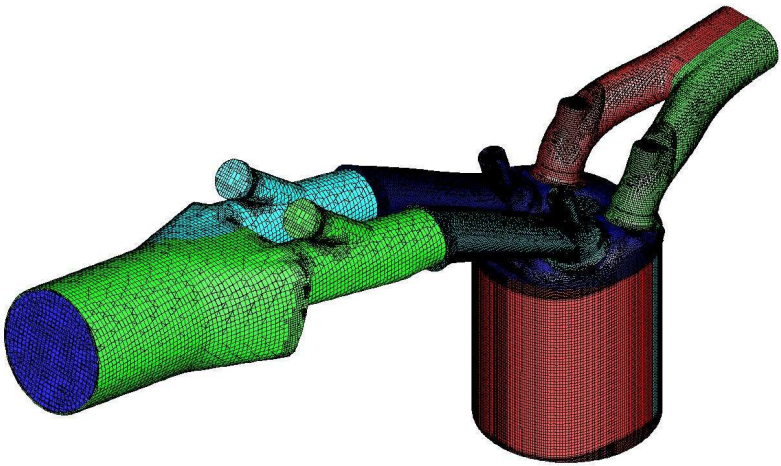

Figure 5.28: Mesh of Engine 2.

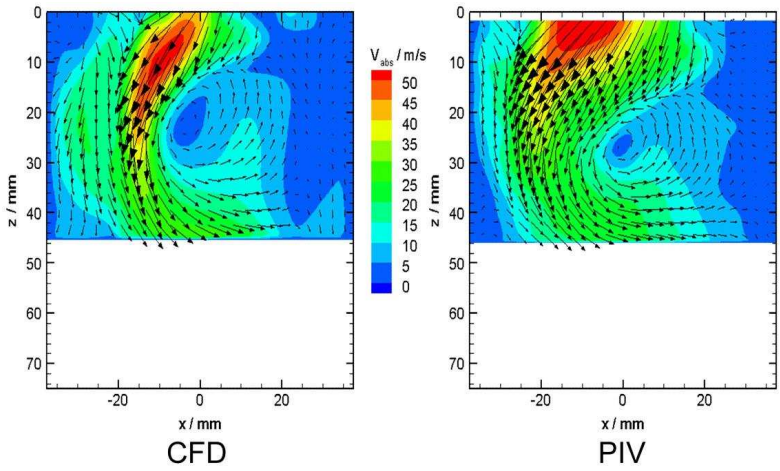

Figure 5.29: Velocity field at 450 °CA, Engine 2.

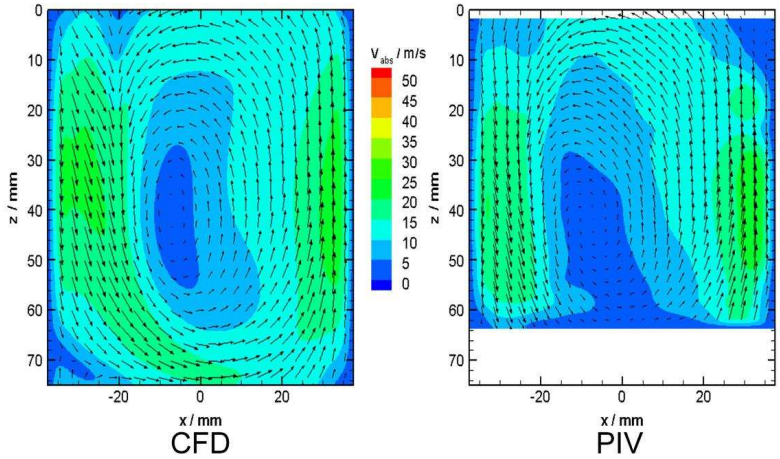

Figure 5.30: Velocity field at 540 °CA, Engine 2.

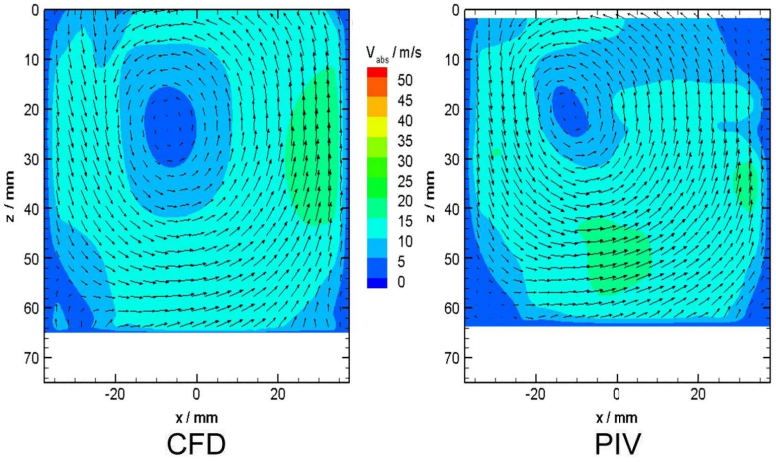

Figure 5.31: Velocity field at 600 °CA, Engine 2.

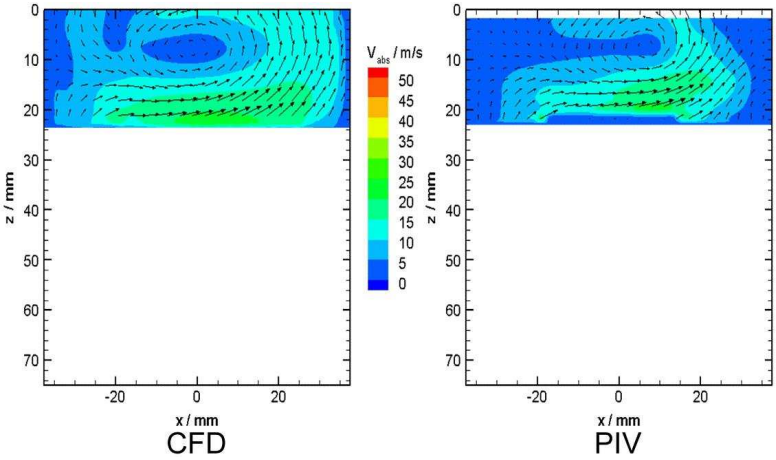

Figure 5.32: Velocity field at 660 °CA, Engine 2.

5.4 Conclusions

In this chapter the main settings adopted for the cold-flow simulations were presented and discussed in detail. Thanks to PIV measurements in different engines and different working points, the choice of the numerical scheme and the turbulence model was analyzed and motivated. Among the investigated models, the standard k-ε model gave the best results, and thus will be used in the next part of this work. Furthermore, the accuracy of the CFD simulations for the cold-flow was assessed. The results obtained showed that some discrepancies during the intake stroke, especially at maximum valve lift, can be expected, while the flow field at BDC and during the compression stroke can be correctly reproduced.

The knowledge gained in the cold-flow simulation will serve as basis for the injection simulations. In fact, the interaction between droplets and air plays an important role in determining the spray shape, spray penetration, evaporation and mixture formation, but due to the high number and complication of the phenomena involved, it is not possible to identify the effect of each submodel adopted. For this reason, a good prediction of the air motion helps in the analysis of the other phenomena involving the spray breakup and evaporation.

Chapter 6

Injection simulations

In this chapter, the procedures developed and used to perform the injection simulations will be described and analyzed in detail.

In modern GDI engines, injection process plays a crucial role in determining the engine performances, intended not only as engine power, but also in terms of pollutant emissions and fuel consumption. The simulation of the injection process is still nowadays challenging, because many complex and not completely understood phenomena are involved.

In particular, the atomization process of the spray emerging from the nozzle is still under investigation in its fundamental mechanisms, briefly recalled in the chapter 4. The volatile behavior of the gasoline, characterized by a continuous distillation curve due to its large variety of hydrocarbon compounds, presents a further challenge in the numerical simulations. Finally, in the wall film formation process, there is a lack of reliable and calibrated models for gasoline engines, due to intrinsic limitations in its experimental investigation. This phenomenon is however strictly related to the oil dilution and soot formation, of high importance in GDI engines, therefore it must be taken into account.

In line with the aim of this work, the focus during the research phase was on the development of a CFD model capable to address the questions emerging during the engine concept phase, as for example the choice of the injector targeting or positioning, or its actuation strategy. Although this obviously requires to deal with the physics involved in the phenomena, during this work an attempt was made to keep the models as simple as possible, to be capable to use them with a reduced amount of input, and in a short simulation time.

As for the cold-flow simulations, a great effort was made to compare always the proposed models with the experimental data, in order to assess the reliability of the procedure and to evidence its possible limitations.

6.1 Injection model

The wide variety of the GDI engines nowadays on the market and under development adopt a multi-hole injector, with injection pressure up to 200 bar. Some engines equipped with an outwards opening injectors are present as well on the market, thanks to the advantages brought especially for the spray-guided narrow spacing combustion concept [65, 66]. Nevertheless, this work focuses mainly on the modeling of multi-hole injectors, which are currently the most adopted solution.

A coupled Lagrangian-Eulerian approach was used for the spray simulation. Each parcel, accounting for a certain number of droplets, is introduced in the computational domain with a defined diameter and velocity. The parcels are then followed using a Lagrangian approach, and source terms in the conservation equation are introduced, to take into account the exchange of momentum, energy and mass with the background fluid, for which the Eulerian approach is used [21].

This approach has the advantage not to require a detailed modeling of the flow inside the nozzle, allowing a limited in-

crease of the simulation time in comparison with a cold-flow simulation. Furthermore, only the nozzle main geometrical characteristics (in the simplest approach only the hole diameters and the injector targeting) are required to perform the simulation, allowing to use the simulation from the first phases of the engine development. Some drawbacks can be found in the limitation in correctly modeling the narrow field near the injector. It is in fact necessary to introduce the liquid fuel in the computational domain already in form of droplets, whose diameter has to be determined with an ad hoc model. In this way, it is avoided to reproduce the stripping process from the liquid core, or the cavitation and break-up phenomena in the nozzle, which are substituted with some ad hoc assumptions.

The model used in this work tries however to go beyond the limitation derived from the absence of the liquid core. In case the droplet are introduced at the nozzle tip, they are immediately subjected to the exchange of momentum with the surrounding air. With this approach, in order to avoid underestimation of the fuel penetration while keeping the correct droplet size, a tuning in the drag coefficient is often required [67]. Introducing the droplet along the liquid core, on the contrary, it is possible to relate the linear penetration phase of the spray directly to the liquid core growth, which is determined in dependence from the spray velocity at the nozzle exit. Furthermore this has the effect that the droplets are distributed along the liquid core length, instead of being placed only in the cells near the nozzle exit. Therefore, the underlying assumption of the Lagrangian approach – that the liquid phase is enough dispersed in the gaseous phase – can be more easily fulfilled. Finally, it was observed that with this approach the simulation has less convergence problems, and the results are less dependent from the spatial discretization in proximity of the nozzle exit.

The stable liquid core length is calculated according to

the model proposed by Hiroyasu [68]. The liquid core length $L_{core|t\to\infty}$ is defined as:

$$L_{core|t\to\infty} = f_{hiro} d \left(1 + 0.4\frac{r}{d}\right) \left(\frac{p_g}{\rho_l U_0^2}\right)^{0.05} \left(\frac{l}{d}\right) \sqrt{\frac{\rho_l}{\rho_g}} \quad (6.1)$$

where d is the the injector hole diameter, r is its rounding radius and l the orifice length, p_g is the air pressure, ρ_l and ρ_g are respectively the liquid and air density, and U_0 is the droplet velocity at the hole exit. f_{hiro} is a constant that can be used to calibrate the model: Hiroyasu suggests in its work, based on diesel spray, a value of 7.0. In the present work however, a dependency of this parameter from the chamber back pressure was encountered, and for this reason the parameter was changed during the model calibration in order to obtain a better fit of the experimental data.

The mean velocity u_{mean} in the injector nozzle is calculated as:

$$u_{mean} = \frac{\dot{m}_{inj}}{A_{hole}\rho_l} \quad (6.2)$$

where $\dot{m}_{inj}$ is the instantaneous mass flow through the hole and A_{hole} is the geometrical area at the nozzle exit. In order to take into account the cavitation effect, the Nurick's law [69] is used to calculate the area of the vena contracta. This area is used to calculate the velocity in the vena contracta, as:

$$u_{vena} = \frac{u_{mean}}{C_c} \quad (6.3)$$

where C_c is the contraction coefficient from the Nurick's law, obtained as [69]:

$$\left(2.687 - 11.4\frac{r}{d}\right)^{-0.5} \quad (6.4)$$

Obtained this velocity, and assuming an isentropic flow in the injector nozzle, the velocity at the injector exit U_0 can be

finally calculated as:

$$U_0 = u_{vena} - \frac{p_2 - p_v}{\rho_l u_{mean}} \tag{6.5}$$

where p_2 is the pressure at the injector exit, and p_v is the pressure in the vena contracta, determined as:

$$p_v = p_1 - \frac{\rho_l}{2} u_{vena}^2 \tag{6.6}$$

where p_1 is the injection pressure.

To simulate the liquid core, the droplets are introduced in the computational domain along the liquid core length determined by eq. (6.1). Their size d_{prim} is determined, following the Schneider approach [70], according to the position x they assume in the liquid core, with the equation:

$$d_{prim}(x) = \sqrt{52.34 \frac{\sigma}{\rho_g u_{rel}(x) \frac{\mathrm{d}u(x)}{\mathrm{d}y}}} \tag{6.7}$$

where σ is the surface tension, $u_{rel}(x)$ is the relative velocity between the gas phase and the liquid core, and $\mathrm{d}u(x)/\mathrm{d}y$ is the radial velocity gradient. $u_{rel}(x)$ is determined as:

$$u_{rel}(x) = \frac{U_0}{2} \left(1 - \frac{3}{4} \frac{x}{L_{core}} \right) \tag{6.8}$$

and the radial velocity gradient is obtained as:

$$\frac{\mathrm{d}u(x)}{\mathrm{d}y} = C_{dudy} \frac{u_{rel}(x)}{0.6d - 0.5d_s(x)} \tag{6.9}$$

where C_{dudy} is a calibration coefficient and $d_s(x)$ is given by:

$$d_s(x) = d \left(1 - \frac{x}{L_{core}} \right) \tag{6.10}$$

Finally, the jet opening angle α is determined according to Naber and Sieber [71] as:

$$\alpha = 2 \arctan \left[C_{Naber} \left(\frac{\rho_g}{\rho_l} \right)^{0.19} \right] \tag{6.11}$$

Once the droplets are introduced in the computational domain, they interact with the background fluid exchanging mass, momentum and energy, and are managed directly by the CFD code. Droplets can incur in the secondary break-up, for which the Reitz and Diwakar model [72] was chosen, already available in the CFD code. According to this model, droplets break-up due to the aerodynamic forces can be caused by the "bag break-up", by effect of non-uniform pressure field that causes drop deformations, or the "stripping break-up", where the liquid is stripped from the droplet surface. For each criterion a stable droplet diameter d_{stable} and a break-up time constant τ_b can be determined, and the droplet size d_d is then reduced until the stable diameter is reached. The stable droplet diameter in case of bag break-up is the diameter of the droplet that allows to satisfy the following equation, based on the Weber number We:

$$We \triangleq \frac{\rho |\vec{u} - \vec{u}_d|^2 d_d}{2\sigma_l} \geq C_{b1} \tag{6.12}$$

where $\vec{u}$ is the fluid velocity, $\vec{u}_d$ is the droplet velocity, and C_{b1} is a model constant whose default value is 6.0. The associated characteristic time τ_b is:

$$\tau_b = \frac{\pi \rho_l^{0.5} d_d^{1.5}}{4\sigma_l^{0.5}} \tag{6.13}$$

In case of the stripping break-up, the criterion for the onset of this regime is:

$$\frac{We}{\sqrt{Re_d}} \geq C_{s1} \tag{6.14}$$

where C_{s1} is a model constant whose default value is 0.5, and Re_d is the droplet Reynold number, determined as:

$$Re_d \triangleq \frac{\rho|\vec{u} - \vec{u}_d|d_d}{\mu} \tag{6.15}$$

In this case, the characteristic break-up time is determined as:

$$\tau_b = \frac{C_{s2}}{2}\left(\frac{\rho_l}{\rho_a}\right)^{0.5}\frac{d_d}{|\vec{u} - \vec{u}_d|} \tag{6.16}$$

where C_{s2} is an empirical coefficient whose default value is 20.

The droplet diameter variation over the time t can be then determined as:

$$\frac{\mathrm{d}d_d}{\mathrm{d}t} = \frac{d_d - d_{stable}}{\tau_b} \tag{6.17}$$

It is noteworthy to point out that, in addiction to the already mentioned advantages in the simulation stability, the use of a liquid core model allows to better reproduce the physical structure of the spray [73, 42], going beyond the intrinsic limitation of the Lagrangian-Eulerian approach, which does not allow to reproduce the continuous liquid part of the spray.

It is known in literature that the classical approach used in engine applications, consisting in modeling just the flow outside the nozzle, can lead to incorrect results. Simulation of the internal flow inside the injector is required to better predict the primary break-up [74]. However, this requires a detailed knowledge of the nozzle geometry, that is generally not disclosed by the injector supplier. For this reason, since the present work focuses on the application of CFD methodologies for GDI-engine simulations mainly from an OEM or engine developer point of view, the proposed method was preferred. In this way, an attempt was made to provide a physical description of the spray, without requiring neither an increment of the input data nor an higher computational cost. This obviously limits the predictive capabilities of the model, but the calibration performed and here presented proves that the model is

capable to well simulate the spray shape and penetration in different working conditions. The calibration consists in tuning only few parameters, and therefore the model was judged more than adequate for the purposes of this work.

The effects of the use of the liquid core are presented in fig. 6.1, where the results obtained using the presented model with and without liquid core are compared with experimental images, obtained for a Bosch 6 holes injector at 1 bar backpressure and 150 bar injection pressure. The two comparing simulations were run after the calibration of the model with the liquid core, in order to obtain the correct spray penetration and average droplet size[1]. The simulation without liquid core was then performed using the same model parameters, except the Hiroyasu parameter, changed in order to limit the liquid core length at 1 mm.

As can be evinced from the images, the use of the liquid core allows to better predict the spray shape and the spray penetration, shown in the graph of fig. 6.2. The droplets size is almost identical in both the simulations, and corresponds to what was experimentally measured with laser diffraction technique. However, without using the liquid core, it is not possible to match the experimental penetration, unless tuning the model with different parameters to modify the droplet size, that would then not match with the experimental measurement.

[1]In this case the average droplet size at 30 mm from the injector tip was provided.

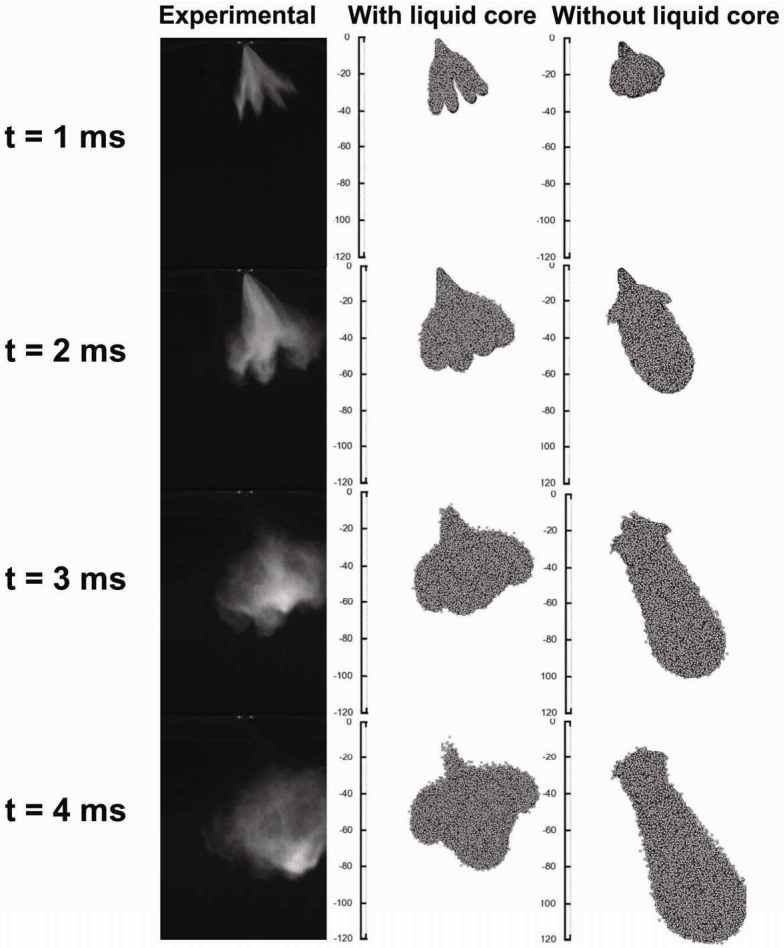

Figure 6.1: Effect of the liquid core on the spray shape.

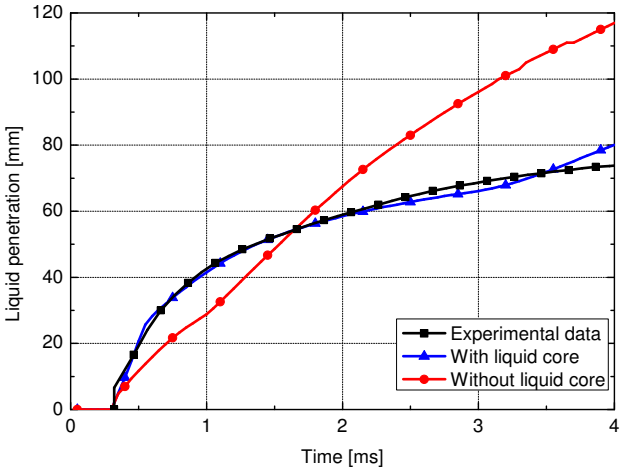

Figure 6.2: Spray penetration with and without liquid core.

6.2 Fuel model

In order to better reproduce the volatile behavior of gasoline, a bi-component mixture was defined, which consists of 53% in mass of 2-methylpentane (C_6H_{14}), representing the lighter components of the gasoline, and 47% of *normal*-octane (C_8H_{18}), used to represent the heavier components of the fuel. By using a bi-component approach, it is possible to better approximate the distillation curve of the gasoline in comparison with a mono-component fuel such as *n*-heptane or *n*-octane, as shown in fig. 6.3. This approach improves the quality of the mixture formation prediction and, in case a wall-film model is used, of the droplet-wall interaction.

From the implementation point of view, the use of a bi-component fuel corresponds to the definition of two different fluids whose each droplet is composed, and two different scalars[2] in which the evaporated fraction of each component

[2] A scalar is here considered as a tracer. It can be defined as "passive",

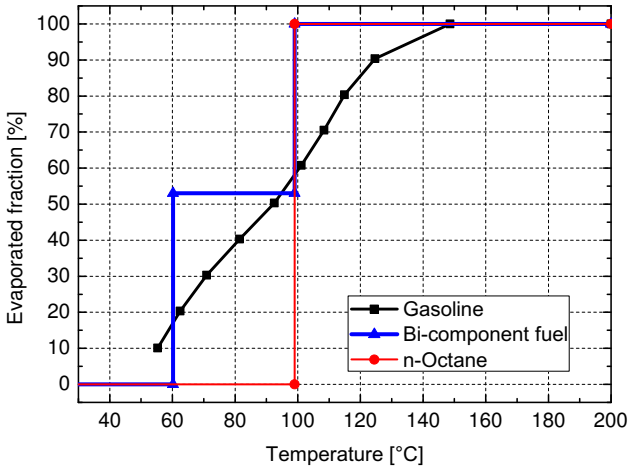

Figure 6.3: Distillation curves at 1 bar pressure of gasoline [75], n-octane and bi-component fuel as in the CFD model.

is considered. In case a liquid film model is used, also two components for the liquid film have to be specified.

It is important to notice that the use of such a bi-component fuel has a deep impact on the spray shape predicted from the model in evaporative conditions, while it has obviously a minor impact in case of lower fuel and chamber temperatures, as those typical of motored optical engine operations. In order to show the impact of the bi-component fuel model on the spray shape and penetration, two simulations with mono-component and bi-component fuels were carried out, in non-evaporative conditions (fuel temperature 20 °C, air temperature 20 °C) and in evaporative conditions (fuel temperature 50 °C, air temperature 100 °C) in a quiescent chamber at atmospheric pressure (1 bar). Results are reported in fig. 6.4a

if it does not influence the background fluid composition, or "active", when its properties are taken into account to determine the fluid global characteristics. In this case the scalar are defined as active.

and 6.4b respectively. As shown in fig. 6.4a, the spray shape in non-evaporative conditions is almost identical between the two fuel models, although the evaporated mass is slightly changed. However, in evaporative conditions the spray shape is modified due to a different evaporation rate, especially at the spray periphery, where heat exchange with the surrounding air is more intense.

In fig. 6.4 the color scale ranges from yellow to red, and it is proportional to the fuel liquid mass integrated along the line parallel to the view direction. In this way a spray visualization of the CFD results can be obtained, which is more easily comparable with the Mie-scattering experimental images, as explained in the next section.

6.3 Wall impingement treatment

Wall impingement is one of the crucial thematics for the GDI engines development, since it is well established that it can lead to soot formation [6]. In fact, due to the late evaporation of fuel, and consequently rich zones in the fuel mixture, diffusive flames can occur, causing particulate formation. Furthermore, fuel impinging on the liner leads to oil dilution, which accelerates the oil degradation, forcing to shortened oil substitution intervals. For these reasons, injection timing and injector targeting have to be carefully defined to optimize the fuel mixture, without causing an excessive wall impingement on the cylinder liner, piston ceiling and intake valves.

The available experimental data on the wall film formation in GDI engines are however limited, due to the intrinsic difficulties in measuring the wall film thickness in real operating conditions. Currently, the most diffused model for the interaction of the droplets with the wall in engine applications is the Bai-Gossman model [76]. This model is available in the computational code used for this work, and was therefore used

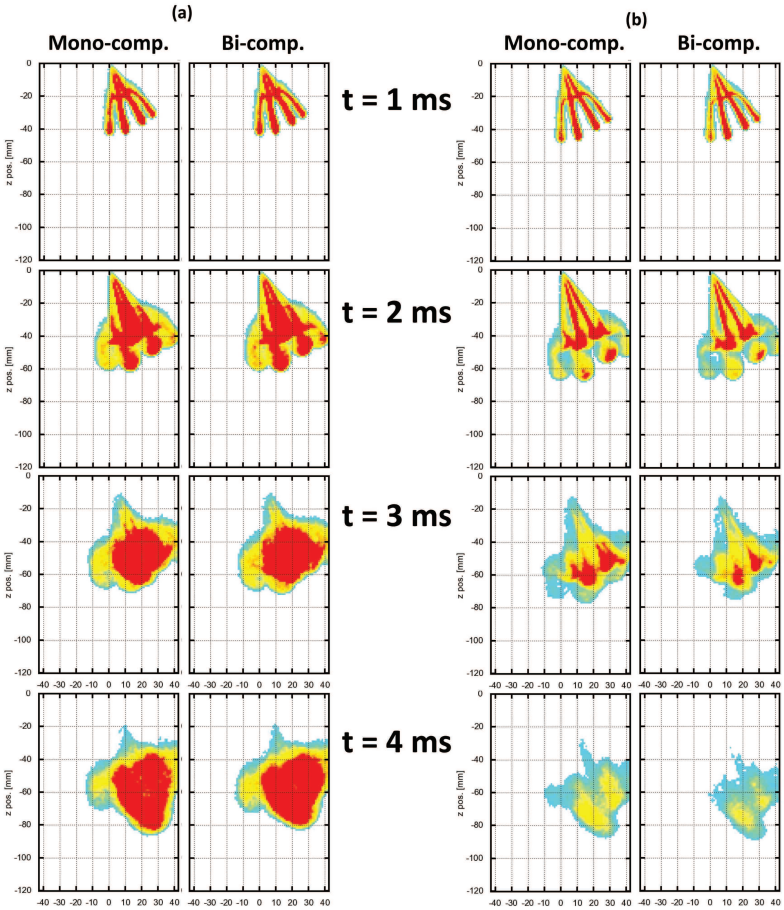

Figure 6.4: Spray shape with mono- and bi-component fuel in non-evaporative (a) and evaporative (b) conditions.

in the simulation that will be presented.

The model distinguishes between five different behaviors that a droplet can have when it encounters a wall:

- rebound: the impinging droplet bounces off the wall with an elastic collision;
- splash: the impinging droplet breaks up into smaller droplets, and some of them are subjected to rebound, while others undergo in the sticking or spreading;
- break-up: the impinging droplet breaks up into smaller droplets, and all the smaller droplets bounce off the wall;
- stick: the impinging droplet adheres to the wall in nearly spherical form;
- spread: the droplet adheres to the wall, but it is spread along the wall surface creating a wall film or merging with the already existing wall film.

The transition between the different criteria is mainly dependent from the wall temperature, the droplet temperature, the droplet velocity relative to the wall and incidence angle, and the droplet Weber number. Details on the transition criteria and the implementation in Star-CD can be found in the Star-CD methodology manual [21], and they are here omitted for the sake of brevity.

The wall-film modeling is currently available in the version of the CFD-code used, but its validation cannot be performed due to the lack of experimental data. In order to avoid the effects of some uncertainty in the model, in this work it was chosen not to use the wall film. Obviously in this case, the behavior "spread" of the Bai-Gossman model cannot take place. However, an alternative procedure to evaluate the wall wetting, and thus the risk of oil dilution and soot formation, is discussed in cap. 7.

6.4 Results for Engine 1

In this section the results obtained for the injection simulation of the operating point at 18 bar imep of tab. 5.2 are presented. The experimental setup for the light scattering investigation used in this comparison was almost identical to the one used in the PIV measurements, except the laser pulses that were adjusted to equidistant timings. The camera was operated with 2 °CA increments, and it recorded the scattered light from the fuel droplets in a vertical light sheet. The light sheet orientation was identical to the PIV set-up, in the tumble plane. Standard gasoline fuel was used for the Mie-scattering analysis. The crankangle resolved spray visualization was evaluated by automated image processing routines, based on Matlab image processing library.

6.4.1 Model calibration

The model was calibrated for a Bosch 6-hole solenoidal injector with a static mass flow of 7.3 g/s at 100 bar injection pressure. The injector was measured using shawdography imaging and laser diffraction techniques for droplets sizing, in a quiescent chamber with adjustable air pressure. Fuel and air temperature were kept constant at 20 °C.

Data for the calibration were registered with a backpressure of 1.88 bar, which well approximate the in-cylinder pressure at the start of injection (SOI), during the intake stroke.

The quiescent chamber was reproduced in the CFD-simulations with a cubic volume with a cell size between 1.0 and 2.0 mm, which corresponds approximately to the cell size adopted also for the in-cylinder simulations.

Usually, CFD results are represented as a series of images where the droplets can be colored according to their temperature, size, mass or density, and can be scaled with their diameter. However, this kind of images are difficult to be com-

pared with the Mie-scattering experimental images. In fact, the intensity of the scattered light in the Mie-measurement is proportional to the scattering cross section, hence the square of the droplet diameter. The registered intensity can be thus correlated, assuming a constant density for the spray, to the mass of liquid illuminated by the laser in that position, hence giving an indication of the amount of liquid spray which is present in a certain location.

In order to obtain a more comparable representation, some of the CFD results presented in this chapter were post-processed integrating, at each time and for each location, the amount of mass which is present in the line perpendicular to the representation plane passing through the corresponding location of the picture. The colored scale is proportional to the cumulative mass along that line, scaled with a factor to obtain an intensity of the colors similar to those visible in the experimental images. Although also these images are not directly comparable with those obtained with the Mie-scattering, their meaning is more similar to the experimental results than just the representation of the single droplets obtained from CFD simulations.

In tab. 6.1 the injector characteristics and the boundary conditions adopted for the injector calibration are summarized. In fig. 6.5 the mass flow rate imposed in the simulation is reported. Since the static flow of the injector is 7.3 g/s at 100 bar, the mass flow was scaled with Bernoulli's law to obtain the mass flow at the injection pressure. Since no measurements of the instantaneous mass flow were available, a dummy mass flow rate was constructed, using for the opening delay, as well as the opening and closing ramp duration, the data provided from the injector supplier, with an iterative process of slight modifications to better match the measurements. The same mass flow used for the calibration, except a change in the injection duration, was then used for the in-cylinder simulations.

Table 6.1: Injector characteristics and calibration boundary conditions for injector 1.

Number of holes	6
Hole diameter	165 μm
Injection pressure	150 bar
Chamber back pressure	1.88 bar
Gas temperature	20 °C
Fuel temperature	20 °C

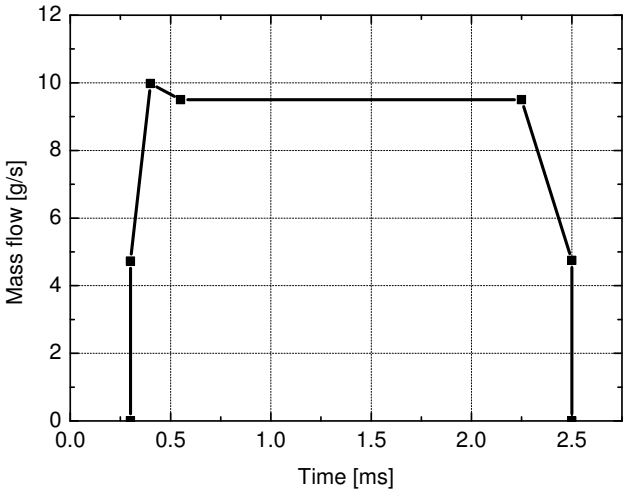

Figure 6.5: Mass flow rate for Engine 1 calibration.

In fig. 6.6 the spray penetration obtained in the CFD simulation and the experimental measurement are reported. It is possible to observe that the 99% penetration curve matches well with the experimental measurements. The graph reports also the length of the liquid core used in the model. It is interesting to observe that the liquid core, according to the model, grows linearly until the steady length is reached. This al-

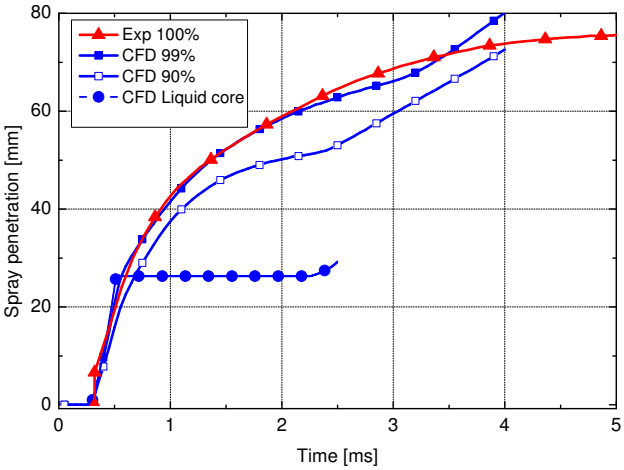

Figure 6.6: Spray penetration for the model calibration of the 6-hole injector.

lows to better reproduce the linear penetration phase without cheating on the droplet size, as explained in the section 6.1.

A further confirmation of the model validity can be obtained comparing the experimental images with the calculated ones. As shown in fig. 6.7, the model is capable to correctly reproduce the spray shape in both the planes of measurement.

6.4.2 In-cylinder results

After the calibration described in the previous section, the injection model was used to perform the in-cylinder simulation of the working point at 18 bar imep reported in table 5.2. Differently from the data in table 5.2, the cylinder head was in this experimental measurement conditioned at 70 °C as well as the injected fuel (commercial gasoline RON 95). The glass piston was not conditioned, but infrared measurements showed a temperature of 50 °C. The same temperatures were imposed in the CFD boundaries.

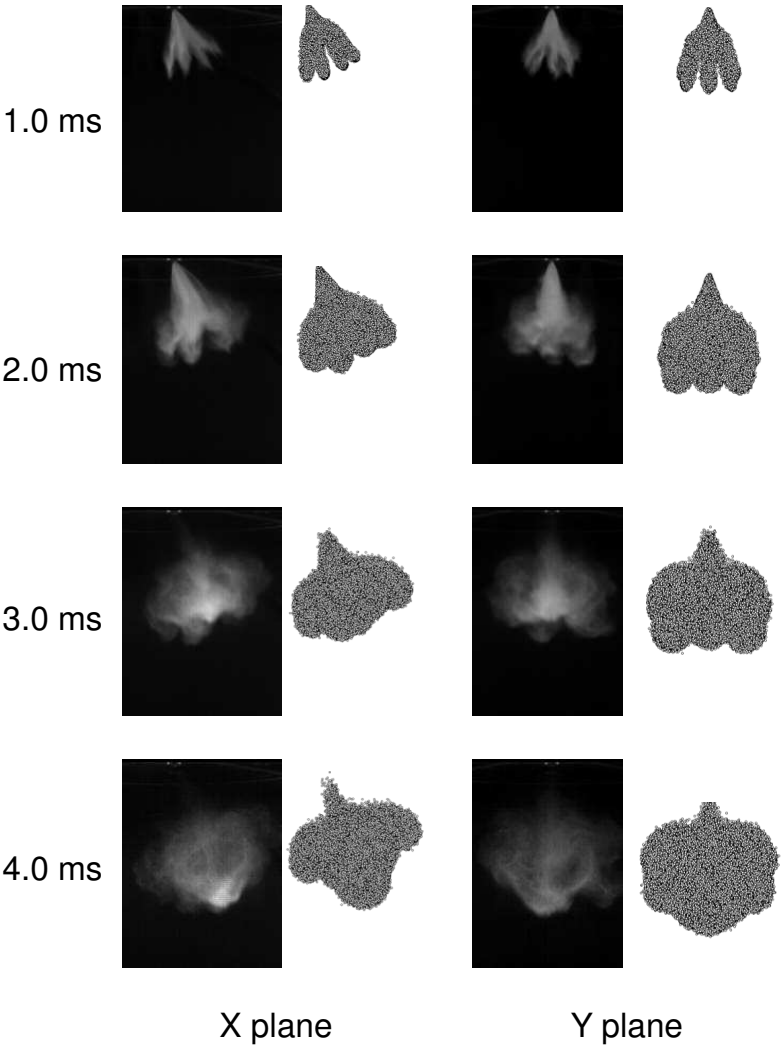

Figure 6.7: Spray images for the model calibration of the 6-hole injector.

The engine mesh used was the same presented for the cold-flow simulation of this engine, as well as the location of the boundary conditions.

Since the air mass flow was measured through an air debimeter, but no measurement of the temperature in-cylinder was available, the simulation was started before the exhaust valve opening, at the end of the expansion stroke, in order to deduce the initialization temperature from the trapped mass and the measured pressure.

The total injected mass was 54.7 mg, corresponding to a duration of injection (DOI) of approximately 55 °CA. The mass flow rate was defined considering the same opening delay, opening ramp duration and closing ramp duration as for the calibration case, converting the delay in ms to take into account an engine speed of 1500 rpm. The resulting mass flow rate is presented in fig. 6.8.

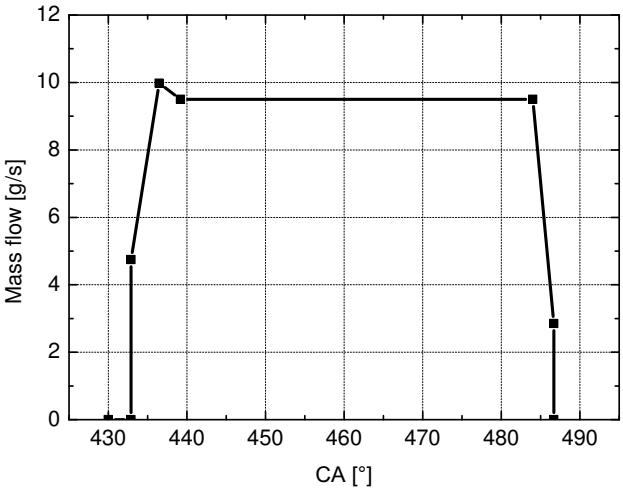

Figure 6.8: Mass flow rate for Engine 1 simulation with SOI 430 °CA.

In this case, Mie-scattering images of the spray were available, and were compared with the CFD images post-processed as previously described. Two measurements plane were investigated, one being the central tumble plane, and the other parallel to this one, but on the valve section. The approximate width of the laser sheet used in the Mie-measurements was 2 mm. To obtain more comparable images, the mass in a width of 7 mm for each side from the measurement plane position was integrated in the CFD post-processing, as show in the scheme of fig. 6.9. The choice of a total integration length of 14 mm, although it does not correspond to the effective width of the measurement plane, is justified by the stochastic approach used for the spray simulation, where a reduced number of "parcels" are introduced in the computation domain. Each parcel represents statistically a large number of droplets having the same characteristics. If an integration width corresponding to the experimental one would be chosen, too few droplets were considered, giving an unsatisfactory result. This choice of the plane width provided the best qualitative match with the experimental results.

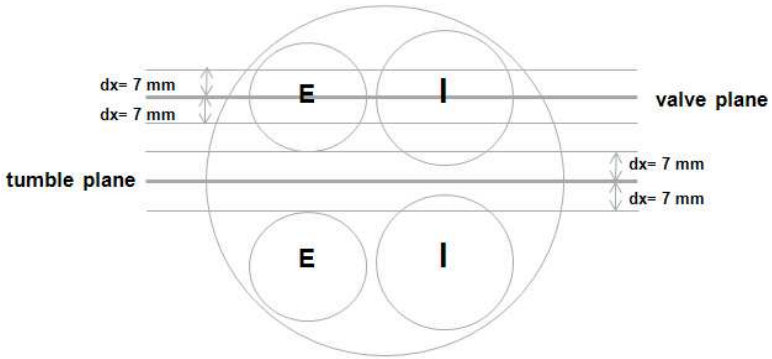

Figure 6.9: Scheme of the CFD post-processing integration area, top view, where I indicates the intake valves and E indicates the exhaust valves.

Results at different crankangles are presented in fig. 6.10 and fig. 6.11, respectively on the central tumble plane and on the valves plane. The experimental images were obtained measuring 10 consecutive cycles of injection. For each cycle, the images in gray scale are binarized and after selecting a certain gray threshold, the spray liquid contour is defined for each image. In this way, the probability of having the liquid fuel at a certain location is calculated over the 10 cycles of measurement (part (d) in figures). Also the averaged intensity images are presented (part (c) in figures), since these pictures provides a qualitative information on the liquid mass quantity of spray presents at each location. The CFD and also the experimental images are presented with the same dimension scale, in order to allow a better comparison, although no quantitative data were extracted. It is possible to evince that the spray model is capable to well reproduce the spray shape and penetration at each crankangle, confirming the suitability of the model for the final purpose of investigating the mixture formation in-cylinder. It is furthermore interesting to observe that the model is capable to correctly predict also the spray bending at late crankangles due to the effects of the air tumble motions. The good accuracy of the spray shape also in the valves plane confirm that the overall spray shape in the CFD model is correctly reproduced. Since the CFD droplets visualization (part (a) of the figure) in the central tumble plane shows all the droplets present in the combustion chamber, this figure is not repeated for the valves plane figure.

An example of the CFD-methodology purpose can be the investigation of different SOI strategies, in order to understand the effects on the mixture homogeneity and the wall impingement. A method to post-process the obtained data to obtain a reduced number of graphs or parameters summarizing the simulation results, will be presented in the chapter 7. Here, to further confirm the model capability to properly represent the

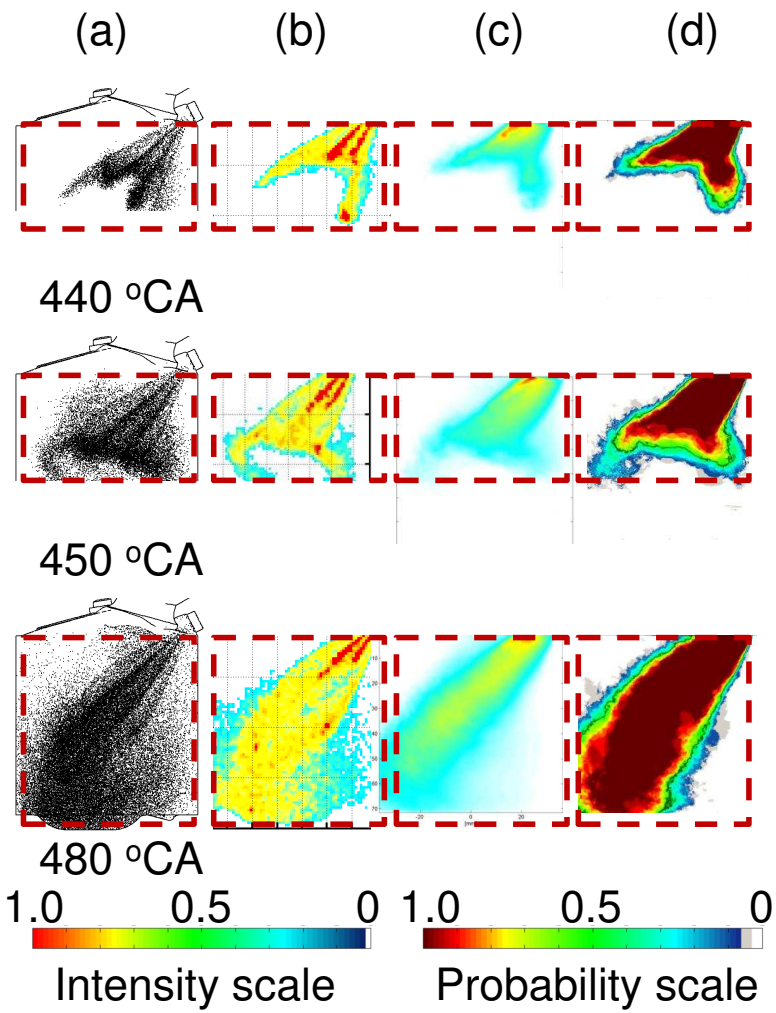

Figure 6.10: Spray visualization in the central tumble plane for SOI 430 °CA. CFD droplets (a), CFD "pseudo-Mie" (b), experimental averaged intensity (c), and experimental probability density (d).

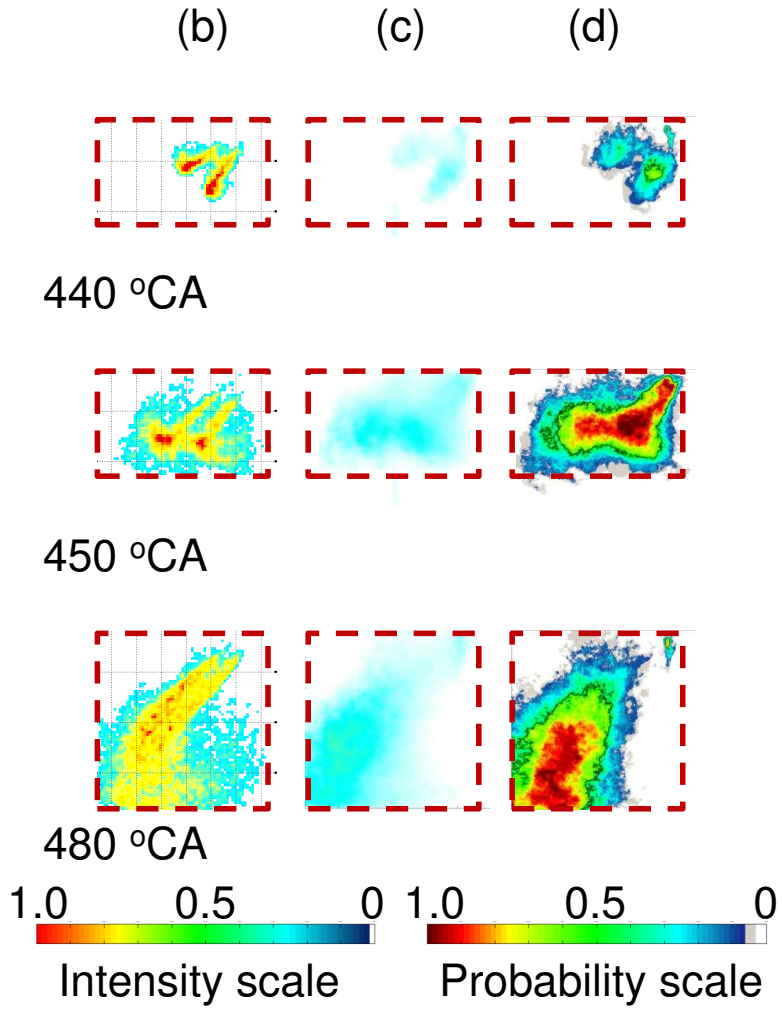

Figure 6.11: Spray visualization in the valves plane for SOI 430 °CA.

injection process, a second simulation with a different SOI is shown in fig. 6.12 and fig. 6.13. In this case a SOI of 410 °CA was used, keeping all the other parameters constant. For this simulation experimental images were compared as well. Also in this case the spray shape is correctly reproduced and the agreement is satisfactory. Furthermore, this assesses that the spray model reacts well to small changes of chamber back pressure, without requiring a new calibration. Figures are proposed with the same crankangle timing after SOI as for the case with SOI 430 °CA. It is interesting to observe that, due to the different in-cylinder pressure and air motion during the injection event, the spray shape differs from that obtained with the other SOI, and in particular the spray results more spread and more bended at late crankangles, due to the higher velocities in-cylinder. The model is capable to correctly reproduce these phenomena.

Calibration of the model performed at one operating conditions for a certain injector results thus valid for a wide range of different operating conditions. On the contrary, a new calibration is necessary in case of a different injector, although only a limited number of parameters have to be modified, as explained in the next section.

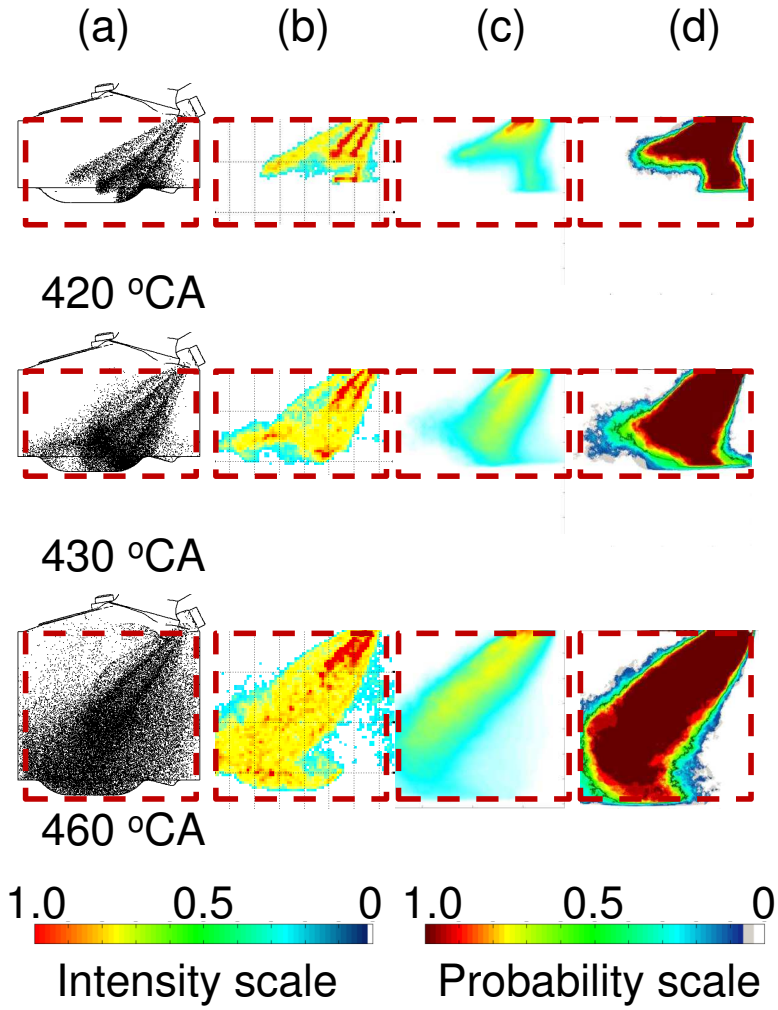

Figure 6.12: Spray visualization in the central tumble plane for SOI 410 °CA.

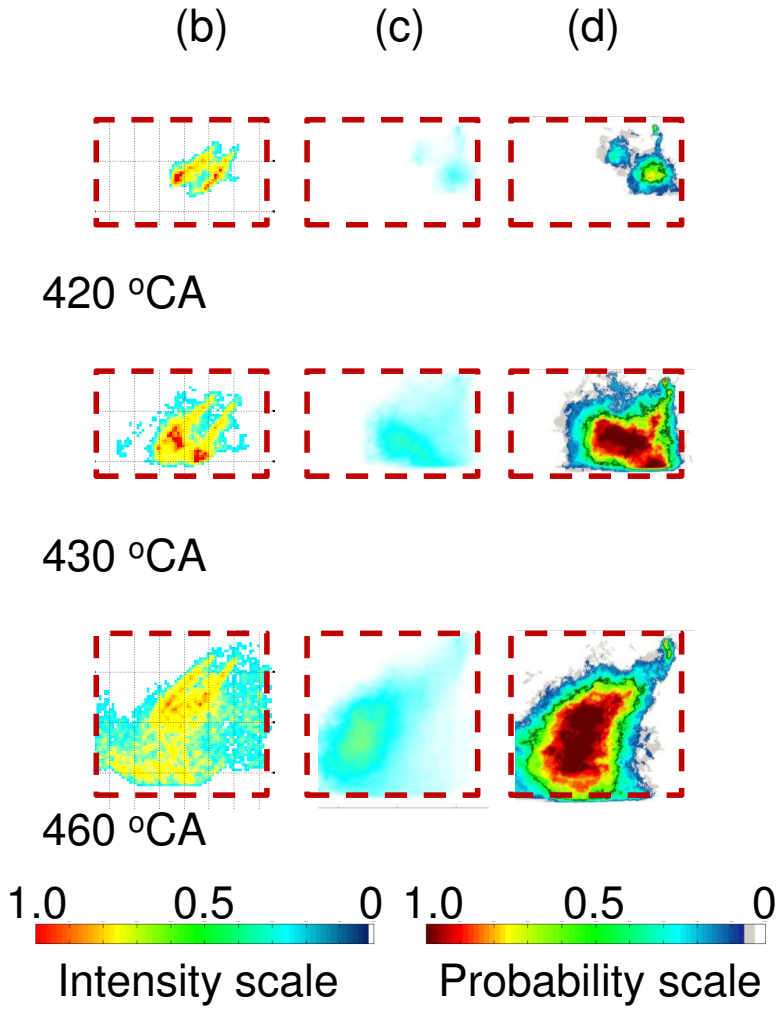

Figure 6.13: Spray visualization in the valves plane for SOI 410 °CA.

6.5 Results for Engine 2

In order to test the injection model also in a different engine and for a different injector, the Engine 2 already investigated for the cold-flow simulations was used to perform a in-cylinder analysis of injection process.

The experimental setup was the same already described, except for the optical engine geometry which was obviously changed in its rapid prototyping intake and exhaust, glass liner and piston, to reflect the design of the investigated engine, whose main characteristics are summarized in tab. 5.1 on page 51. It is important to notice that in this case we are dealing with a central injector location. In this way, the model is tested for both the central and side injector configurations.

6.5.1 Model calibration

The injection simulations were performed considering a 7-hole Bosch injector. In this way, it was possible to test the injector model also with a different injector. A new model calibration was performed, using experimental images obtained with 150 bar injection pressure, which corresponds to the one used in this case for the in-cylinder investigations, and 1 bar back pressure.

The mass flow rate used in the CFD simulation is presented in fig. 6.14, scaled as before using Bernoulli's law for an injection pressure of 150 bar, and considering the static mass flow of 7.2 g/s at 100 bar provided by the injector supplier. The opening ramp and closing ramp were built according to the injector supplier indications.

In fig. 6.15 is reported the spray penetration obtained from the CFD simulation in the quiescent chamber, compared with the experimental one. For the experimental measurements, also in this case the data from 10 consecutive injections were averaged, and for the CFD simulations the same grid of the

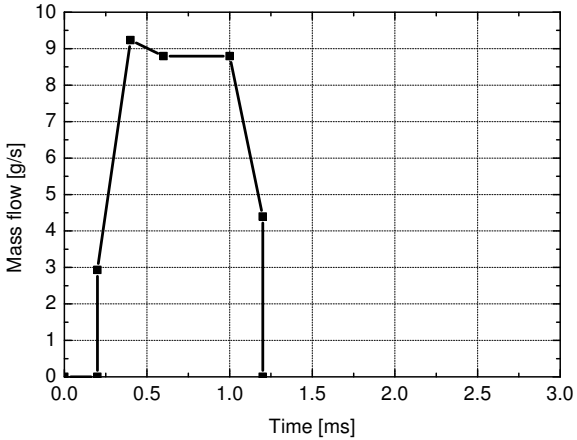

Figure 6.14: Mass flow rate for the model calibration of the 7-hole injector.

previous calibration was used.

Also with this different injector, it was possible to find an appropriate set of model parameters in order to achieve the correct penetration. Observing the graph in fig. 6.15, it could seem that the penetration in the last phase of the simulation is overestimated. However, the measured penetration is in this phase not consistent, due to the high evaporation of the spray. Comparing the images presented in fig. 6.16, it is possible to observe that the experimental and calculated spray penetrations are in good agreement also in the late phase. Anyhow, it is necessary to remark that a more accurate comparison was not possible because only the liquid phase is visible with the Mie-scattering technique, and no information was available on the fuel evaporation obtained with other experimental techniques, such as the LIF.

It can be observed that, despite the complete different shape of the spray in comparison with the pattern of the pre-

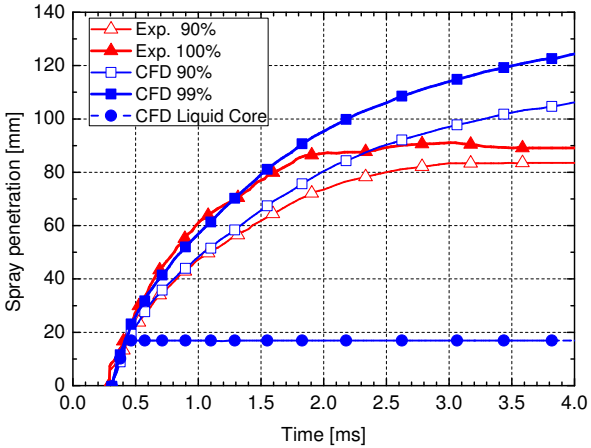

Figure 6.15: Spray penetration for the model calibration of the 7-hole injector.

vious injector, the CFD model is capable to well represent it. Furthermore, it is important to point out that, in comparison with the parameters used for the previous injector, the Hiroyasu constant in eq. (6.1) was changed, in order to reduce the liquid core length, and the droplet size constant in eq. (6.9) was modified, to obtain slightly larger droplet sizes, as indicated by the injector supplier, since no SMD measurements were directly available. In addition to the two mentioned constants, only the hole diameter was modified, using a diameter of 178 μm, which corresponds to the value measured with optical microscopy. Already with a limited number of calibration parameters, the model seems thus able to correctly provide an appropriate spray shape and penetration. This is particularly important for the use of the injection model from an OEM, where very often is necessary to compare different injector patterns or injector specifications, without having the possibility to recalibrate the model with optical images and measurements as comparison.

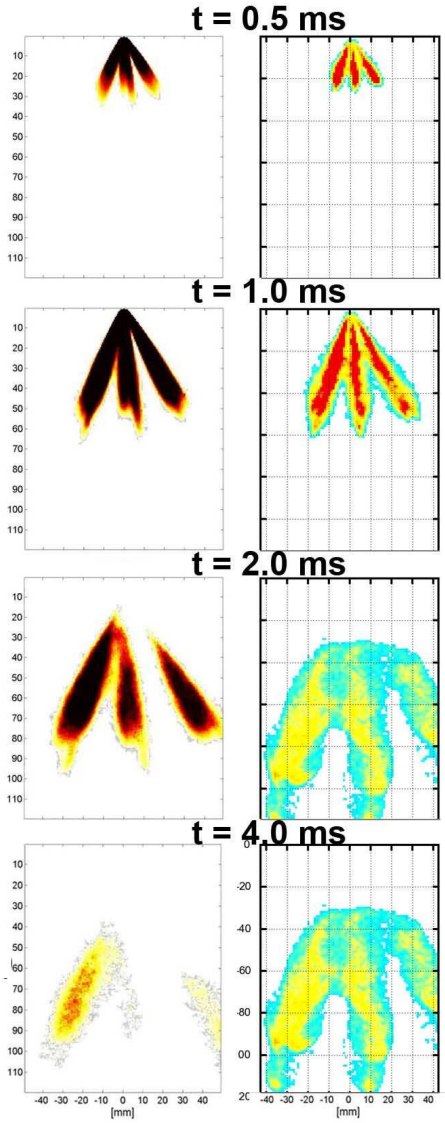

Figure 6.16: Spray images for the model calibration of the 7-hole injector.

6.5.2 In-cylinder results

To finally assess the spray model also in-cylinder, an engine injection simulation was performed, after the calibration in the quiescent chamber described in the previous section. As usual, results obtained with optical measurements were compared with the already described methodology. In this case, optical measurements on the tumble and cross-tumble central planes were available.

The operating point corresponds to that already reported in tab. 5.3 on page 72. A comparison between CFD images of the injection process and the experimental spray probability and averaged intensity images is presented in fig. 6.17 on the central tumble plane, and in fig. 6.18 on the central cross-tumble plane. The SOI was in this case 440 °CA with a DOI 26 °CA, corresponding to a total injected mass of 46.1 mg. The mass flow rate was defined as for the calibration case, adjusting the event duration.

The figures are scaled with the same size, in order to facilitate the visual comparison. In the Mie-measurements, the laser sheet was produced from the left side of the image. For this reason the jet on the right shows a lower detected light intensity, although it should have the same mass as the other beams. From a visual comparison on both the planes, it emerges that the spray shape was correctly reproduced by the CFD model, as well as the spray penetration.

It is important to notice that, while in the quiescent chamber injection the counter pressure remains constant, in an in-cylinder simulation the pressure changes during the injection event, although in a reduced range, since the intake valves are generally open when the injection occurs. This constitutes a further challenge for the injection model, since the droplet sizes and the cavitation model depend also from the gas pressure. Therefore, the satisfactory results obtained in the in-cylinder simulation confirm the reliability of this model, despite its sim-

plicity.

As far as the comparison for the late intake stroke is concerned, it is difficult to properly compare the experimental images with the CFD ones, since most of the liquid is at this time evaporated, but no measurement of the vapor phase was performed. However, as described in section 6.2, an attempt to improve the evaporative behavior in the model, with respect to a single-component fuel, was done.

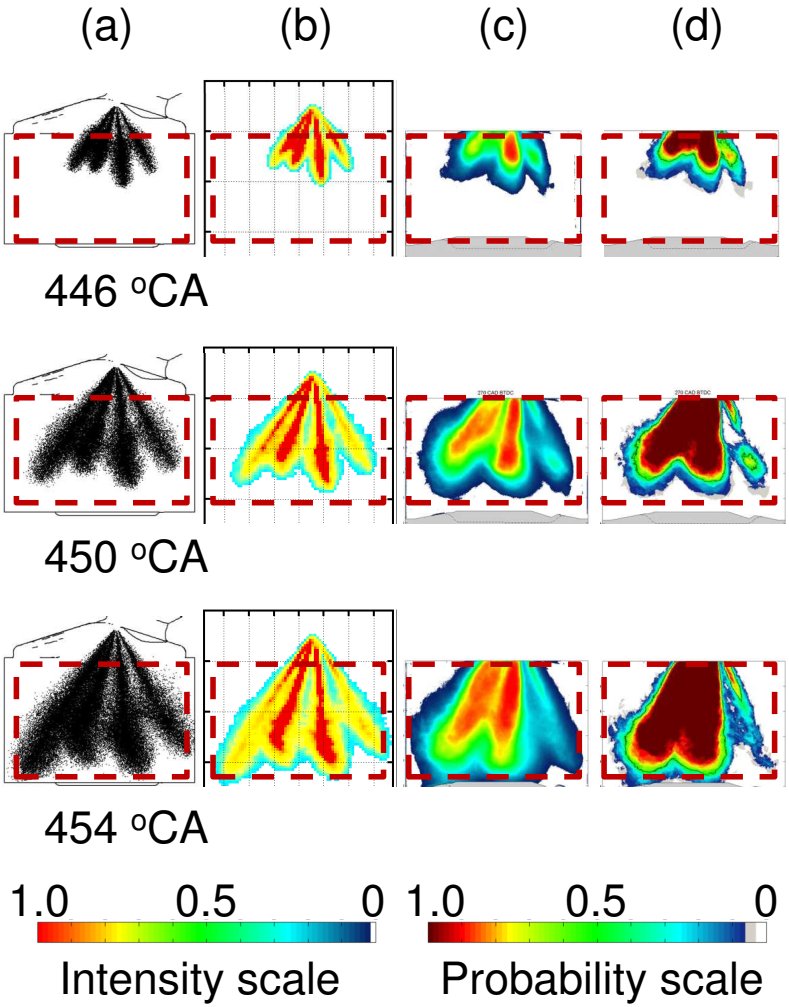

Figure 6.17: CFD droplets (a), CFD "pseudo-Mie" (b), experimental averaged intensity (c), and experimental probability density (d) for the in-cylinder injection simulation of Engine 2 on central tumble plane.

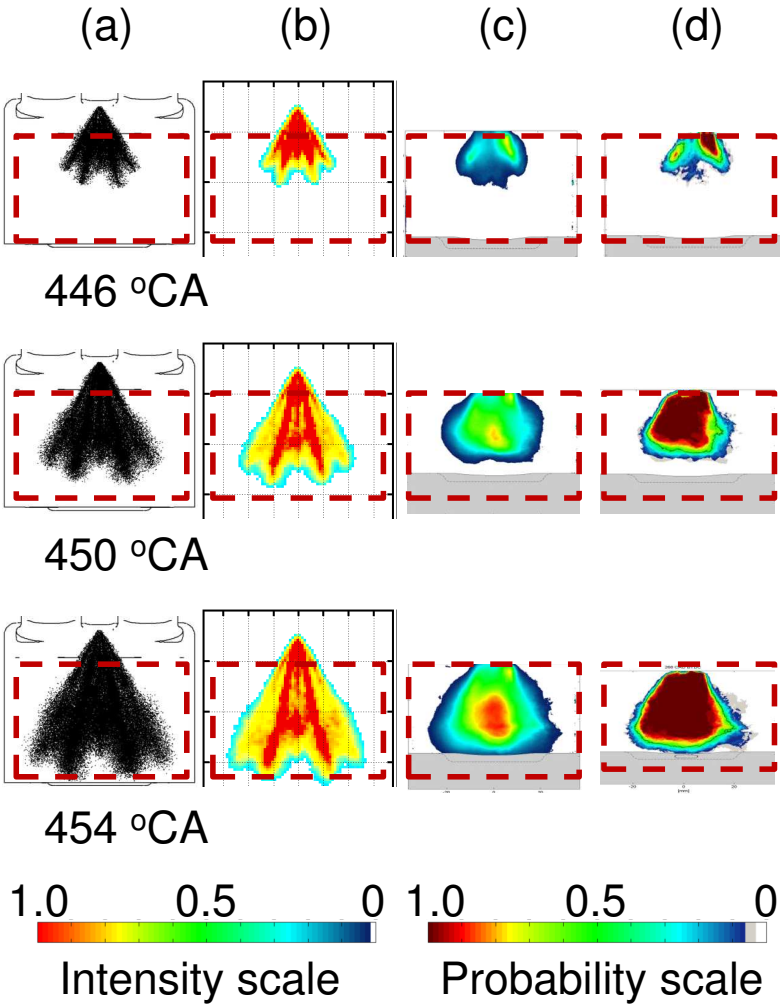

Figure 6.18: CFD droplets (a), CFD "pseudo-Mie" (b), experimental averaged intensity (c), and experimental probability density (d) for the in-cylinder injection simulation of Engine 2 on central cross-tumble plane.

6.6 Conclusions

In this chapter, the injection simulations performed on two different engines, one having a side injector and the other a central injector, were discussed. The model adopts a simplified approach, without taking into account the flow inside the nozzle, which deeply affects the primary atomization. However, it was shown that, with a reduced number of parameters required to calibrate the model, it is possible to reproduce correctly the spray shape, spray penetration and, where measurements were available, also the global droplet size.

No assessment on the accuracy of the evaporation modeling was possible, since laser induced fluorescence images, useful to visualize the vapor phase, were not available. No wall film model was used, due to the lack of experimental data necessary to validate it, but the prerequisite of having a correct spray penetration was respected, as shown in the comparison images.

Despite the uncertainties due to the above mentioned lack of experimental data to further validate the results of the simulation, the model demonstrated to be suitable to perform investigations on different spray targetings or injection strategies, which are generally the main purpose of the injection simulation. A way to compare synthetically the results of different simulations will be presented in the next chapter.

Chapter 7

Diagnostic indexes for the evaluation of simulation results

In the previous chapters the simulation methodology for cold-flow simulation and injection simulation was presented and validated through the comparison with optical data.

In this chapter, some procedures to synthetically analyze and interpret the obtained data will be presented, in order to be able to summarize the results of a CFD simulation in a limited set of indexes capable to drive the development process.

7.1 Lambda homogeneity

An important parameter to characterize the fuel-air mixture of a spark-ignited engine is the air/fuel equivalence ratio, or λ (lambda). It is well known that gasoline engines can work only in a narrow range of lambda around the stoichiometric air-fuel ratio (corresponding to $\lambda = 1$), even more reduced due to the aftertreatment requirements.

The global lambda evolution in-cylinder during the fuel

evaporation can be obtained from the CFD simulations. In the proposed methodology, the liquid fuel evaporates into two different scalars representing the two gaseous components of fuel. For each cell, summing the mass fraction of each scalar, it is possible to determine the fuel/air fraction of that cell. Comparing this ratio with the stoichiometric one, it is possible to determine the lambda value in each cell.

If the injected quantity is correctly calculated and the fuel evaporates completely, the global lambda value will reach the desired value in proximity of the TDC, as shown in fig. 7.1, which refers to the simulation results with different SOI for the operating point at 18 bar imep in tab. 5.2 on page 53.

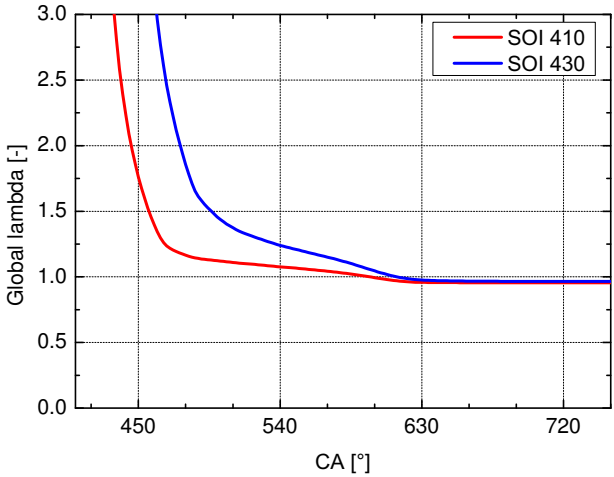

Figure 7.1: Global lambda for Engine 1 simulation, 18 bar imep.

Although the global lambda value is near the stoichiometric value as desired for both the SOI, few information about the mixture quality can be obtained looking at the global air-fuel ratio. Much more interesting is the achieved mixture homogeneity in the cylinder, which can be evaluated through the

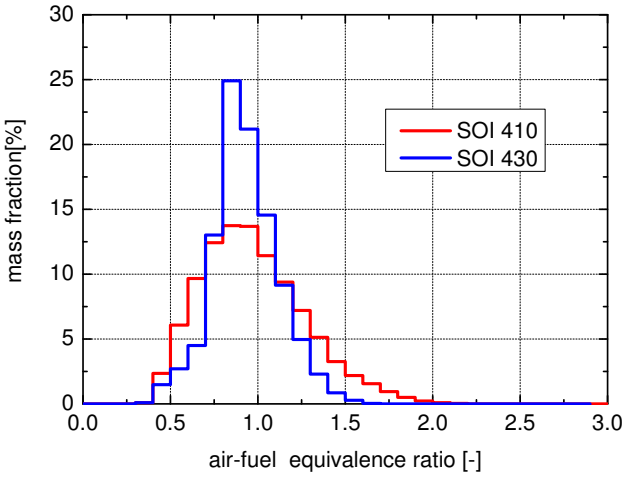

Figure 7.2: Lambda distribution in-cylinder for Engine 1 simulation, 18 bar imep.

histogram in fig. 7.2. The histogram represents the mass distribution of lambda in the cylinder. In this way, it is possible to have a quantitative evaluation of the achieved homogeneity, represented by the dispersion of the data, which is related to the histogram width, if the classes are kept constant in the different simulations.

In order to further summarize the results, the whole histogram could be condensed considering the ratio $r = 1/x_{max}$, where x_{max} is the maximum volume fraction. In case of a completely homogeneous mixture, thus with all the in-cylinder mass with a fixed value of lambda, the value of r would be 1. Higher values of r indicate a less homogeneous mixture, therefore when comparing two injection strategies or two injector targetings, the one with the lower r ratio has to be preferred. A more precise evaluation, considering not exclusively the mass fraction in the most frequent lambda class, but the effective dispersion, can be obtained evaluating the Coefficient of Vari-

ation COV [77]. The COV can be defined as:

$$\mathrm{COV} = \sqrt{\frac{1}{m}\sum_{i=1}^{n} m_i(\lambda_i - \lambda)^2} \tag{7.1}$$

where m is the total in-cylinder mass, λ the global air-fuel equivalence ratio, and the i subscript indicates the local values of the i-th cell.

Observing the results shown in fig. 7.2, which reports the lambda classification in the cylinder at 700 °CA, it can be evinced that the SOI at 430 °CA allows to obtain a better homogenization. Despite an earlier SOI provides a longer time available for the evaporation and fuel mixing, in this case a later injection timing enhances an higher fuel spreading in the combustion chamber, since the injection takes place when the charge motion in the cylinder has its maximum speed. Observing the lambda distribution in the tumble and cross-tumble central planes, presented in fig. 7.3 at BDC and in fig. 7.4 at 700 °CA, the higher homogeneity obtained with a late injection timing is evident. The earlier evaporation due to the early injection causes a rich area near the piston at BDC, which cannot be further homogenized, resulting in a worst homogeneity also at the spark timing.

A more precise evaluation of the homogeneity in-cylinder can be obtained considering the COV. In the analyzed case, as shown in fig. 7.5, the later timing allows to obtain an improvement in the homogeneity of approximately 20%, and the mixture results at every crankangle more homogeneous than the one obtained with the early injection.

The same evaluations already described for the whole cylinder can be done also for the volume near the spark; in this work, a sphere of 5 mm radius around the spark-electrode location was considered. The evolution in time of the lambda value near the spark, presented in fig. 7.6, can be related to the ignition stability of the mixture. Therefore, a more constant

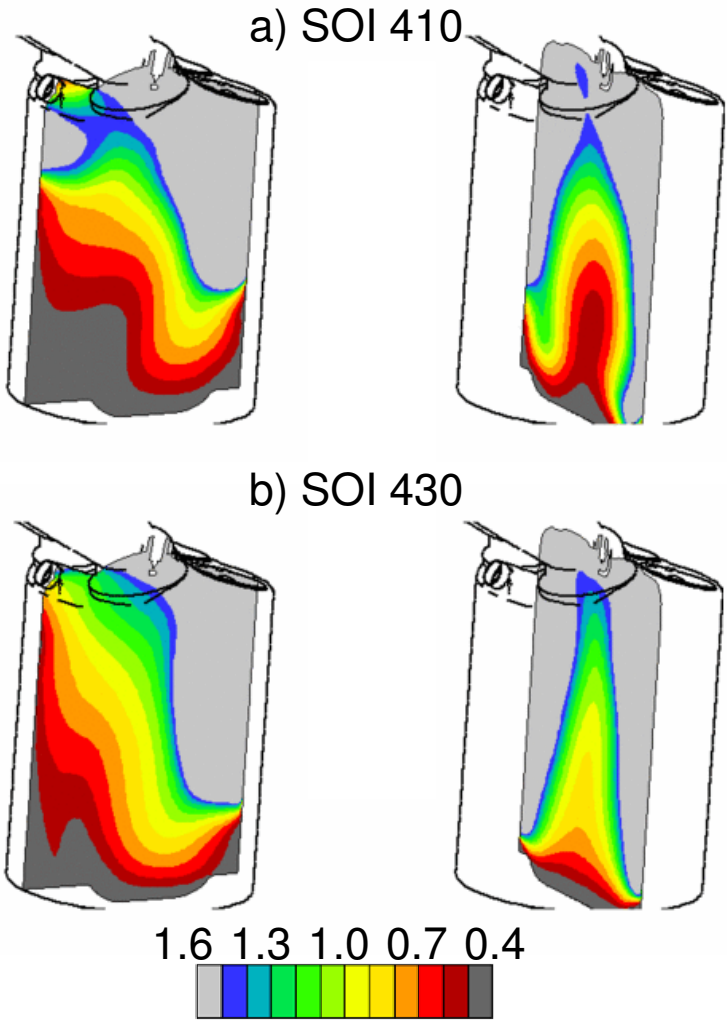

Figure 7.3: Air-fuel equivalence ratio in-cylinder at BDC.

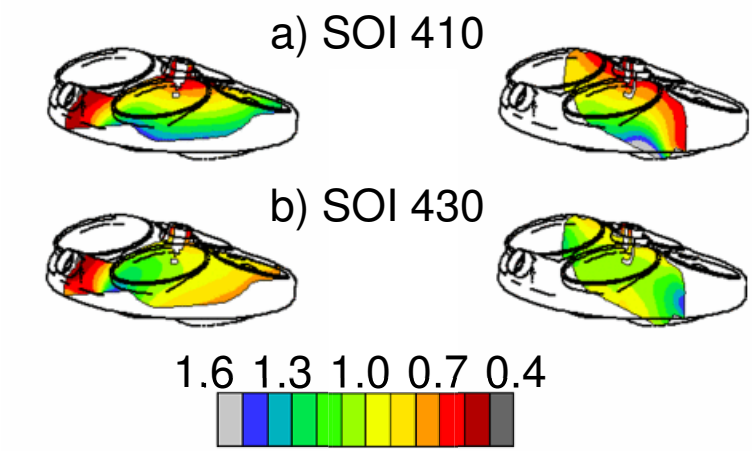

Figure 7.4: Air-fuel equivalence ratio in-cylinder at 700 °CA.

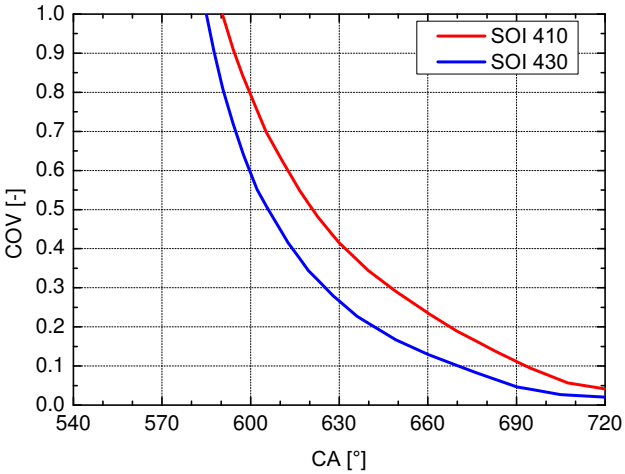

Figure 7.5: Coefficient of Variation (COV) for Engine 1 simulation with different SOI.

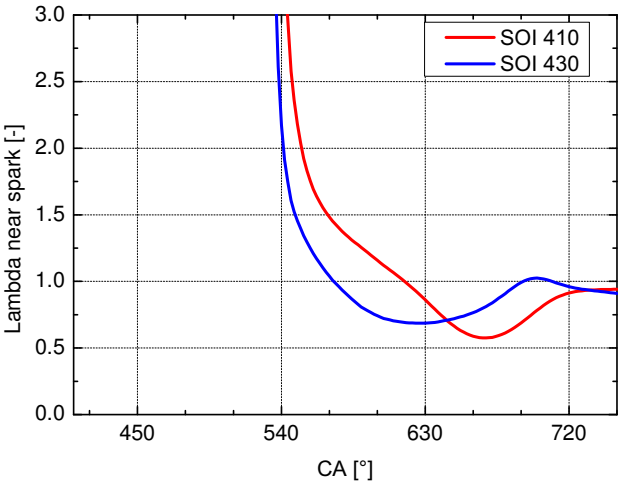

Figure 7.6: Air-fuel equivalence ratio near the spark plug for Engine 1 simulation.

value, and possibly in the slightly rich range (λ less than 1), indicates a better stability of the mixture near the spark, allowing more degree of freedom in the choice of the spark timing. The late injection is also in this case convenient. Despite a later fuel evaporation, the mixture formation process takes advantages from an higher mixing. The homogenization is in fact enhanced by the injection during the phase of highest in-cylinder velocities. Hence the charge motion transports the mixture in a favorable way near the spark plug.

7.2 Wall impingement

As discussed in section 6.3, in this work the choice of avoiding the use of the wall impingement model available in the software was done. This was due to the impossibility to validate the model, and to the experience acquired by the author

on the extreme sensibility of this model to the mesh quality near the wall, the wall temperatures, the time step and even the restart of a simulation. The dependence of the results on all the mentioned parameters prevents from obtaining reproducible solutions and comparable results between two simulations. Furthermore, it should be pointed out that some of these parameters can be physically related to the mechanism of wall film formation, while some others are clearly due just to some implementation problems[1].

Nevertheless, the spray simulation is robust enough, as demonstrated in chapter 6, to consider only the liquid fuel near the liner, the piston and the valves, in order to obtain information about the tendency to wall impingement of a certain injector. In particular, the droplets mass in a circular layer with 1 or 2 mm width from the liner wall was considered, as well as the droplets mass in a layer of 2 mm width from the piston crown. Results of this evaluation are presented respectively in fig. 7.7 and 7.8.

It is interesting to notice how in this case the early timing leads to an higher liner impingement. Despite the higher position of the piston when the injection begins with the early timing, the piston impingement is comparable with both the strategies. Due to the higher momentum exchange in case of the late injection, the droplets are transported by the tumble motion toward the piston, causing the second peak in the piston impingement graph. Although in case of early injection the first peak is higher, the integral impingement results similar for both the strategies.

The liner impingement can be correlated with the tendency to oil dilution, while the valve and piston impingement can be correlated with the soot formation. In fact, late fuel evaporation or even liquid droplets remaining on the piston or valves can lead to pool flames, responsible for the soot forma-

[1]The last version of the software used for this work was the 4.18.

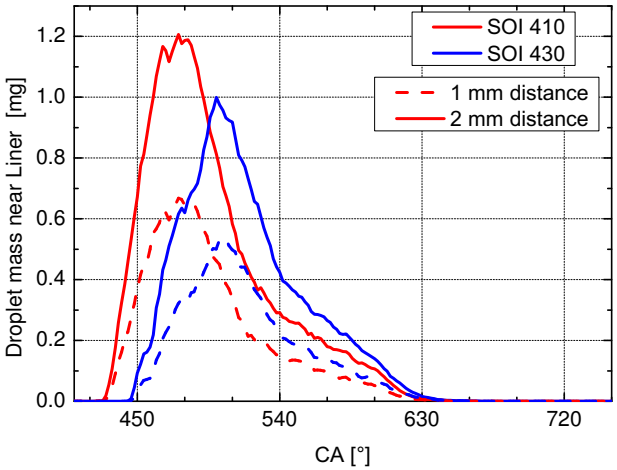

Figure 7.7: Liner impingement.

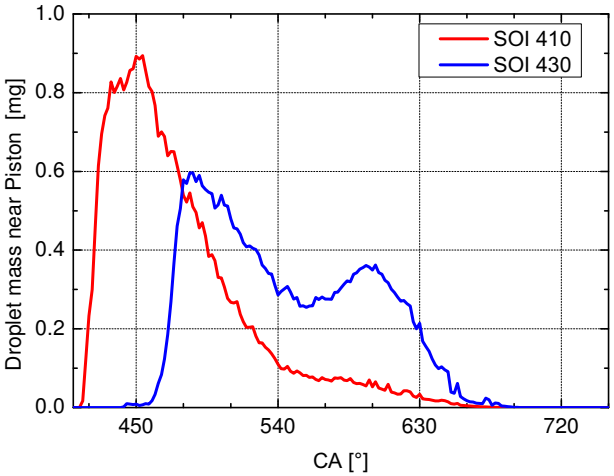

Figure 7.8: Piston impingement.

tion [78, 79]. The integrated mass in proximity of the piston and the valves seems to well correlate with the smoke number measured at the test-bench, while the mass near the liner well correlates with the oil dilution. In fig. 7.9 the CFD results are compared with the experimental data. Results in fig. 7.9 do not refer to Engine 1 and 2 previously analyzed, since obviously no data for the oil dilution and soot formation were available for the motored optical engine. The results refer indeed to a simulation performed with the presented methodology on a passenger car FIAT 4-cylinder engine [80]. The values cannot be directly compared, because referred to different physical quantities. Nevertheless, it can be observed that the qualitative and quantitative trend obtained at the test-bench varying the SOI can be reproduced with the CFD simulations. This allows to use CFD simulations to investigate different injection strategies, or injector targetings, and quantitatively evaluate the effects they will have on the oil dilution and soot formation.

However, it has to be pointed out that the quantitative information are valid when referred to the same engine. On the contrary, according to the author's experience, no correlation can be found between the results obtained for different engines. Therefore it is impossible to define a threshold value under which the mass of liquid near the piston, valves or liner, has to be considered critical, since it changes from engine to engine. However, it can be predicted which injection strategy or targeting will produce the lower impingement, obtaining also a quantitative evaluation of the differences.

The injection timing in GDI engines is always a trade-off between a good mixture homogeneity, for which an advanced SOI is generally advantageous, and the piston impingement, for which a late injection timing is favorable. On the contrary, the trend of valve and liner impingement by changing the SOI is more variable. In particular, the valve impingement de-

pends also on the valve timing, and thus the valve lift, during the injection event. The liner impingement is influenced by the interaction between the droplets and the charge motion. Since no quantitative threshold can be defined both for the COV and the soot and oil dilution indexes, it is necessary to evaluate each case in detail, in order to decide which could be the best strategy in terms of timing or targeting definition.

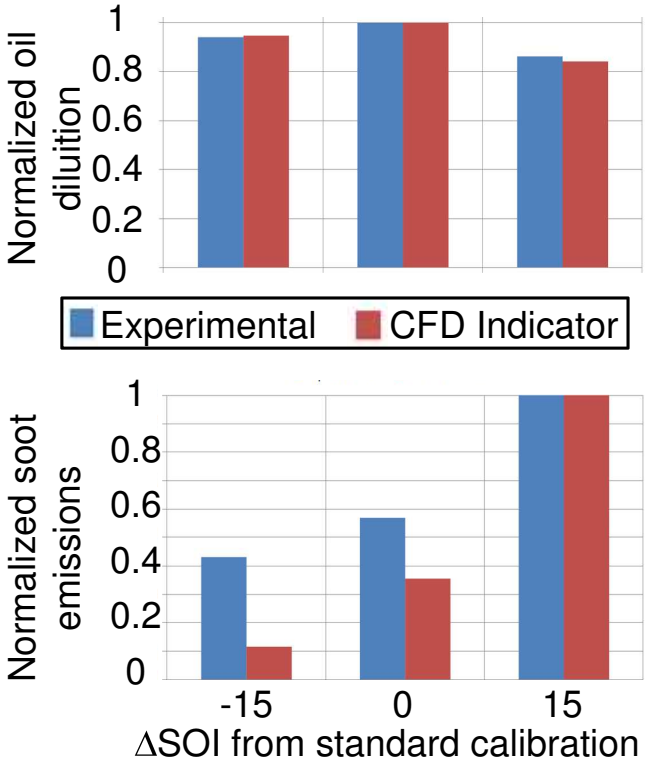

Figure 7.9: Comparison of CFD oil dilution (full load, 5000 rpm) and soot formation (full load, 1500 rpm) indexes with experimental data for different injection timings.

It is important to stress that CFD helps in having a better understanding of the involved phenomena and it provides a first ranking of the analyzed variants. Nevertheless, in case of reduced gap in the ranking evaluation, only an investigation at the test-bench will provide the necessary information to select the optimal variant.

Chapter 8

Conclusions and future perspectives

In this work a comprehensive procedure for the simulation of spark-ignited combustion engines was proposed. The methodology focused on the current state of art, taking into account the constraints in terms of calculation time, memory and computational resources presently acceptable in an industrial environment.

For this reason a RANS approach for the turbulence was chosen, and a Lagrangian-Eulerian method for the spray simulation was used. Both the choices are well established in the automotive industry, and are currently the most affordable in terms of computational requirements, providing at the same time satisfactory results with a reduced amount of input information.

Also the use of a commercial software is motivated by the aim to use the same methodology which is used in the industry, being thus capable to deal easily and fast with different complexes geometries. As far as the meshing and post-processing capabilities are concerned, the commercial software still have considerable advantages even on the most developed

open source solution, namely Open-FOAM. Despite Open-FOAM offers a full accessible code, this is considered less relevant in the industry, where the aim is not to develop the CFD simulation itself, but to use it as a tool for the engine design.

This work contributes with an extensive comparison of the most known and used models with optical experimental data. The models generally adopted for the turbulence simulations were compared with PIV measurements from two different engines and different operating conditions.

As far as the injection is concerned, a Lagrangian-Eulerian model capable to take into account the liquid core was adopted, adapting it from the Diesel application for which has been developed. Even in this case, optical data were presented, and compared with the results obtained with CFD.

Air motion and spray injection are and will remain for a long time the main areas of interest for the application of the in-cylinder simulations for gasoline direct injection engines. An example of how the CFD simulations can be used to address the problem of wall impingement, which is currently of high importance especially for downsized engines, was presented.

However, it is necessary to remark that also the simulation of the combustion is becoming nowadays more important. At the moment, many different phenomenological models are available to simulate the combustion. However, they normally require a careful calibration, and are generally not capable to predict the combustion anomalies such as pre-ignition or knocking, which are of major interest in the modern extremely downsized and turbocharged gasoline engines. In the future, considering also the higher computational and memory resources available, these themes will be probably addressed with the use of a LES approach and reaction kinetic.

The proposed methodology is capable to help in the normal activities of a gasoline engine development, such as the port

design and the injector targeting definition. Although specifically developed for gasoline engines, it can be deemed suitable for every spark-ignited engine and it was used by the author, during its work at Politecnico di Torino and FEV GmbH in Aachen, for many different engines.

Bibliography

[1] J. H. Johnson, *SI Engine Emissions*. Society of Automotive Engineers, 2005.

[2] R. Van Basshuysen, *Ottomotor mit Direkteinspritzung*. Vieweg Teubner Verlag, 2008.

[3] (2013, February) Emission standards for Europe. [Online]. Available: http://www.dieselnet.com/standards/eu/ld.php

[4] F. Zhao, D. L. Harrington, and L. M., *Automotive Gasoline Direct-Injection Engines*. SAE International, 2002.

[5] A. Königstein, U. D. Grebe, K. J. Wu, and P. I. Larsson, "Differentiated analysis of downsizing concepts," *MTZ worldwide*, vol. 69, no. 6, pp. 4–11, 2008.

[6] B. Stojkovic, T. Fansler, M. Drake, and V. Sick, "High-speed imaging of OH* and soot temperature and concentration in a stratified-charge direct-injection gasoline engine," *Proceedings of the Combustion Institute*, vol. 30, no. 2, pp. 2657–2665, 2005.

[7] P. Price, R. Stone, T. Collier, and M. Davies, "Particulate matter and hydrocarbon emissions measurements: comparing first and second generation DISI with PFI in single cylinder optical engines," *SAE Technical Paper*, no. 2006-01-1263, 2006.

[8] M. Q. Lin, P. Zhou, J. Qin, Y. G. Pei, and S. Z. Pan, "The analysis of GDI engine soot emission based on spray and ignition timing tactics," in *2nd International Conference on Electronic & Mechanical Engineering and Information Technology (EMEIT-2012)*, 2012, pp. 1769–1773.

[9] M. Lindhal, "Engineering designers' requirements on design for environment methods and tools," Ph.D. dissertation, KTH, School of Industrial Engineering and Management (ITM), Machine Design (Dept.), Machine Design (Div.), 2005.

[10] J. D. Anderson, *Computational Fluid Dynamics*. McGraw-Hill, 1995.

[11] C. Hirsch, *Numerical computation of internal and external flows: fundamentals of computational fluid dynamics*, 2nd ed. Butterworth-Heinemann, 2007.

[12] J. H. Firziger and P. Milovan, *Computational Methods for Fluid Dynamics*, 3rd ed. Springer, 2002.

[13] P. Adomeit, O. Lang, S. Pischinger, R. Aymanns, M. Graf, and G. Stapf, "Analysis of cyclic fluctuations of charge motion and mixture formation in a DISI engine in stratified operation," *SAE technical paper*, no. 2007-01-1412, 2007.

[14] O. Vermorel, S. Richard, O. Colin, C. Angelberger, A. Benkenida, and D. Veynante, "Towards the understanding of cyclic variability in a spark ignited engine using multi-cycle LES," *Combustion and Flame*, vol. 156, no. 8, pp. 1525–1541, 2009.

[15] D. Wilcox, *Turbulence Modeling for CFD*. DCW Industries, 1993.

[16] S. Pope, *Turbulent flows*. Cambridge University Press, 2000.

[17] B. Launder and D. B. Spalding, "The numerical computation of turbulent flows," *Computer methods in applied mechanics and engineering*, vol. 3, no. 2, pp. 269–289, 1974.

[18] B. E. Launder and B. Sharma, "Application of the energy-dissipation model of turbulence to the calculation of flow near a spinning disc," *Letters Heat Mass Transfer*, vol. 1, pp. 131–137, 1974.

[19] W. Jones and B. Launder, "The prediction of laminarization with a two-equation model of turbulence," *International Journal of Heat and Mass Transfer*, vol. 15, no. 2, pp. 301–314, 1972.

[20] V. Patel, W. Rodi, and G. Scheuerer, "Turbulence models for near-wall and low Reynolds number flows: A review," *AIAA journal*, vol. 23, no. 9, pp. 1308–1319, 1985.

[21] *Star-CD Methodology*, CD-adapco.

[22] V. Yakhot and S. Orszag, "Renormalization group analysis of turbulence. I. Basic theory." *Journal of scientific computing*, vol. 1, no. 1, pp. 3–51, 1986.

[23] F. Tanner, G. Zhu, and R. Reitz, "A turbulence dissipation correction to the k-epsilon model and its effect on turbulence length scales in engine flows," in *International Multidimensional Engine Modeling Users Group Meeting at the SAE Congress, Detroit*, 2001.

[24] W. Rodi, "Influence of buoyancy and rotation on equations for the turbulent length scale," in *2nd Symposium on Turbulent Shear Flows*, vol. 1, 1979, p. 10.

[25] A. N. Kolmogorov, "Equations of turbulent motion of an incompressible turbulent fluid," *Izvestia Academy of Sciences*, vol. 6, no. 1 and 2, pp. 56–58, 1942.

[26] R. J. LeVeque, *Finite volume methods for hyperbolic problems*. Cambridge University Press, 2002.

[27] S. V. Patankar and D. B. Spalding, "A calculation procedure for heat, mass and momentum transfer in three-dimensional parabolic flows," *International Journal of Heat and Mass Transfer*, vol. 15, no. 10, pp. 1787–1806, 1972.

[28] R. I. Issa, "Solution of the implicitly discretised fluid flow equations by operator-splitting," *Journal of computational physics*, vol. 62, pp. 40–65, 1986.

[29] A. A. Amsden, J. D. Ramshaw, P. J. O'Rourke, and J. K. Dukowicz, "KIVA: A computer program for two- and three-dimensional fluid flows with chemical reactions and fuel sprays," Los Alamos National Lab., NM (USA), Tech. Rep., 1985.

[30] A. A. Amsden, "KIVA-3V: A block-structured KIVA program for engines with vertical or canted valves," Los Alamos National Lab., NM (United States), Tech. Rep., 1997.

[31] D. J. Torres and M. F. Trujillo, "KIVA-4: An unstructured ALE code for compressible gas flow with sprays," *Journal of Computational Physics*, vol. 219, no. 2, pp. 943 – 975, 2006.

[32] (2009, March) Advanced combustion engine R&D: Goals, strategies, and top accomplishments. [Online]. Available: http://www1.eere.energy.gov/vehiclesandfuels/pdfs/adv_combustion_goals.pdf

[33] *Es-Ice user guide*, CD-adapco.

[34] (2010, June) Convergent science simplifies CFD meshing for engine combustion modeling. [Online]. Available: http://www.sae.org/mags/aei/8073

[35] T. Lucchini, G. D'Errico, H. Jasak, and Z. Tukovic, "Automatic mesh motion with topological changes for en-

gine simulation," *SAE Technical Paper*, no. 2007-01-0170, 2007.

[36] H. Zhao, *Laser Diagnostics and Optical Measurement Techniques in Internal Combustion Engines.* SAE International, 2012.

[37] M. Lackner, *Lasers in chemistry - Volume 1.* Wiley, 2008.

[38] P. G. Merker, C. Schwarz, and R. Teichmann, *Combustion Engines Development: Mixture Formation, Combustion, Emissions and Simulation.* Springer, 2011.

[39] M. Reeves, D. P. Towers, B. Tavender, and C. Buckberry, "A high-speed all-digital technique for cycle-resolved 2-d flow measurement and flow visualisation within SI engine cylinders," *Optics and lasers in engineering*, vol. 31, no. 4, pp. 247–261, 1999.

[40] J. Westerweel, "Fundamentals of digital particle image velocimetry," *Measurement Science and Technology*, vol. 8, no. 12, p. 1379, 1999.

[41] R. A. Mugele and H. D. Evans, "Droplet size distribution in sprays," *Industrial & Engineering Chemistry*, vol. 43, no. 6, pp. 1317–1324, 1951.

[42] A. H. Lefebvre, *Atomization and sprays.* Taylor & Francis, 1989.

[43] N. Ashgriz, *Handbook of Atomization and Sprays: Theory and Applications.* Springer, 2011.

[44] R. Flierl, F. Lauer, S. Schmitt, and U. Spicher, "Potentials and limits of CO_2 emissions of gasoline engines. Part 2: new combustion processes," *MTZ 73*, 2012.

[45] S. Pischinger, "Lectures notes, internal combustion engines," 2007.

[46] S. E. Parrish and R. J. Zink, "Spray characteristics of multi-hole injectors under flash boiling conditions," in

21st Annual Conference on Liquid Atomization and Spray Systems, 2008.

[47] V. Warnecke, E. Achleitner, and H. Bäcker, "Entwicklungsstand des Siemens VDO Piezo-Einspritzsystems für strahlgeführte Brennverfahren," in *27. Internationales Wiener Motorensymposium*, 2006.

[48] G. Bidone, *Experiences sur la forme et sur la direction des veines et des courants d'eau lances par diverses ouvertures.* Imprimerie Royale, 1829.

[49] J. A. F. Plateau, *Statique experimentale et theorique des liquides soumis aux seules forces moleculaires.* Gauthier-Villars, 1873.

[50] J. L. R. Strutt, "On the instability of jets," in *Proceedings of the London Mathematical Society*, vol. 10, 1879, pp. 4–13.

[51] C. Weber, "Disintegration of liquid jets," *Zeitschrift für Angewandte Mathematik und Mechanik*, vol. 11, no. 2, pp. 136–159, 1931.

[52] A. Haenlein, "Disintegration of a liquid jet," *National Advisory Commitee for Aeronautitics (NACA) Technical Memorandum 659*, vol. 2, no. 4, 1932.

[53] R. D. Reitz, "Atomization and other breakup regimes of a liquid jet," Ph.D. dissertation, Princeton University, 1978.

[54] W. Ohnesorge, "Formation of drops by nozzles and the breakup of liquid jets," *Zeitschrift für Angewandte Mathematik und Mechanik*, vol. 16, no. 4, pp. 355–358, 1936.

[55] E. Giffen and A. Muraszew, *The atomisation of liquid fuels.* Chapman & Hall, 1953.

[56] G. M. Faeth, L. P. Hsiang, and P. K. Wu, "Structure and breakup properties of sprays," *International Journal of Multiphase Flow*, vol. 21, pp. 99–127, 1995.

[57] S. Khosla, C. E. Smith, and R. P. Throckmorton, "Detailed understanding of drop atomization by gas crossflow using the volume of fluid method," in *ILASS Americas, 19th annual conference on liquid atomization and spray systems, Toronto, Canada*, 2006.

[58] W. Wiese, S. Pischinger, P. Adomeit, and J. Ewald, "Prediction of combustion delay and duration of homogeneous charge gasoline engines based on in-cylinder flow simulation," *SAE Technical Paper*, no. 2009-01-1796, 2009.

[59] M. Grill, T. Billinger, and M. Bargende, "Quasi-dimensional modeling of spark ignition engine combustion with variable valve train," *SAE Technical Paper*, no. 2006-01-1107, 2006.

[60] E. Delogu, "Development of a coupled 0D-3D CFD methodology for the simulation of the combustion process in S.I. engines," Master's thesis, Politecnico di Torino, 2009.

[61] V. Pignone and U. R. Vercelli, *Motori ad alta potenza specifica, le basi concettuali della tecnica da competizione*. Giorgio Nada Editore, 2003.

[62] Z. Y. Han and R. D. Reitz, "Turbulence modeling of internal combustion engines using RNG k-ε models," *Combustion Science and Technology*, vol. 106, pp. 267–295, 1995.

[63] *Star-CD User Guide*, CD-adapco.

[64] P. Adomeit, A. Brunn, R. Weinowski, M. Jakob, S. Pischinger, H. Kleeberg, and D. Tomazic, "A new approach for optimization of mixture formation on gasoline DI engines," *SAE Technical Paper*, no. 2010-01-0591, 2010.

[65] W. Piock, G. Hoffmann, A. Berndorfer, P. Salemi, and B. Fusshoeller, "Strategies towards meeting future partic-

ulate matter emission requirements in homogeneous gasoline direct injection engines," *SAE International Journal of Engines*, vol. 4, no. 1, pp. 1455–1468, 2011.

[66] A. Marchi, J. Nouri, Y. Yan, and C. Arcoumanis, "Spray stability of outwards opening pintle injectors for stratified direct injection spark ignition engine operation," *International Journal of Engine Research*, vol. 11, no. 6, pp. 413–437, 2010.

[67] A. B. Liu, D. Mather, and R. D. Reitz, "Modeling the effects of drop drag and breakup on fuel sprays," *SAE Technical Paper*, no. 930072, 1993.

[68] H. Hiroyasu and M. Arai, "Structures of fuel sprays in Diesel engines," *SAE Technical Paper*, no. 900475, 1990.

[69] W. H. Nurick, "Orifice cavitation and its effect on spray mixing," *ASME Transactions Journal of Fluids Engineering*, vol. 98, pp. 681–687, 1976.

[70] T. Schneider, "Zur Modellierung der Zerstäubung von Flüssigkeitsfreistrahlen," Ph.D. dissertation, Universität Dortmund, 1995.

[71] J. D. Naber and D. L. Siebers, "Effects of gas density and vaporization on penetration and dispersion of Diesel sprays," *SAE Technical Paper*, no. 960034, 1996.

[72] R. Reitz and R. Diwakar, "Effect of drop breakup on fuel sprays," *SAE Technical Paper*, no. 860469, 1986.

[73] C. Baumgarten, *Mixture formation in internal combustion engines*. Springer, 2006.

[74] B. Befrui, G. Corbinelli, M. D'Onofrio, and D. Varble, "GDI multi-hole injector internal flow and spray analysis," *SAE Technical paper*, no. 2011-01-1211, 2011.

[75] P. G. Aleiferis and Z. R. van Romunde, "An analysis of spray development with iso-octane, n-pentane, gasoline,

ethanol and n-butanol from a multi-hole injector under hot fuel conditions," *Fuel*, 2012.

[76] C. Bai and A. D. Gosman, "Development of methodology for spray impingement simulation," *SAE technical paper*, no. 950283, 1995.

[77] F. Millo, M. Badami, A. Bianco, and E. Delogu, "CFD diagnostic methodology for the assessment of mixture formation quality in GDI engines," *SAE International Journal of Engines*, vol. 4, no. 2, pp. 2461–2476, 2011.

[78] E. Stevens and R. Steeper, "Piston wetting in an optical DISI engine: fuel films, pool fires, and soot generation," *SAE Technical Paper*, no. 2011-01-1203, 2001.

[79] A. Warey, Y. Huang, R. Matthews, M. Hall, and H. Ng, "Effects of piston wetting on size and mass of particulate matter emissions in a DISI engine," *SAE Technical Paper*, no. 2002-01-1140, 2002.

[80] D. Andriesse, E. Comignaghi, G. Lucignano, A. Oreggioni, S. Quinto, and S. D., "The new 1.8 ltr DI turbojet gasoline engine from Fiat Powertrain Technologies," in *17th Aachener Kolloquium Fahrzeug und Motorentechnik*, 2008.

List of Publications

[1] F. Millo, M. Badami, A. Bianco, and E. Delogu, "CFD Diagnostic Methodology for the Assessment of Mixture Formation Quality in GDI Engines," *SAE International Journal of Engines*, vol. 4, no. 2, pp. 2461-2476, 2011, DOI: 10.4271/2011-24-0151.

[2] A. Bianco, E. Delogu, F. Millo, D. Ceratto and S. Ravina, "A numerical 1D-3D investigation on different LPG injection strategies and engine concepts," *Société des Ingénieurs de l'Automobile (FRA), The Spark Ignition Engine of the Future*, Strasbourg (France), Nov.-Dec. 2011, pp. 1-9, 2011.

Acknowledgements

I am first of all indebted with my supervisor Prof. Federico Millo, who has supported and considerably helped me in realizing my ambition to spend a research period in Germany, and has guided me during this work.

I would like to thank Dipl. Ing. Christof Schernus, who has allowed me to be hosted at FEV GmbH. Without his support and willingness this work would have never been possible. He also helped me in getting well acquainted at FEV and in Aachen, considerably contributing to the success of this experience.

I also would like to thank Dr. Ing. Jens Ewald, who has helped me with valuable suggestions and constant guidance, and thanks to his understanding I had a pleasant and instructive permanence at FEV.

I thank Dr. Ing. Andrè Brunn, who has always supported me providing the data and information I needed as fast as possible, as well as all the other colleagues at optical laboratory.

Also the other colleagues at FEV, in particular Dr. Ing. Matthias Budde and Dipl. Ing. Bastian Morcinkowski, have helped me sharing their valuable know-how and pleasant company.

Giuseppe Falleti, during his thesis work, has contributed significantly to some of the simulations, pictures and graphs I used for this work.

Last but not least, I would like to thank all the colleagues

and friends who have shared their knowledge and their friendship in all the places where this work has been developed, such as Andrea Bianco, Theodoros Vlachos, Rossella Rotondi and many others that, although are not mentioned here, played an important role in my personal and professional growth.